Università degli Studi di Padova

Padova Neuroscience Center

Ph.D. Course in Neuroscience   *XXXV Series*

A brain-silicon closed-loop hybrid system with synapse-inspired neuroelectronic links

Supervisor
Prof. Stefano Vassanelli

Co-supervisor
Prof.ssa Alessandra Bertoldo

PhD Candidate
Mattia Tambaro

Coordinator
Prof. Antonino Vallesi

Academic Year
2022-2023

"Agilulfo, lui, aveva sempre bisogno di sentirsi di fronte le cose come un muro massiccio al quale contrapporre la tensione della sua volontà, e solo così riusciva a mantenere una sicura coscienza di sé. Se invece il mondo intorno sfumava nell'incerto, nell'ambiguo, anch'egli si sentiva annegare in questa morbida penombra, non riusciva piú a far affiorare dal vuoto un pensiero distinto, uno scatto di decisione, un puntiglio."

— Il cavaliere inesistente, Italo Calvino

Abstract

The SYNCH project (a synaptically connected brain-silicon neural closed-loop hybrid system) aims to create a hybrid system connecting a biological neural network (BNN) in the brain of a living animal and a spiking neural network (SNN) on a chip through memristors, mimicking synapses, enabling co-evolution of connectivity and co-processing of information at the level of neurons. The SNN acts as a supportive network, processing activity read from a neuronal population, and modulating neural behavior through intracortical microstimulation (ICMS). In the context of this project involving many partners and universities, my work and this thesis focus on the real-time bidirectional brain-computer interface and, therefore, on the detection of ongoing intracortical neuronal activity, such as extracellular action potentials (AP) and multiunit activity (MUA), and on the characterization of the feedback available to the SNN via intracortical microstimulation (ICMS).

The bidirectional communication consists of developing a system that detects the in-vivo neuronal spiking activity in real time by extracting the relevant features –location and timing– to be fed as input to the SNN. The use of a traditional computer architecture to detect and send events and to receive stimulation triggers introduces a variable latency of a few tens of milliseconds due to the USB connection with the recording system and the software elaboration time. But to achieve a reliable closed-loop control and drive properly the neural activity, the latency between an event occurrence and its detection is a crucial point. For this reason, I developed a spike detection algorithm running directly on the FPGA of an electrophisiology recording system, together with the logic required to stimulate the tissue from the same electrode array used to sense the neuronal activity.

For the characterization of the effect of the ICMS perception of the brain network, I classified the neural activity evoked by ICMS experiments conducted in the somatosensory cortex of rats during urethane anesthesia. Activity is recorded by a probe that spans the entire depth of the cortex and allows the recording of the local field potentials (LFP), as well as the MUA and the AP of subpopulations of neurons, while also allowing simultaneous stimulation. I found that the ICMS caused an initial inhibition of the activity of about 120-140 ms, followed by spindle-like activity at about 11-12 Hz. The evoked response in its entirety lasts many hundreds of milliseconds, originating from the central layers (upper end of Va and IV) and then spanning to layers III and Vb, with stronger and more widespread activity in the central oscillations. Varying the ICMS parameters –amplitude, duration, and depth –, the response did not show any significant variation in shape. The stimulation amplitude start to be effective from 5 μA with a higher number of successfully evoked trials per experiment when increased, while stimulating in layers between IV to VI did not show any significative difference. Based on these results, the response is modulated by applying pulse trains at different frequencies (5 to 20 Hz). The trains showed to strongly attract the spindles frequency to the frequency of the stimulation. By combining ICMS of different frequencies with different amplitudes (5 to 20 μA), the neuronal activity could be modeled following the pictorical representation of an Arnold's tongue, highlighting the typical behavior of a robust self-sustained oscillator during the evoked spindle.

Contents

Listing of figures

ix

xiii

Listing of tables

Listing of acronyms

ADC . . . . Analog to Digital Converter

ANN . . . . Artificial Neural Networks

AP . . . . Action Potential

AER . . . . Address Event Representation

BRAM . . . . Block Random Access Memory

CU . . . . Control Unit

EEG . . . . Electroencephalography

EPSP . . . . Excitatory Postsynaptic Potential

FIFO . . . . First-In First-Out

FPGA . . . . Field Programmable Gate Array

GUI . . . . Graphical User Interface

HDL . . . . Hardware Description Language

ICMS . . . . Intracortical Microstimulation

IIR . . . . Infinite Input Response

IPSP . . . . Inhibitory Postsynaptic Potentials

LFP . . . . Local Field Potential

MAD . . . . Median Absolute Deviation

MSB . . . . Most Significant Bit

MUA . . . . Multiunit Activity

POm . . . . Posterior nucleus

RAM . . . . Random Access Memory

RMS . . . . Root Mean Square

SNEO . . . . Smoothed Nonlinear Energy Operator

SNN . . . . Spiking Neural Network

SNR . . . . Signal-to-Noise Ratio

SPI . . . . Serial Peripheral Interface

STDP . . . . Spike Timing Dependent Plasticity

SWS . . . . Slow-Wave Sleep

TG . . . . Trigeminal Ganglion

TN . . . . Trigeminal nuclei

UART . . . . Asynchronous Receiver-Transmitter

UDP . . . . User Datagram Protocol

USB . . . . Universal Serial Bus

VPM . . . . Ventral Posteromedial Nucleus

1

Introduction

The brain's remarkable computational properties provide animals with unmatched physical autonomy, interaction and adaptation capabilities compared to any artificial system. Its complex network are constantly evolving to optimize processing of real-world inputs by relying on event-based signaling and self-reorganizing connectivity, giving it an unique capabilities of autonomy and adaptation. Here, spikes are transmitted between neurons through synapses undergoing continuous *birth-death* and adjustment, reconfiguring brain circuits and adapting processing to constantly changing inputs. The SYNCH project (a synaptically connected brain-silicon Neural closed-loop hybrid system) builds upon the growing understanding of brain biology, particularly the features of neuronal networks and the evolution of their synapses. The project aims to create a hybrid of biological and technological components by establishing synapse-inspired links between brain neurons in vivo and their digital counterparts, using a neuromorphic approach. This will create a hybrid system connecting the brain of a living animal and a spiking neural network (SNN) on a chip through memristors, enabling co-evolution of connectivity and co-processing of information at the level of neurons. The hybrid system will have programmable features of functionality and connectivity, making it suitable for applications in bioengineering, biorobotics, self-adapting biomedical devices, and advanced neuroprostheses, such as an artificial retina.

In the context of this project involving many partners and universities, my work and particularly this thesis focuses on the real-time bidirectional interface between the biological and digital domains. Therefore, on the detection of ongoing intracortical neuronal activity, such as extracellular action potentials (AP) and multiunit activity (MUA), as well as the characterization of the feedbacks available to the SNN through intracortical microstimulation (ICMS).

The first part of this bidirectional communication consists in developing a system that detects the in vivo neuronal spiking activity in real time by extracting the relevant features –location and timing– to be fed as input to the SNN. The interfacing of the systems occurs both via the Internet (when displaced in different countries) and via direct communication (for system integration in loco). For remote integration of closed-loop components, I developed spike detection operations on a custom version of the acquisition software that runs on the host computer. The software has been modified to stream events detected by a set-by-hand threshold crossing spike detection algorithm running in real time, while stimulating on the trigger received. Using a traditional computer architecture to detect and send events introduces a variable latency of a few tens of milliseconds due to the universal serial bus (USB) connection

with the recording system and the software elaboration time –the same is for the stimulation trigger–; anyway, this is not a serious limitation for the remote closed loop, where the latencies are mostly dominated by the time required by the packets to travel through the network (dozens of milliseconds) and its variability. To achieve stronger closed-loop control and drive activity, the latency between an event occurrence and its detection is a crucial point. For this reason, for the local integration of the closed-loop components, I worked to implement the spike detection algorithm directly on the Field programmable gate array (FPGA, 1.1.5) of the RHS controller. This FPGA is normally used to control the recording, to drive the headstages, and to buffer the data to send to a computer where it is stored. The hardware description language (HDL) design of this device is open source, as is the software that controls it. For detection operators, I worked on algorithms that were suitable for real-time and reliable detection of intracortical activity. From recordings originated from the same device, I founded the Smoothed Nonlinear Energy Operator (SNEO) algorithm to be a light and reliable spike detector method; it demonstrates a good accuracy level while not being greedy of resources, allowing for a real-time implementation while requiring small amount of resources, scarcely available on the instrument. I adapted this algorithm to develop an FPGA pipeline to process the real-time stream of signals recorded by 32 channels, and I also adapted the controller software to add spike visualization and spike detection settings. The detected events are streamed both via a privileged channel of communication to the host for Internet forwarding and via hardware-connected cable with almost a negligible latency from the spike detection.

The second part of the bidirectional communication consists of exploiting an experimental paradigm to develop and test the closed-loop system and the interaction from the SNN to neurons, characterizing the effect of the ICMS perception of the brain network. I classified the neural activity evoked by ICMS experiments conducted in the somatosensory cortex of rats during urethane anesthesia. Specifically, experiments are conducted in the barrel cortex, an area that is well known to be the cortical representation of the mustachial pad of rats, where each barrel corresponds to a principal whisker (or vibrissae). Activity is recorded by a probe that spans the entire depth of the cortex and allows recording of the local field potentials (LFP), as well as the MUA and the AP of subpopulations of neurons, while also allowing simultaneous stimulation by applying current pulses to the tissue. At first, I studied whether it was possible to evoke by ICMS the same neural activity elicited by the physical stimulation of the whisker, to investigate the possibility that the anesthetized rat could perceive them in the same manner. Therefore,

I characterized the spiking activity elicited in the barrel cortex by mechanically stimulating the whisker using a piezoelectric bender and electrically stimulating with pulses of different intensities and duration, applied at different depths of the cortical. If the response evoked by whisker mechanical stimulation consisted of a strong deflection in the LFP and an increase in the firing rate originating from layers IV and Vb and spanning across all layers at 10-15 ms from the stimuli, I found that the ICMS caused an initial inhibition of the activity of about 120-130 ms, followed by spindle-like activity at about 11 Hz. The evoked response in its entirety lasts many hundreds of milliseconds, originating again from the central layers (upper end of Va and IV), but usually spanning to layers III and Vb only, with stronger and more widespread activity in the central oscillations. Based on these results, to characterize this response so that it can be exploited for the purpose of the SYNCH project, I modulated the response by applying pulse trains at different frequencies (5 to 20 Hz) for a duration of 1 second, to provide to the SNN a set of different feedbacks to apply to control the activity. The trains showed to strongly attract the spindle frequency to the superimposed one. By combining ICMS of different stimulation amplitudes (5 to 20 μA) with different frequencies, I investigated whether neuronal activity could be modeled to describe the phenomenon. Combining the results, the pictorical representation of an Arnold's tongue emerged, highlighting the typical behavior of a robust self-sustained oscillator during the evoked spindle.

1.1 Background

This section wants to provide some background information from the literature to the topic that will be explored in this thesis.

1.1.1 Electrophysiology & techniques

Electrophysiology is the study of electrical activity in biological systems and has been used to explore the mechanisms underlying a variety of physiological processes. It relies on sophisticated instrumentation that can measure small changes in electric potential, current flow, and impedance at different levels within an organism or cell. Electrophysiological techniques provide valuable insight into the functioning of individual cells as well as whole organ systems. In the context of monitoring brain signaling, these techniques involve using specialized equipment and techniques to measure the electrical activity of brain cells or neurons.

The field of neural electrophysiology has been around for many decades, with its beginnings in the work of pioneering neurologists such as Charles Scott Sherrington and Ivan Pavlov. Through the use of electrical recordings, researchers began to understand the role of neural activity in various brain functions and behavior. This field has its roots in the work of two British scientists, Alan Hodgkin and Andrew Huxley, who in 1952 published their groundbreaking paper "A quantitative description of membrane current and its application to conduction and excitation in nerve" [1]. In this paper, they proposed a mathematical model of the AP, which describes how the electrical potential of a neuron changes over time in response to a stimulus, providing a quantitative description of the electrical signals generated by neurons. This work led to the development of techniques such as single-unit recording, patch clamp, and voltage-sensitive dye imaging, which are now widely used to study the activity of neurons in both animal models and humans. Neuronal electrophysiology has grown exponentially over the past several decades and has contributed significantly to a better understanding of the nervous system and provided the foundation for many of the advances in neuroscience that have been made since then.

Nowadays, it is used to monitor brain signaling for a variety of purposes, including diagnosis and evaluation of neurological disorders, brain mapping, and neurosurgery. It can provide valuable information about the function and activity of different regions of the brain, and it can help identify areas

of abnormal activity or connectivity. In some cases, electrophysiological monitoring can also be used to guide interventions such as brain surgery or stimulation therapies. Some common electrophysiology techniques used to monitor brain activity include:

- Electroencephalography (EEG): This technique involves placing electrodes on the scalp to measure the electrical activity of the brain. It is a non-invasive method that is commonly used to diagnose and evaluate neurological disorders, such as epilepsy and brain tumors.

- Electrocorticography (ECoG): This technique involves placing electrodes directly on the surface of the brain to measure the electrical activity of specific regions of the brain. It is an invasive technique that is often used during brain surgery or other interventions to guide the placement of electrodes or other devices.

- Magnetoencephalography (MEG): This technique involves using highly sensitive magnetic sensors to measure the magnetic fields produced by the electrical activity of the brain. It is a non-invasive method that is often used in conjunction with other techniques, such as MRI, to provide detailed information about brain function and connectivity.

- Functional magnetic resonance imaging (fMRI): This technique involves using magnetic resonance imaging to measure changes in blood flow and oxygenation in the brain, which are thought to reflect changes in brain activity. It is a non-invasive method that is commonly used to study brain function and connectivity.

- Multi-electrode array (MEA) electrophysiological recording: This technique involves placing electrodes directly inside the brain to measure the electrical activity of specific regions. It is an invasive technique that is often used in research and clinical settings to study the function and activity of specific brain regions.

In particular, MEA recording is a technique for extracellular recording, measuring voltage fluctuations of neurons from outside their membranes [2]. It can provide detailed information about the electrical activity of the brain, including the timing, amplitude, and frequency of neural activity. This can be useful for studying the brain's response to different stimuli, such as sounds or visual patterns, or for studying the functional connectivity between different brain regions. This method typically uses microelectrodes of only a few micrometers in width inserted into the tissue to acquire signals from individual neurons or population activity, typically through a small hole in the skull. These microelectrode arrays enable the possibility of sensing the small-amplitude extracellular depolarization of a population

of neurons near its metallic surface [3, 4, 5, 6], allowing the simultanous recording of LFPs –some mV–, APs –hundreds of μV–, and MUAs –tens of μV–. If the LFP is the slow-changing electric potential in the extracellular medium around neurons (up to some hundreds of Hz) [7] and the AP is a rapid sequence of changes in the voltage across a membrane of a single neuron (from hundreds to thousands of Hz) [8], a MUA represents something in between. It is believed to be the average spiking of small neuronal populations close to the vicinity of the placed microelectrode and it is obtained by band-pass filtering the recorded signal in a frequency range of 300-500 to a few thousand Hz [9]. MUA signals are usually analyzed to study population-level neural activity, rather than the activity of individual neurons and can provide information about the firing rates and the temporal patterns of activity in a population of neurons, which can be used to study information processing in the brain. MUA is also useful in studies where it is not possible or practical to record the activity of individual neurons. Typically, microelectrodes are placed on a probe with one or more shanks, with a channel count increased to hundreds or even thousands [10, 11, 12]. These microelectrodes can also be used to inject variable current or voltage to evoke a physiological response from neurons in a sphere centered on the stimulating channels [13, 14].

The electrodes are typically placed inside the brain and are connected to a recording device that is used to measure the electrical activity of neurons in the surrounding area. Common applications include investigating the neural pathways involved in movement control, sensory processing, memory, and learning. A related technique involves stimulating with electric fields generated by the electrodes known as ICMS [15]. ICMS can be used to modulate neuronal firing patterns for therapeutic purposes or to assess functional connectivity between brain regions [16, 17].

1.1.2 Barrel cortex of rat

The barrel cortex is a distinct cortical area in the neocortex of rodents located within the somatosensory cortex. This area plays an important role in the processing of sensory information from the whiskers, a key sensory organ for rats, which allows the rat to accurately perceive the shape and location of objects based on the movement of its whiskers.

The barrel cortex has been extensively studied to understand how sensory input is encoded and transformed into meaningful representations, and has provided valuable insights into the organization and

function of the somatosensory cortex. It consists of several interconnected cytoarchitectonic fields that are typically organized into a set of barrels or columns [18] arranged in an isomorphic map of the mystacial whiskers, where each vibrissa is specifically mapped to a barrel of neuronal populations, as shown in Figure 1.1. This mapping is also seen at each step of the sensory pathway, with ensambles called *barrelettes* [19, 20, 21, 22] in the principal trigeminal nucleus of the brain stem, *barreloids* [23, 24, 25] in the ventral posteromedial nucleus (VPM) of the thalamus, and *barrels* in the primary somatosensory cortex. Each barrel is selectively activated by the corresponding whisker on the contralateral whisker pad [26, 27, 28], called the principal whisker, and forms a cortical processing unit for that single vibrissae. Each barrel column is composed of a vertical array of 2 mm that runs orthogonally to the six-layered structure of the cortex, and is separated from the others by a narrow zone called *septa* [29, 18] of approximately 70 μm [30]. Barrel-columns, as well as the whiskers on the mystacial pad, can be identified by their arc position (1-7, caudal to rostral) within a specific row (A-E, dorsal to ventral) in a simple grid-like organization. The name "barrel" is due to the curved shape that resembles a 500 μm large [30] barrel stave (Figure 1.2a), which contains approximately 2000 neurons. The barrel field in the rat comprises neurons in a volume of 4.7 to 6.4 mm^2, varying from specimen to specimen [31, 18], of which 75% are excitatory and 25% are inhibitory [32]. In rats, this structure has been particularly well studied due to its unique cellular organization and overall anatomical complexity. Each barrel receives input from all related primary afferents and projects to other cortical areas to receive sensory information. Layer IV sends strong functional excitatory connections to all other layers within the column, while layer V is the only layer within the column that receives functional excitatory input from all other cortical layers within the column [33]. This topographic organization has been suggested to play an important role in motor control during tactile exploration [34]. The neuronal architecture formed by the convergence of thalamocortical afferents from the corresponding whisker follicles [35] within each barrel contains different types of neurons with distinct properties such as orientation selectivity or spatial integration capabilities. Neurons located within the same barrel can respond differently depending on various factors, including depth within the cortex or stimulus, and activity patterns can be used to decode different tactile stimuli, such as touch intensity or directionality [36, 37, 38]. Synchronized activity between pyramidal cell populations located within each individual barrel has been shown to occur when animals perform active exploratory movements with their whiskers such as whisking or tapping stimuli on objects, suggesting
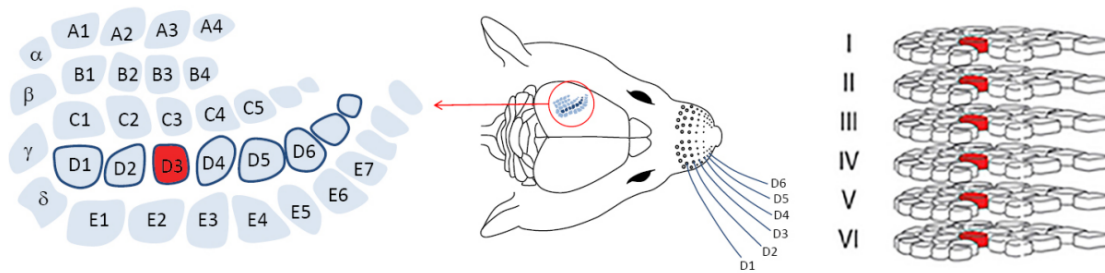
Figure 1.1: Organization of the barrel field of rats. Barrels are organized in an isomorphic map of the mystacial whiskers and both are indicated by a letter and a number identifying their position. Each barrel is divided in turn in layers.

a possible role for these interactions in sensory processing [39, 40].

WHISKER-BARREL PATHWAY

The whisker-barrel pathway is a highly studied system in rodents and involves the integration of sensory information from the mechanoreceptive organs, the vibrissae, to generate complex behaviors.

The follicle attaches the whisker to the skin and provides tactile sensitivity and motion to the whisker. Each follicle is innervated by the peripheral branches of about 200 cells of the trigeminal ganglion (TG) whose nerve endings convert mechanical energy into APs. These afferent signals travel past the cell bodies in the TG and continue along the central branch to form synapses in the trigeminal nuclei (TN) of the brainstem. From here, vibrissal information is conveyed to the thalamus through three main parallel pathways before continuing to the barrel field of the somatosensory cortex (Figure 1.2a), some of them forming sensorimotor loops below the cortical level. The lemniscal pathway has neurons in the principal TN clustered in barrelettes, whose axons travel to the barreloids of the dorsomedial section of the ventral posterior medial nucleus of the thalamus. Both barrelettes and barreloids are sets of modules arranged as a topographic projection of the whiskers; neurons in a given module respond principally to the particular somatotopically connected whisker, thus defining a single whisker receptive field for trigeminal sensory neurons [41]. The axons of dorsomedial VPM neurons project to the primary somatosensory cortex (S1), where they terminate in the barrels of layer IV. The extralemniscal pathway has neurons in the caudal part of the interpolar TN clustered into whisker-related barrelettes, which project to the ventrolateral domain of the VPM, where neurons cluster in the tails of the dorsomedial VPM barreloids. The axons of ventrolateral VPM neurons project to the septa between the barrels of S1

9

and to the secondary somatosensory cortex (S2). The paralemniscal pathway has neurons in the rostral part of the interpolar TN that are not spatially clustered and project to the medial sector of the posterior nucleus (POm). The axons of POm neurons project to targets immediately ventral to the barrels, in layer Va of S1, S2 and to the primary motor cortex. The paralemniscal pathway is not spatially specific, it integrates multiple whisker information and defines a multiwhisker receptive field [42]. The functions of the different pathways have not yet been directly tested, and hypotheses vary between research groups; however, the selectivity of the response during artificial whisking suggests that paralemniscal neurons convey information about whisking kinematics, extralemniscal neurons about contact timing, and lemniscal neurons about detailed whisking and touch information [43]. Subsequently, neurons within the barrel cortex respond to stimulation of single or multiple whiskers through lateral connections between barrels, mediating communication between different modalities of cortical representation. Furthermore, this network extends further downstream into other brain regions involved in motor control, including the basal ganglia and cerebellum. This pathway is important for allowing the rat to accurately perceive and respond to tactile sensations from its whiskers.

Thalamo-cortical loop

The thalamus is a complex structure in the brain that plays a role in the processing and relay of sensory and motor information. It is a large collection of neuronal groups located between the cerebral cortex and the midbrain. It is involved in sensory, motor, and limbic functions, such as regulating consciousness, sleep, and alertness. All information that enters the cortex is filtered through the thalamus, making it called the gateway to the cerebral cortex.

Initially considered to be a simple relay station that passes information between the cortex and the peripheral nervous system, the thalamus can switch between two modes of information transfer, bursting and tonic, and has a dynamic and controllable change between OR and AND -gating [44]. The thalamus is connected to the cortex and its continuous input is necessary to maintain cortical activity [45] and to support behavioral tasks by improving functional cortical connectivity [46]. In turn, corticothalamic projections, which outnumber thalamocortical (TC) projections by approximately an order of magnitude [47, 48], shape thalamic activity. The thalamus is composed of two structures, the *dorsal* thalamus (usually simply referred to as thalamus) and the *ventral* thalamus (known as subthalamus or

(a) Intercolumnar and Intracolumnar interactions of the barrel cortex. Only the most important interlaminar connections are shown and local recurrent connections are not indicated. Intracortical input to layer VI is poorly characterized. Adapted from [55].

(b) somatosensory talamocortical loop in rodents: primary pathways. Taken from [56].
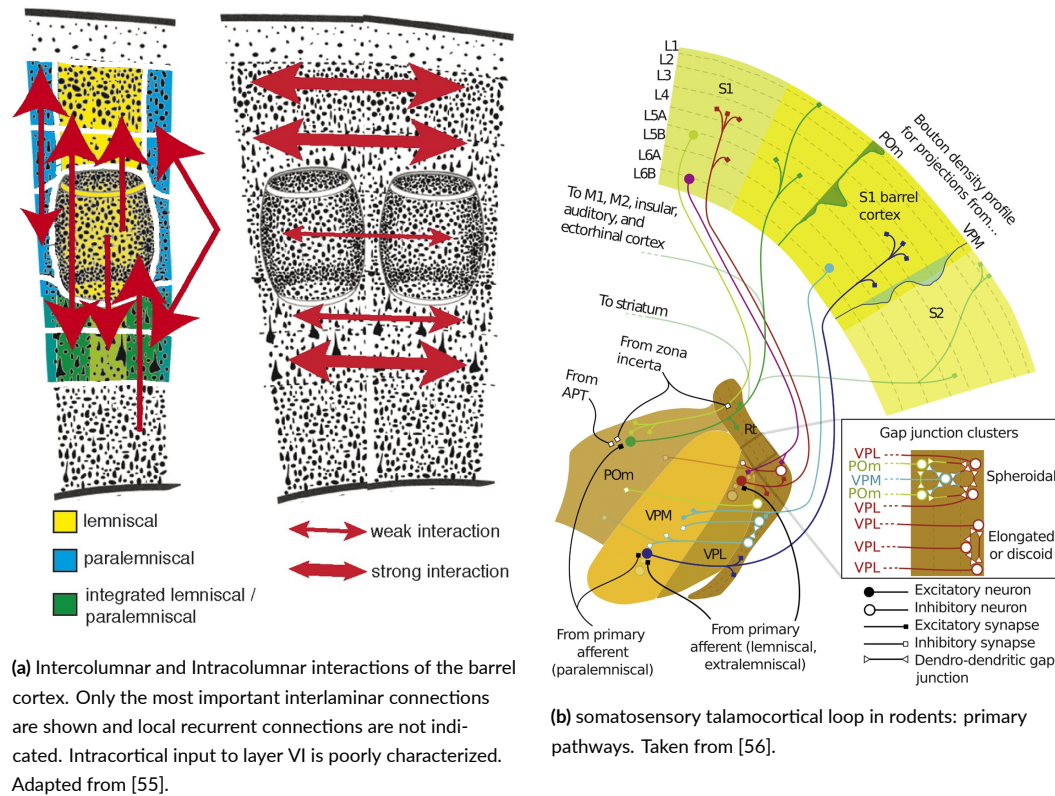
Figure 1.2: Microcircuit of the barrel cortex and talamocortical loop in rodents.

prethalamus) [49]. In the somatosensory system, the ventrobasal complex of the dorsal thalamus (VB) consists of two first-order nuclei that relays somatosensory signals: the VPM for the face and neck area, and the VPL for the rest of the body. These nuclei receive peripheral input through various pathways, such as the lemniscal, extralemniscal, and paralemniscal pathways. Rodent VB is mainly composed of excitatory TC cells that target S1, mainly L4, but also L2-3 and L5b-6 (see Figure 1.2b) [50, 51]. These cells send collaterals to the inhibitory reticular nucleus (Rt) of the ventral thalamus , and the signals are amplified and further processed by the cortical microcircuitry [52]. Additionally, TC cells send monosynaptic pathways directly back to the thalamus [53]. The anterior part of POm projects preferentially to L5, while the posterior part tends to innervate L1 with sparser and wider axonal arborization [54]. FO and HO TC projections innervate the complementary cortical lamina [50, 51], and do not send intra-nucleus collaterals, but collaterals to Rt on their way to the cortex [54].

One particular area of interest within the field of the barrel cortex is the response evoked by whisker stimulation, which has been shown to be highly organized and structured. The response evoked in the barrel cortex by whisker stimulation is a key element to understanding the neuronal basis of tactile perception.

Whisker stimulation produces sensory information that is processed through the somatosensory thalamus and transmitted to primary somatosensory cortical areas, including the barrel cortex [57]. It activates neurons in the barrel cortex through direct activation of mechanoreceptors located on the whiskers themselves as well as through indirect pathways involving other brain regions such as thalamus [58]. This activation leads to a complex pattern of activity across different layers and columns of neurons, with each layer exhibiting distinct responses depending on stimulus parameters such as intensity, duration, frequency, and location [59, 60]. In addition to these spatiotemporal patterns of neuronal firing, studies have also revealed that whisker stimulation can evoke specific types of synaptic plasticity in the barrel cortex. Long-term potentiation has been observed following brief periods of high-frequency stimulation, while long-term depression occurs when stimuli are applied at low frequencies for extended periods [61, 62]. These forms of plasticity are believed to play an important role in learning and memory formation processes within this region. Overall, research into the response evoked by whisker stimulation has provided valuable insight into how sensory information is processed within the rodent neocortex. By understanding how individual neurons respond to different stimuli we can gain a better understanding not only about basic mechanisms underlying cortical function but also about higher order cognitive processes such as learning and memory formation.

Spindles in somatosensory neocortex

The spindle oscillations of the thalamocortical system are a widely studied phenomenon in neuroscience. Spindles are rhythmic bursts of electrical activity that occur during slow-wave sleep (SWS) and can be observed by EEG. They typically last approximately 0.5 to 2 seconds and have a frequency range of 10–15 Hz, with peaks at 12–14 Hz [63, 64].

In rodents, neocortex has been shown to display high levels of spontaneous spindle activities during

SWS. Studies suggest that these spindles may play an important role in information processing related to tactile perception, as they show higher amplitude responses when presented with stimuli evoked by whisker movements compared to non-stimulated conditions [65]. Spindle activity is believed to be involved in memory consolidation processes by modulating synaptic plasticity mechanisms [66]. It was demonstrated that disrupting these oscillations led to impairments in spatial learning tasks, suggesting a link between them and memory formation processes associated with the barrel cortex region. Also, spindle bursts represent a functional hallmark of the developing cerebral cortex in vitro and in vivo and have been observed in various neocortical areas of newborn rodents. Spindle bursts are generated in complex neocortical-subcortical circuits that often involve the participation of motor regions of the brain. Together with early gamma oscillations, spindle bursts synchronize the activity of a local neuronal network organized in a cortical column [65, 67].

1.1.3 Intracortical microstimulation

ICMS is a neuromodulatory technique of electrical stimulation of the brain that has been used to study the neural basis of motor, sensory, and cognitive functions in humans for more than two decades. ICMS involves the application of electrical current to cortical neurons through electrodes implanted inside the brain to activate them. This approach has provided invaluable insight into how different regions of the cortex are functionally connected and how stimulation can alter behavior, including movement, perception, and cognition.

The use of ICMS began with pioneering work by [68], who showed that small amounts of electrical current applied directly to single neurons could induce movements or sensations in humans without any external stimulus being presented. Since then, numerous studies have demonstrated that applying low-amplitude electrical pulses directly to human cortex can produce a variety of physiological effects such as modulating sensory thresholds or altering pattern recognition performance[69, 70]. These effects have also been shown to be regionally specific with stimulation at different sites producing different behavioral outcomes. Furthermore, ICMS has played an important role in understanding how local neural circuitry contributes to higher-order cognitive processes such as decision making and learning. By stimulating individual neurons within particular regions while subjects perform certain tasks, it is possible to obtain information about which cells contribute most strongly towards task performance.

ICMS in the somatosensory cortex is a promising new field of neuroscience research that has the potential to revolutionize our understanding of the brain. In recent years, advances in ICMS have enabled scientists to stimulate and record from individual neurons in the somatosensory cortex with unprecedented precision and accuracy. This technique has opened up exciting possibilities for studying how neuronal activity relates to behavior and learning, as well as providing insight into disease states such as chronic pain or Parkinson's disease. The primary goal of this type of research is to identify which regions of the somatosensory cortex are involved in particular behaviors or responses, and then use ICMS to manipulate those areas with greater specificity [71]. By selectively targeting specific neural pathways within the somatosensory cortex, researchers can gain valuable insights into how sensory information is processed by different parts of the brain. Furthermore, these studies have revealed how different types of stimuli interact with each other at a cellular level. In addition to its applications in basic science research, ICMS also holds great promise for clinical treatments related to disorders associated with abnormal sensory processing. This technique may be useful for alleviating symptoms associated with various neurological conditions including stroke rehabilitation or neuropathic pain management. Overall, ICMS provides an invaluable tool for studying both normal brain function as well as neurological disorders such as Parkinson's disease and epilepsy where altered cortical activity plays an important role. As such, this approach has great potential to develop novel therapies aimed at restoring neuronal activity patterns associated with healthy functioning. Also, ICMS has become an increasingly important tool for exploring both healthy and diseased brains alike. It provides us with an invaluable window into how neural circuits process information about our environment -—from simple tactile inputs all the way through complex cognitive tasks—- and gives us hope that we might one day be able control these processes more effectively than ever before.

1.1.4 Arnold's tongues

An Arnold tongue is a pattern of behavior in a nonlinear system that exhibits periodic behavior. The term is named after the mathematician Vladimir Arnold, who studied the behavior of such systems in the 1960s. An Arnold tongue typically consists of a series of periodic regions in a parameter space, each of which corresponds to a different frequency of the periodic behavior. The boundaries of these regions form a tongue-like shape, hence the name. In general, the behavior of a system with an Arnold tongue

is highly sensitive to changes in its parameters, which can lead to a variety of complex and interesting phenomena.

The Arnold's tongue phenomenon is a well-known concept in chaos theory, which describes the behavior of nonlinear dynamical systems when driven at different frequencies. The idea behind this phenomenon is that certain ranges of frequencies can produce chaotic behavior while other ranges can lead to regular or periodic behavior. In essence, it suggests that there exists a "tongue" shaped region within the frequency domain where chaotic dynamics occur and outside of which regular or periodic dynamics take place. This phenomenon has been extensively studied over the past few decades and its implications for various fields such as engineering, physics, biology, and economics have been explored [72]. For example, researchers have used Arnold's tongue to study synchronization phenomena in coupled oscillators, pattern formation in chemical reactions, and even financial markets. Furthermore, recent studies have suggested that understanding how Arnold's tongues form could be useful in controlling complex systems with multiple parameters [72, 73].

It is believed that the spindles in the brain may have originated from the chorticothalamic loop. However, it is also true that they are the result of the coordinated activity of many neurons [74]. In theoretical and computational models, this collective brain dynamics is considered a macroscopic self-sustained oscillation [75, 76]. These models are used to develop algorithms to cancel abnormal brain rhythms by deep brain stimulation to treat pathological brain conditions [75, 77, 78, 79]. The reductionist approach to treating a large network of neurons as a single active unit comes from studies in nonlinear dynamics, which suggest that a collective oscillatory mode of a large population of highly interconnected units emerges through a Hopf-like bifurcation. This means that the population can be considered a macroscopic, self-sustained oscillator [80, 81]. This approach is simple and is based on the principle that synchronization theory predicts that if a system can be modeled as a noisy limit cycle or weakly chaotic oscillator, it will adjust its frequency when exposed to a rhythmic perturbation [82]. If the frequency of the oscillator is initially close to that of the external stimulation , then a stimulation of sufficient strength will lead to frequency locking, resulting in the frequencies becoming equal.

The SYNCH project aims to connect a network of neurons in the brain of a living animal and a SNN to create the hybrid system. The SNN acts as a supportive network, processing activity read from a neuronal population, and modulating neural behavior through ICMS. The two networks are interfaced through memristors, mimicking synapses that integrate the firing information between the two domains. In this way, a set of neuromorphic synapses with plasticity links the network of neurons to the SNN to form a hybrid network. While the brain has its own natural dynamics, the SNN can be programmed to operate within the hybrid in function of artificially imposed settings, implementing a reward-based learning by reservoir computing and opening a novel and yet unexplored scenario to investigate and modulate brain functiong. This project pursues ambitious innovation and theoretical objectives, including proof-of-concept demonstration that SNN can act as a *smart* and low power device for adaptive electrical brain neuromodulation in a rodent model with brain-inspired machine learning approaches for recognition of biosignals based on spiking neurons and brain-inspired synaptic connectivity. A sketch of the morphology of the network is shown in Figure 1.3.

In this context, relying on the spiking activity as a source of events provides a fully coherent propagation of the information. The memristor are stimulated in discrete pulses, as well as the stimuli given to the SNN. The SNN itself then utilizes spikes to mimic the neuronal processing of the brain. The discrete events are also perfectly compatible with the digital communication between the components. The spiking activity carries meaningful information about the underlying neural dynamics ongoing in a specific brain area, as demonstrated by many works that relay on spikes to decode the functional state to interface the brain with external devices [83]. By preserving the temporal and spatial pattern of spikes, the SNN can efficiently project the activity to a higher dimensionality while functioning as a *reservoir*, to provide an easier decoding of the state of the biological network in a more controllable environment as the digital domain. Also, a processing based on spikes, rather than on continuous signal as LFP, allows for lower power application, opening the road for embedded processing in a miniaturized device consuming very small power and producing very little heat.
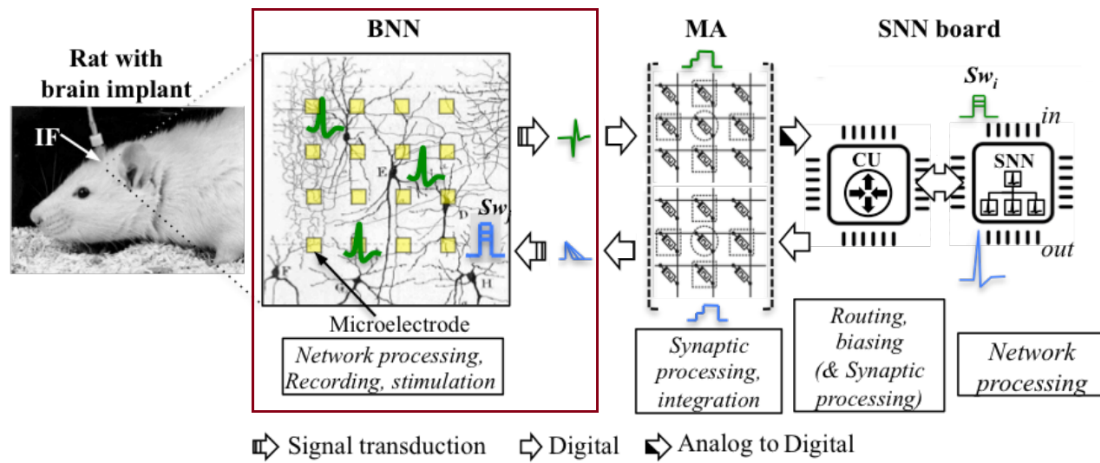
Figure 1.3: SYNCH component and communication scheme. The red box highlight the part object of this work, the interfacing with the network of neurons. Following, in order, the memristor array, the CU, and the SNN. This scheme is adapted from the SYNCH proposal.

Memristors

A memristor is a two-terminal electronic device that exhibits non-linear electrical properties and memory effects. It was first theorized by Leon Chua in 1971, but it wasn't until 2008 when the first working prototype of a memristor was created at HP labs [84]. The basic principle behind how a memristor works lies in its ability to store information based on the amount of charge that has flowed through it. This property makes them ideal for applications such as neuromorphic computing, where they can be used to emulate biological synapses [85]. The basic operation of a memristor involves the flow of electrons between two terminals that are connected by an electrolyte medium. When current flows through the device, ions from the electrolyte will move across its surface due to electrochemical reactions taking place at each terminal. This movement causes resistance changes that depend on both the magnitude and direction of current flow [86]. As more charge passes through the device, this resistance change accumulates over time resulting in what is known as "memristance". This phenomenon is reversible and can be used to store information even after power has been removed from the system [87]. Memristors also have unique switching characteristics compared to other passive devices such as resistors or capacitors. In particular, they exhibit a hysteresis behavior where their output depends not only on their input but also on their previous state [88]. This allows them to act as logic gates for digital circuits or analog filters for analog circuits depending on how they are configured. Additionally, because these devices

can retain information without external power sources they offer advantages over traditional memory technologies such as dynamic random access memory (RAM) or flash memory.

Spiking neural network

SNNs have recently emerged as a new type of artificial neural network that is capable of modeling the spiking behavior of neurons in the brain. These networks are inspired by biological neurons, which communicate with each other through electrical signals called spikes. SNNs use these same spikes to process information and make decisions, allowing them to better mimic natural neural processing than traditional artificial neural networks (ANNs). The main advantage of SNNs over ANNs is their temporal nature; they can process both spatial and temporal information simultaneously. This makes them well suited for tasks such as pattern recognition and classification, where it is important to capture changes over time. They also offer more efficient hardware implementations due to their sparse communication patterns [89]. In addition to being temporally aware, SNNs have several distinct features that separate them from ANNs. For example, they use an event-driven approach instead of a continuous one, as ANNs do [90]. This means that rather than constantly updating all nodes at every step, only those nodes affected by an input spike will be updated at any given moment in time. The result is a much more efficient system with fewer computations required per unit of time compared to ANNs. Another key feature of SNNs is their ability to learn using unsupervised learning methods such as spike timing dependent plasticity (STDP), which has been shown to be effective for learning complex spatio-temporal patterns from data streams [91]. STDP works by strengthening or weakening connections between neurons based on when their associated spikes occur relative to each other; this allows the network to adapt its weights according to what it learns from its environment without requiring explicit labels or supervision from an external source. Overall, SNN technology provides many advantages over traditional ANN models including improved temporal awareness and efficiency along with powerful unsupervised learning capabilities via STDP. As research into this area continues, we can expect further improvements in performance and applications for these powerful networks in various fields, ranging from robotics and computer vision tasks to medical diagnosis systems [92, 93, 94].

FPGA

An FPGA is a type of digital logic device that can be configured by a user to perform a variety of different functions. It consists of an array of programmable logic gates that can be connected in a variety of ways, allowing the device to perform a wide range of tasks. FPGAs are often used in electronic systems that require high performance, low power consumption, and/or flexibility for prototyping and testing of new electronic designs, as well as in the development of custom digital circuits for specific applications.

2

Datasets

2.1 Surgery & probe implant

Wistar rats are kept in the animal research facility of the Department of Biomedical Sciences of the University of Padua under standard environmental conditions. All procedures are approved by the local Animal Care Committee (OPBA) and the Italian Ministry of Health (authorization number 522/2018-PR). Young adult rats undergoing the experiments are in the range of P25-P35 (being P0 on the day of birth) with a body weight between 80 and 160 g and of both genders. Rats are anesthetized with an intraperitoneal induction dose of urethane (0.15/100 g of the body weight, 0.1 g/ml solution), followed after half an hour by an additional dose (0.015/100 g of the body weight). The anesthetic dose has been adapted from the standard dosage for surgical procedures [95] and tuned thanks to the expertise of the laboratory. After 10 minutes from the additional dose, a sub-cutaneous dose of Carprofen painkiller (Rimadyl; 0.5 mg/100 g of the body weight) is injected. 5 minutes later the animal is positioned on a stereotaxic instrument and the head is fixed by teeth- and ear-bars. Body temperature is maintained at 37^0C and recorded using a homeothermic monitoring system connected to a heating pad and a rectal probe (World Precision Instruments ATC1000 DC temperature controller) for the surgical and recording procedures. The anesthesia state is verified by poking the posterior paw and the eyelid of the animal and by observing the absence of whisking activity. Throughout the course of the entire experiment, the state of the anesthesia is continuously monitored after each set in the same manner. The depth of the anesthesia is also verified by observing the slow oscillation of the LFP activity, presenting of up- and down-state rhythmically as in what is commonly observed during deep anesthesia state [96, 97, 98]. An anterior-posterior opening in the skin is made in the center of the head and a dedicated window in the skull is drilled over the somatosensory barrel cortex at stereotaxic coordinates $-1 \div -4$ AP, $+4 \div +8$ ML referred to as bregma [99, 100], and a single shank probe is inserted orthogonal to the cortical surface in the middle of the window at coordinates -2.5 AP, $+6$ ML by means of a micromanipulator (PatchStar; Scientifica). As a reference for the recording/stimulation, the depth is set at 0 when the electrode proximal to the chip tip touches the cortical surface. The top four electrodes outside the tissue help to ensure the probe positioning also by visual inspection besides the depth of the probe tip. An Ag/AgCl electrode bathed in the extracellular solution in proximity of the probe is used as a reference. Throughout surgical procedures and recording, the brain is constantly bathed in a standard Krebs solution (in mM: NaCl

120, KCl 1.99, NaHCO 3 25.56, KH 2 PO 4 136.09, CaCl 2 2, MgSO 4 1.2, glucose 11). The probe placement, coordinates and angle, have been verified by multiple histologies performed on brain lesions left by the implant of thicker needles. The thin shaft of the probes used for these experiments makes it difficult to verify the insertion site from histology, so the insertion is verified electrophysiologically, by looking at the stereotypical response evoked by the whisker mechanical stimulation. Particularly, the placement of the probe is evaluated before starting the recordings by stimulating different whiskers following the somatotopic map existing between the mystacial pad and the S1 cortical architecture, to identify the whisker that gives the strongest evoked response and thus to identify the correspondent barrel. Prior to every experiment, the impedance of the probe electrodes is measured at 1 kHz and saved using the Intan controller. If the impedance of any electrode deviates greatly from the expected value of approximately 1 MΩ, the channel is marked as inoperative and is not considered for subsequent analysis. A faulty channel happened to be the first one on the tip of the probe, in this case the probe has been shifted down by an electrode to not lose any measurement in the layer VI, and the cortex depth mapping has been adjusted accordingly. Every animal undergoes an experimental protocol that normally includes at the beginning, middle and end of the experiment the recording of 5 minutes of spontaneous activity followed by a recording of 5 minutes of whisker stimulation. The experimental protocol is thus divided into two main phases, normally used for sets of stimulation of different amplitude.

2.1.1 ELECTROPHYSIOLOGY SETUP

The electrophysiology setup used to acquire data during the experiments is the RHS stimulation/recording controller from Intan Techonogies (Los Angeles, California, USA; Figure 2.1). The controller allows users to record electrophysiology signals and perform ICMS across up to 128 channels using open-source software. This device connects to a host computer via a USB 2.0 cable. The device supports:

- Up to 4 Intan RHS headstage with a sampling rate of 20, 25, or 30 kS/s each

- Biphasic or triphasic stimulation pulses generated with timing resolution as fine as 33 μs, pre-configured by software and triggered by keypresses or digital inputs

- Independent ground isolation on each headstage port to reduce noise from ground loops

- 2 analog input and 2 analog output ports with $\pm$10 V range and 2 digital input and 2 digital

output ports recorded in sync with amplifier waveforms, suitable to trigger stimulation pulses or to control automated episodic recording sessions.

- Optional I/O expander increases the number of auxiliary ports to 8 analog input and 8 analog output and 16 digital input and 16 digital output ports.

The stim/recording controller is connected via a thin and flexible serial peripheral interface (SPI) cable with a small 32 channel RHS headstage mounting two RHS2116 Stim/Amplifier chips, each with 16 independent stimulator/amplifier channels. The headstage integrates a configurable low-noise biopotential amplifier and a programmable constant-current stimulator capable of generating stimulation pulses from the microelectrodes. The headstage supports 32 channels and replaces all analog instrumentation circuitry in extracellular recording and stimulation systems. Some key points of this headstage are:

- integrated electrophysiology interface chip with amplifiers, stimulators, and industry-standard SPI.

- Stimulators source and sink currents ranging from 10 nA to 2.55 mA over an ± 9 V range.

- 16 bit Analog-to-Digital (ADC) samples amplifiers up to 40 kSamples/s per channel.

- Low noise floor: 2.4 μV root mean square (RMS) typical.

- Upper cutoff frequency configurable from 100 Hz to 20 kHz.

- Lower cutoff frequency configurable from 0.1 Hz to 1000 Hz.

- Fast amplifier artifact recovery for post-stimulus recording.

- Integrated, on site, multi-frequency electrode impedance measurement capability.

Probes used for barrel cortex recordings are Atlas E32 + R-65-S1-L6 NT, while probes used for talamocortical recodings are Atlas E32+R-200-S1-L20 NT. Probes details are listed in Table 2.1
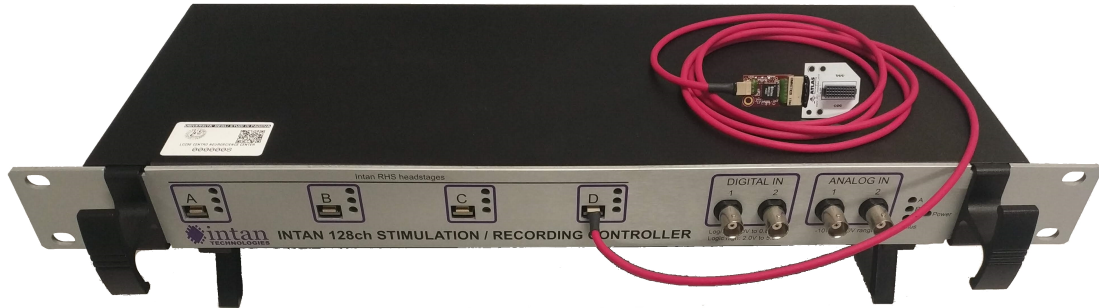
Figure 2.1: Intan Technologies RHS stimulation/recording controller. It supports the simultaneous recording from up to 4 headstages of 32 channels each, with a sampling frequency up to 30 kHz per channel, while allowing the ICMS with custom amplitude and duration from the same channels used to record.

Atlas	E32+R-65-S1-L6 NT	E32+R-200-S1-L20 NT
Number of shafts	1	1
Shaft length mm	6	20
Shaft width μm	123	123
Number of electrodes	32	32
Electrode Pitch μm	65	200
Electrode Range μm	2015	6200
Electrode diameter μm	25	25
Material	IrOx	IrOx
Probe thickness μm	50	50

Table 2.1: Probe details of the Atlas E32+R-65-S1-L6 NT.
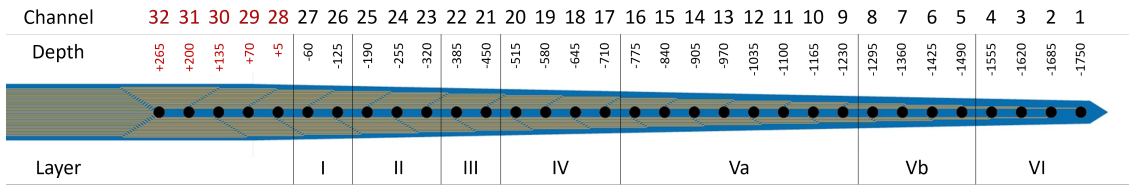
Figure 2.2: Atlas Neuro E32+R-65-S1-L6 NT tip, showing channels number, depth and layer placement of the electrodes in the barrel cortex.

2.2 Recordings in the rat barrel cortex

Barrel cortex signals are acquired by a single-shank probe with 32 iridium oxide electrodes (Atlas Neuro E32+R-65-S1-L6 NT) and recorded with a sampling frequency of 25 kHz by the Intan Technologies RHS Stimulation/Recording Controller. The wide band signal is filtered during acquisition with two single-pole high-pass filters (for digital filtering and offset removal) with a cutoff frequency of 0.1 Hz and a single-pole low-pass filter with a cutoff frequency of 7.6 kHz. In a single head stage, the system provides, on the same electrode array, both the amplification and digitization of 32 signals and the ICMS governed by current up to ± 7 V. The entire depth of the barrel cortex is covered by 27 out of the 32 electrodes of the probe, and only these are used for subsequent analysis, with channel number and location as in Figure 2.2. The layer depth of the barrel cortex, as well as the placement of the channels is based on the literature [101] and from previous histologies of the rat brain performed in the laboratory. The stimulation, mechanical or ICMS, is triggered by a waveform generator (Agilent 33250A 80 MHz, Agilent Technologies Inc., Colorado, USA), whose output is recorded synchronously with the neural signal by the recording controller via TTL (digital) input. From the onset of every ICMS, all electrodes are grounded for 1 ms to avoid saturation of the ADC and to achieve faster recovery from the stimulation artifact.

Each experimental setting is replicated with multiple rats and tests multiple stimulation protocols. I observed a great variability in both intra- and inter-animals stimuli-evoked responses. This forces us to collect a great number of repeated experiments to draw reliable conclusions. Some targeted experiments showed how the probability of evoking a response (and the strength and quality of the response) when administering the same stimulus varies greatly over time, even for the same animal, increasing and decreasing repeatedly. As suggested in the literature, this problem could be amplified by the different
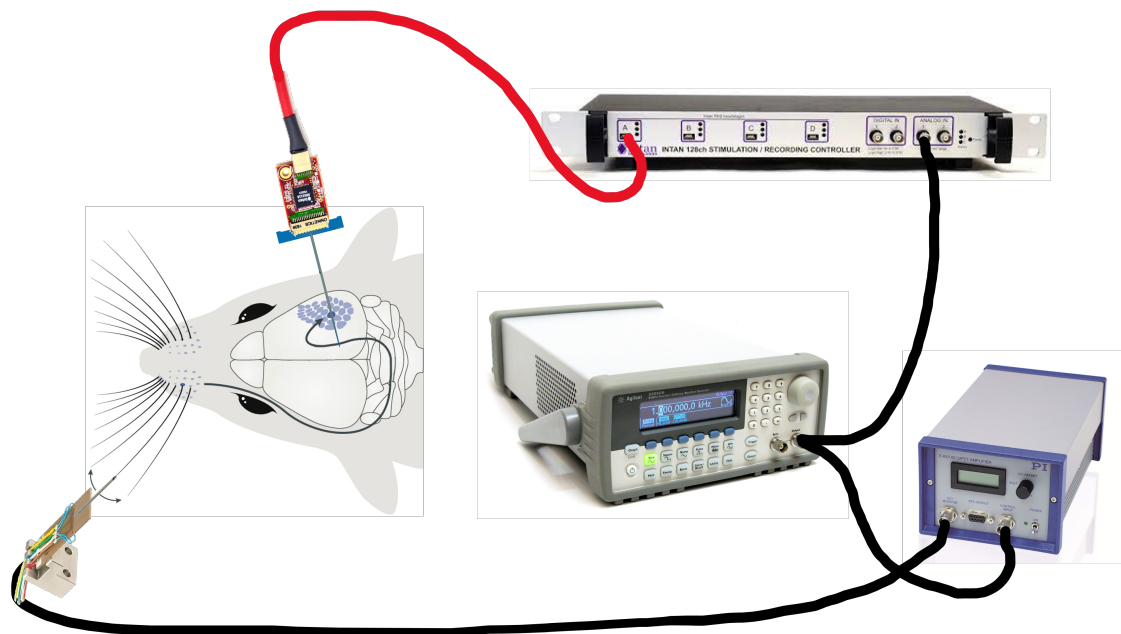
Figure 2.3: Whisker stimulation setup sketch. The piezoelectric whisker bender is used to precisely stimulate a single vibrissae. The controller of the piezoelectric is governed by a signal generator to set the stimulation amplitude and duration, whose output is recorded synchronously to the neural signal by the Intan stimulation/recording controller.

states during urethane anesthesia [102].

2.2.1 WHISKER STIMULATION

Stimulation of the whisker is administered mechanically in sets of multiple trials with the same characteristics by inserting a single contralateral whisker into a 25G hypodermic needle (BD Plastipak, Madrid, Spain) attached to a multilayer piezoelectric bender with integrated strain gauges (P-871.122, Physik Instrumente, Karlsruhe, Germany). The bender is rapidly displaced by controlling it with a power amplifier (E-650.00, Physik Instrumente, Karlsruhe, Germany). The contralateral whisker relative to the recording barrel is cut to 10 mm and inserted 8 mm into the cannula and stimulated by a displacement of the cannula of 5 ms duration and 100 μs rise/fall time. The setup is sketched in Figure 2.3. Data are collected in sets of stimulation trials that are administered every 10 seconds. This long time between stimuli ensures protection against any dynamic adaptation to stimuli [103].
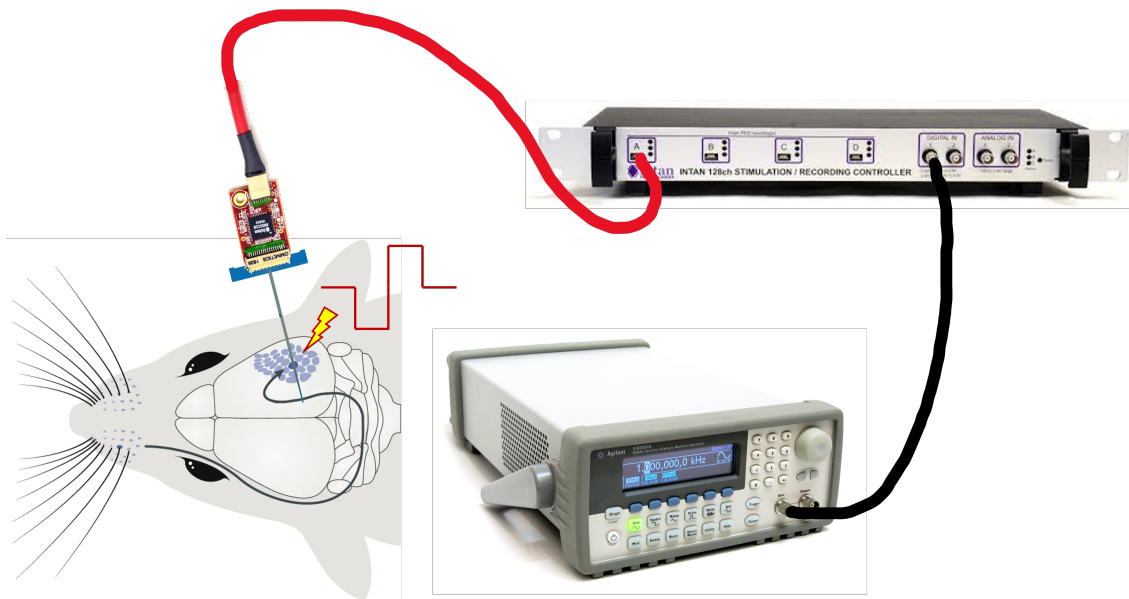
Figure 2.4: ICMS setup sketch. The signal generator is used to trigger the ICMS, managed by the Intan stimulation/recording controller.

2.2.2 SINGLE PULSE OF MICROSTIMULATION

ICMSs are administered in sets of multiple trials with the same shape and characteristics. ICMS is governed by current and consists of a biphasic pulse given with a negative and positive phase symmetrical to zero, whose duration is 200 μs each. ICMS is applied in a range of amplitudes from $\pm$5 μA to the maximum voltage supplied by the instrument of 7 V, corresponding to a maximum current between $\pm$25 and $\pm$30 μA depending on the animal. The total injected charge resulting per pulse ranges from 1 to 5∼6 nC. The stimulation electrode is chosen for the experiments depending on the position of the probe and the cortical layer to stimulate. Data are collected in sets of 30 or 60 stimulation trials, administered every 5 or 10 seconds, and each set includes a single amplitude and a single phase duration. The setup is sketched in Figure 2.4. The amplitude, duration, shape, and combination of pulses are chosen based on work found in the literature [104, 105, 106] and on previous trials and experiments carried out in our laboratory.

2.2.3 TRAINS OF MICROSTIMULATIONS

Trains of ICMSs are administered in sets of multiple trials with the same shape and frequency. Pulse bursts have a duration of 1 second and are given at a specified frequency between 6, 8, 10, 12, 14, and 20 Hz. The amplitude of the first pulse is fixed to 25 μA, while the rest of the pulses can assume a single value between 5, 10, 15, or 20 μA. The first, stronger pulse has the role of evoking the spindle response, the subsequent pulses aim at modulating it. The total injected charge resulting per pulse ranges from 1 to 5 nC. An electrode is chosen as the target to apply the first ICMS and the following pulses of the bursts are given by the electrode immediately above. The target layer is the VI, thanks to a previous investigation of the most effective depth of stimulation. ICMS is governed by current and consists of a train of biphasic pulses of the same shape, with a negative and positive phase symmetric to zero, whose duration is 200 μs each. Data are collected in sets of 30 bursts of stimulation, triggered every 10 seconds. Each set includes a single amplitude and a single stimulation frequency. The setup is the same as sketched in Figure 2.4.
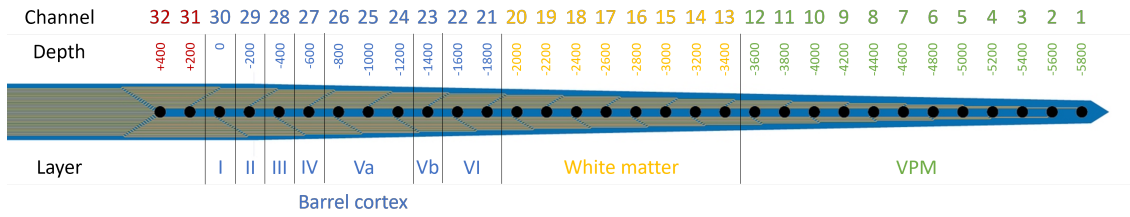
Figure 2.5: Atlas Neuro E32+R-200-S1-L6 NT tip showing channels number, depth and layer placement of the electrodes in the barrel cortex.

2.3 CORTICOTHALAMIC RECORDINGS

To investigate the behavior of the oscillation, we recorded data from the barrel cortex and the VPM of the thalamus simultaneously, to determine whether any thalamocortical loop was involved in the sustenance of the oscillation. For this purpose, we changed the recording site to a peripheral barrel (from C1 to B3), to record from both the barrel and the thalamus using a single longer probe (Atlas Neuro E32+R-65-S1-L6 NT, 32 channels, 200 μm pitch), positioned as in Figure 2.6. The recording setting and the stimulation protocols remained the same as previously described 2.2, with the channel number and location as in Figure 2.5. The surgery procedure remained the same as 2.1, except for the insertion coordinates that changed to -2.9 AP, $+6.4$ ML.
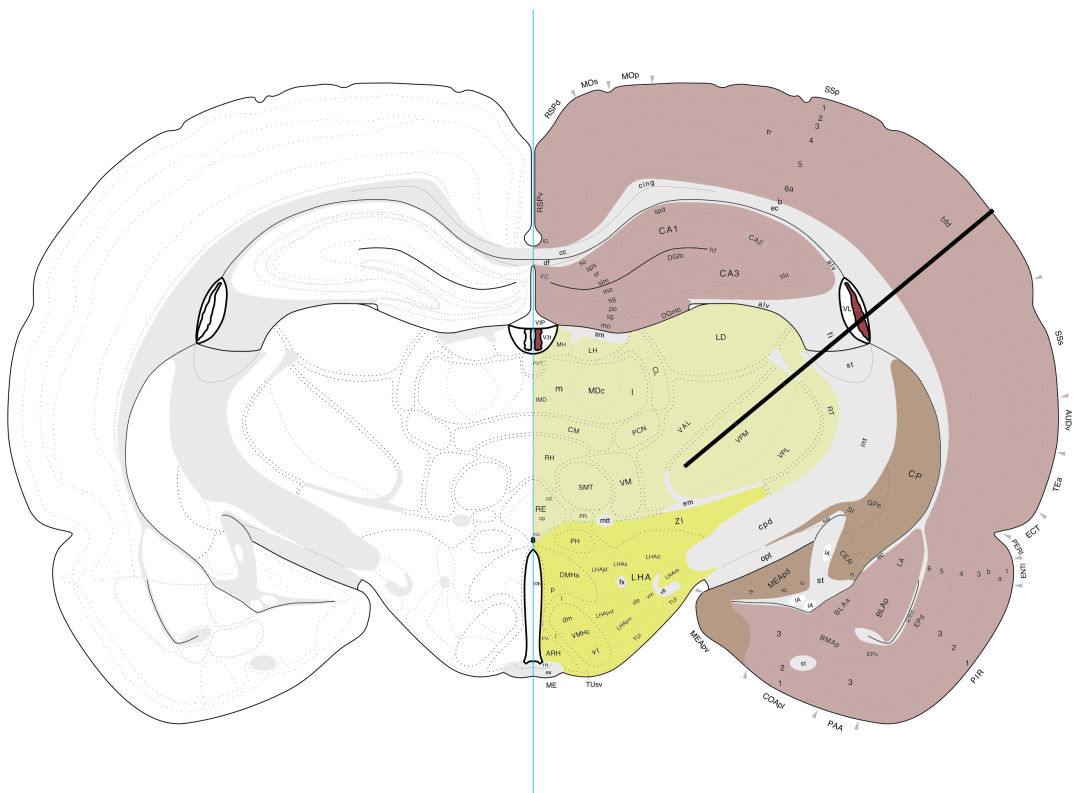
Figure 2.6: Atlas Neuro E32+R-200-S1-L6 NT placement to record from the barrel cortex and the VPM of the thalamus simultaneously. Black line indicates the position of the probe needle.

3

Methods

3.1 ANALYSIS

Analysis of biological data is conducted in MATLAB R2021a, MathWorks Inc., using custom scripts and follows two different pipelines for spikes and LFP. Having the stimulation and the recording on a single probe and a single insertion point provides great flexibility, but also comes with some disadvantages. The voltage applied to the electrodes for stimulation is orders of magnitude greater than the sensed neural activity. This causes the ICMS to introduce an artifact with exponential decay and non-linear effects that spreads differently depending on the physical placement of both the on-chip ADC and the electrodes in the tissue, with huge artifacts that pollute the recording. To reduce the impact of the stimulation artifact such as saturation of the amplifier and slower recovery, the signal is grounded for the duration of the applied pulses during the acquisition of the signal. Then, given the different frequency bands where events are investigated in the LFPs and the spiking activity, the artifact reduction is managed and mitigated differently for the two analyses.

3.1.1 LOCAL FIELD POTENTIAL ANALYSIS

LFPs are evaluated in the 4 to 100 Hz band, including theta, alpha, beta, and gamma. The slower component of the delta is too weak compared to the in-band power of the artifact to be informative. Any artifactual periodicity in the signal is found by the power spectrum of the signal and is possibly removed by a notch filter. To mitigate the artifact generated by the stimulation, the 25 ms after every stimulation onset on each channel are overwritten with the last known pre-stimulus value. The remaining signals, from 25 ms to the end of the post-stimuli considered window, are extracted and averaged between trials of the same set. This average is lowpass-filtered at 4 Hz by a Butterworth filter of the 1st order applied in forward and reverse, and subtracted to each trial to remove the artifact drift. The cleaned signals are then aligned with the end of the overwritten part of the signal and filtered by a Butterworth bandpass filter of the 2nd order in forward and reverse to achieve a linear phase. The signal spectrograms shown here are computed with a time resolution of 800 ms and an overlap of the segment of 99%. Finally, the intra-experiment delay variability is evaluated by cross-correlating the LFP of each trial with the LFP trials average and is estimated as the standard deviation of the peak lags.

The adopted spike detection method allows to identify both isolated APs and MUAs from the raw recording; the signals are filtered with a 3rd order bandpass Butterworth filter with a cutoff frequency (-3 dB) of 300 Hz for the lower frequency and 4 kHz for the higher frequency. The spatial average of the signal recorded by the 32 channels is subtracted from the signal of each channel to reduce the correlated noise. Spikes and MUA are recognized by detecting negative peaks below a threshold of 4 times the median of the absolute value of the signal divided by 0.675 [107].

If the recordings in the thalamus normally show APs with an amplitude in the range of hundred of μV in most of the electrodes, the activity recorded by the electrodes in the barrel cortex rarely shows any clear and strong spikes. The predominant activity consists of MUA, intended as a burst of spikes originated by an ensemble of activity of a population of neurons of some tens of μV amplitude, as it will be shown in Chapter 4 in Figure 4.20. The firing rate estimated by accumulating the spikes in a moving window of 10 ms from channels belonging to the same layer, well emphasizes these MUA, which result in a sharp and peaked increase of the firing profile. So, by accumulating this *noisy* activity we still achieve meaningful insight of the underlying dynamics coherent with the information provided, for example, by LFP.

During each applied stimulation, the signal shows a sharp transient due to electrode grounding and charge remaining at the electrode/tissue interface. Also, the noise in the signal is higher with respect to the baseline for some milliseconds. To help the filter to converge quicker to a steadier regime and to not pollute the noise estimation used to draw the detection threshold, the signal after the filtering is overwritten with a 0 value from the onset of the stimuli until 15 ms later, and no (mostly) false events can be detected. An example of the post-filtering artifact will be shown in Chapter 4 in Figure 4.19.

To check for the presence of the spindle response evoked by ICMS in each set, the periodicity of the signal is estimated by the autocorrelation of the 1 second post-stimulus spiking activity. The sum of the spiking activity found on all the channels is autocorrelated for a length of 250 ms for each trial (to find periodicity down to 4 Hz) and averaged over the set. The greatest peak non-centered in zero, if present, is compared against a threshold to find the frequency of the eventual evoked spindle. The threshold is found by a permutation test by shuffling the position of the spikes of each trial and repeating the

previous steps. Each threshold point is taken as the 95% maximum value reached by the average auto-correlation of the shuffled spikes for that delay. Similarly, the response delay was estimated by finding the first firing rate peak after the stimuli in the firing activity averaged per trial. Each result is finally visually inspected to check for artifacts or errors that could distort the signal and lead to a wrong detection or result and possibly manually adjusted.

The study of the response evoked by the train of stimulations is performed on the spiking activity only. In fact, the large artifacts induced by ICMS alter the signal in the LFP frequencies of interest for the spindle, for a duration longer than the stimulation period. Also, compared to LFP, spike provides a better time resolution, required to identify the small variation in the frequency shift determining the Arnold's tongue.

The recordings and the power spectrum of the signals are visually inspected both before and after the filtering to check for unexpected artifacts or suspicious periodicities. The recording will be discarded if the signal is seriously compromised and it cannot be fixed, for example, by applying a notch filter or by removing a recording part or a defective channel. This causes the robustness of the SNEO –that will be discussed in Section 3.2.3– against supra-threshold signals outside the spike duration to be redundant, and for this reason a simpler detection method is preferred. Also, working offline, the threshold can be estimated accurately from the entire recording, using time consuming methods as the median. With this in mind, on average, the two methods produce very similar results.

3.2 Electrophysiology setup development

This section is adapted from my work published in the Digital Journal (Tambaro et al., 2021 [108]).

The biological interface setup is developed on top of the Intan Technologies RHS stimulation/recording controller, with the aim of a reliable integration with the systems developed by the other closed-loop participants. The stimulation/recording controller interfaces with two RHS2116 chips from Intan Technologies (Los Angeles, California, USA) to record and stimulate the probe implanted in the anesthetized animal brain. The controller is governed via a computer through an open-source application built on a developer interface designated RhythmStim, that consists of a hardware/software mixture of Verilog HDL code and C++/Qt API written for the Opal Kelly XEM6010 USB FPGA. RhythmStim is used to configure the Xilinx FPGA on the Opal Kelly module to communicate with the RHS2116 chips over SPI buses and to stream data blocks containing multiple samples of each probe channel and the different input/output ports from these chips to a host computer over USB connection, exposing all the features of the headstage and the controller previously mentioned. Both the host computer to FPGA software interface and the FPGA to headstage hardware interface are fully open source and customizable. A single headstage is interfaced with the Intan RHS Stim/Recording controller that is connected in turn to a host computer running the Intan Stim/Recording Controller software based on the RhythmStim API. For the closed-loop purpose, the system must be able to detect activity in the animal brain as AP and MUA and to communicate them to the closed-loop CU. Moreover, it must be able to stimulate the brain tissue with current pulses using the electrodes when required by the CU. For this reason, the spike detection algorithm is implemented directly in hardware on FPGA and the Intan software is extended with the following features:

- on-line spikes detection

- events information embedding and communication

- external stimulation commands reception

- stimulation artifact rejection

- events logging

The integration relies on two main strategies depending on the participants' physical location: one based on an Internet-oriented communication and one based on a local-oriented communication.

3.2.1 PRELIMINARY SOFTWARE IMPLEMENTATION

For remote communication of the first stages of the project, experiments have been conducted with the systems of the participants physically placed in different areas. A communication based on the user datagram protocol (UDP) transmission protocol reliant on a private mesh network is used to connect the systems. To interface the RHS controller with the network, spike detection operations have been delegated to the host computer running a custom version of the acquisition software. The software has been modified to stream events detected by a set-by-hand threshold crossing spike detection algorithm running in real-time, while stimulating on trigger received; it also implemented the filtering of the signal and the events logging on disk. Using a traditional computer architecture to detect and send events introduces a variable latency of a few milliseconds due to the USB connection with the recording system and the software elaboration time –and the same for the stimulation command–; anyway this is not a serious limitation for the remote closed-loop, given that in this scenario the latencies are mostly dominated by the time required by the packets to travel through the network (dozens of milliseconds) and its variability. The spike detection is executed in parallel on different threads for different channels, allowing for simultaneous multichannel event detection on a multicore host computer. To deal with the stimulation artifact, the signal is forced to zero for a window of few milliseconds whenever a stimulation occurred, to avoid detecting false events during the large fluctuation induced by the stimulations. A high-level view of the main developed software loop is shown in Figure 3.1.

3.2.2 LOW-LATENCY SPIKE DETECTION

In order to process the information that relies behind the voltage fluctuations detected by the sensing spots on the probes, the acquired signal must be digitally sampled with a frequency high enough to discern the activity up to the fast depolarization of a single neuron, called AP or spike, and MUA. To accurately reconstruct this activity, as short as 1 ms, samples must be collected at a high sampling frequency of up to 30-40 kHz. Given the large number of channels featured by the most recent probes [6, 109, 110], the number of samples generated per second can be difficult to process in real-time, precluding experi-
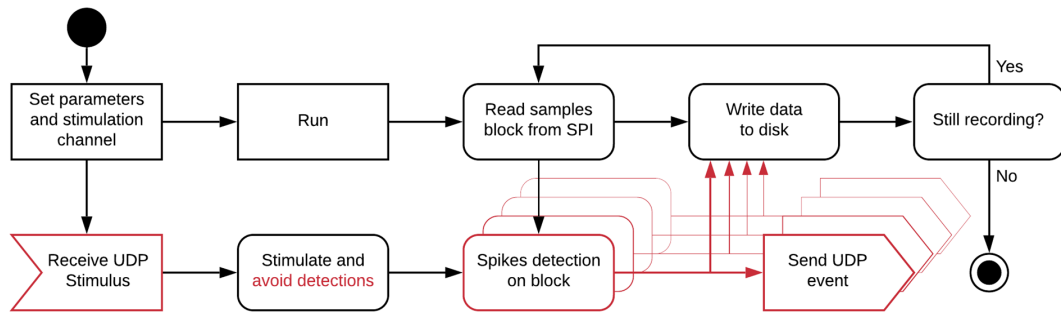
Figure 3.1: Block diagram of the acquisition, streaming and, stimulation trigger reception. In black the default capability of the controller, in red the component developed for the purpose of the closed-loop experiment.

ments where the latency in the recognition of activity events is crucial. For example, when dealing with spike-dependent closed-loop experiments for brain-computer interfacing involving ICMS [111, 112], keeping the feedback timing in a biologically acceptable range can be a critical step [113, 114, 115]. This work aims to overcome the detection latency limitation of a common software implementation; traditional processing of the information is subjected to the USB communication latency necessary to transfer the samples in chunks from the acquisition system to a computer, where the samples processing is, in turn, conditioned by the operating system scheduler, blocking calls, and computer performances. Altogether, these constraints cause tens of milliseconds of delay from the sampling of the neural activity to its elaboration and interpretation.

Here is described a digital spike detector running in the FPGA of the recording system, which elaborates the neural activity received directly from the headstage, which samples the signals acquired by the microelectrodes without intermediate steps. The headstage, mounted on the top of the probe, embeds up to two chips each managing 16 electrodes and including a low noise amplifier, a 16 bit Analog-to-Digital Converter (ADC), high-pass and low-pass filters, and stimulation circuitry. Processing the data in-place on the recording system allows evaluating the digitalized signal point-by-point with the lowest latency from the ADC, and communicating the temporal and spatial firing information of each of the 32 channels in less than 1 ms from the maximum negative peak of the spikes. The project has been integrated into the open source hardware description language (HDL) code and acquisition software RhythmStim from Intan Technologies (Los Angeles, California, USA) and deployed on the RHS

stimulation/recording controller from the same company. The logic managing the sampling and data transmission has been added alongside, creating a new dedicated pipeline to process the raw data stream acquired by the 32 channels headstage without reducing the original functionalities. The spike detection pipeline starts without any buffering system when receiving a new sample, guaranteeing the lowest latency from digitalization to processing. The spike detection method included in the system by default works by detecting when the first order high-pass filtered signal crosses a threshold set by the user on a subset of a monitored channel, raising the signal of one of the mapped digital outputs of the system. The spike detector presented in this work wants to replace and improve both the communication of events and the detection capability of the system in identify APs and MUAs, despite the good noise performance at high frequencies. Our experiments found the instrument noise at the high frequency band of AP and MUA to be about 10 μV RMS during neuronal inactivity, making it trivial to detect APs that can reach amplitudes down to -150 μV when neurons are close to the electrode surface. Unfortunately, in many experiments, these strong signals represent a minority, most of the signals originate from neurons that are far from the electrodes, leading to MUAs of about 15 μV RMS and a Signal-to-Noise Ratio (SNR) of 3.5 dB once the signal is filtered. Therefore, we need a more powerful tool capable of accurately detecting both the AP and MUA events. The presented spike detector design includes:

- A 3rd order Butterworth high-pass infinite input response (IIR) filter with a cutoff frequency of 300 Hz and a Savitzky-Golay smoothing filter [116], fitting the high-pass filtered signal with a 2nd degree polynomial.

- A point-by-point signal energy estimation using the SNEO [117], that aggregates both the frequency and the amplitude of the voltage fluctuations in a series of samples that can be compared with a threshold.

- A novel dynamic threshold per-channel estimation based on the Root Mean Square (RMS) of the SNEO output that accommodates any drift of the probe or changes in the signal quality, that rapidly converges to a firing-independent value close to an ideal threshold based only on the noise energy. The threshold can be adjusted by the user to open the detection of both the single AP and MUA.

- A post-ICMS blind window of a user-defined duration, to prevent the detection of false positives following the high increase in the signal power due to the artifact induced by the injection of a current.

- The capability to stream the amplitude, the channel, and the timing of each detected spikes via the USB to the host computer, and, simultaneously, via the UART protocol to any other connected device with sub-milliseconds latency. By the UART command, it is also possible to trigger the ICMS set from the host application.

The software application on the host computer used to manage the connection, recording and setting of the stimulation/recording controller system has been extended to manage the new functions. A new dedicated graphical user interface (GUI) to manage the spike detector has been created to show a real-time raster plot of the spiking activity of each channel and to allow adjustment of the threshold multiplier and the artifact blanking window during the experiment to improve the spike detection performance. Through the application, the system can also be connected to the network to stream the spikes details to a specified IP address over the UDP protocol. Finally, channels can be excluded from the spike detection so that they are not sent via both UART and UDP. The system has been tested with in vivo experiments on the barrel cortex of anesthetized rats and it is currently used in our laboratory for closed-loop experiments of ICMS. Examples of the system output on APs and MUAs detection are highlighted.

3.2.3 ALGORITHMS DESIGN & IMPLEMENTATION

The digital implementation of the spike detector is based on an algorithmic processing that can be divided into six major steps. High-pass filtering, Savitzky-Golay fitting, SNEO, threshold estimation, detection, and local minimum finder. These core parts are described here, together with the parameters used for an implementation running with a sampling frequency of 25 kHz for each of the 32 channels. The input is assumed as a matrix where the first index indicates the electrode number, or channel, while the second index reports the sampled amplitude of the signal. The information to extract from the signals is given by the index where the spiking events are detected for each channel and the corresponding amplitude. The output then is a sparse matrix with the input shape, containing the negative amplitude of the filtered signal where a spike is detected. The parameters –length of the Savitzky-Golay window, k for the SNEO and the threshold multiplier– are tuned both by simulation and experimentally to achieve better accuracy. Synthetic datasets are created with spikes templates of different amplitudes and SNR inserted in the known positions. In this case, the accuracy is focused on the single AP detection and is

calculated from the ratio between the correctly detected events and the sum of the total events and the false positives. The results achieved by varying the parameters of the algorithm are then compared to maximize the accuracy. The analysis is not shown here for the sake of brevity, but the method follows what I provided in [118]. Acquisitions from experiments are then used to fine tune what has been found by the simulation, where it is possible to also evaluate the MUA detection.

These algorithms have been described in HDL language to be implemented on the Opal Kelly XEM6010-LX45 board that mounts the Xilinx Spartan-6 XC6SLX45-2 FPGA. This board is mounted by default by the Intan RHS stimulation/recording controller and together with the RhythmStim design provides the interface between a host computer and the headstages (up to 4). Each headstage is connected through a Serial Peripheral Interface (SPI) cable to the recording system, used to simultaneously communicate two digitalized samples. The RhythmStim allows for the acquisition of data for both visualization and recording on the host computer application. The application is used to set the filters on the head stages and to program the latter to stimulate a channel with a user-defined current shape based on different external trigger sources connected to the recording system. The RhythmStim hardware part manages the acquisition of samples from each channel at a constant frequency of 20, 25, or 30 kHz and the ICMS when it is triggered. In a high-level overview, the system continuously loops over 20 action slots: the last four slots are used to start and stop the ICMS and to set the parameters of the headstages, while in the other first 16 slots, a 32 bit command is sent via SPI to sample a different pair of channels. The headstage answers after a delay of two slots with a pair of values of 32 bit, each containing the sampled value in the 16 Most Significant bit (MSB), stored with a positive offset of 32'768, where the least significant bit of the value corresponds to 0.195 μV. The pair is written in the RAM of the Opal Kelly board (Portland, Oregon, USA), which is used as a buffer for the asynchronous USB communication with the host application. The design has been modified to write the 16 MSB of both the samples pair, received from the headstage connected to the system port D, also in a 64 bit width First-In First-Out (FIFO), filling the other 32 bit with a system timestamp representing the number of samples acquired. The FIFO crosses the domain clock and provides to the spike detector the values at the working frequency of 100 MHz. Here, the spike detection pipeline begins, whose main steps of the process are described in Figure 3.2.

The values are read as soon as the FIFO is not empty and the two samples are converted in two's complement removing the positive offset of 32'768. The spike detection design is split into different
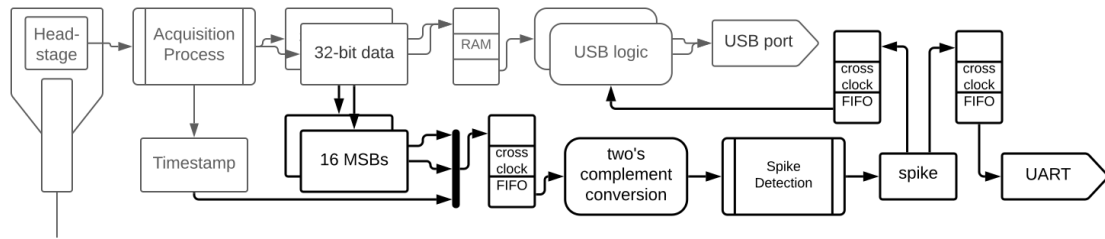
Figure 3.2: Block diagram of the system. In faded the existing parts, in bold the pipeline added for the spike detector.
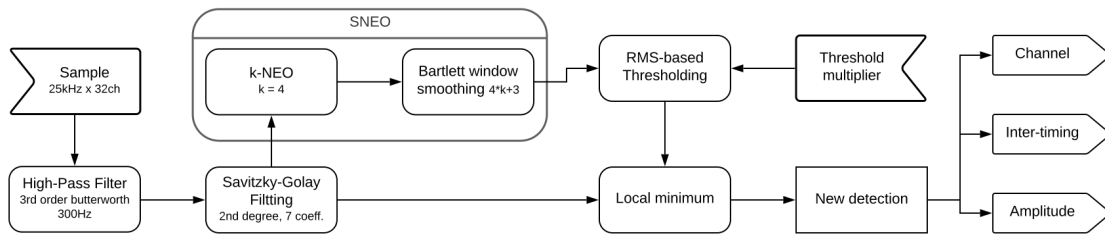
Figure 3.3: Spike detection pipeline.

HDL components described in the next subsections. These components are orchestrated by a main design that allows the various output to flow from one component to the next, keeping the channel and the samples count. The samples pair is processed sequentially through the pipeline shown in Figure 3.3, one sample immediately after the other. Processing is tuned for a sampling frequency of 25 kHz. The spike detector can also work with a 16 channels headstage, since the second value of each samples pair will simply have a constant value of 0. As the main design rules, the operations are performed in the integer domain. Where a division is required, it is constrained to a power of two, to be performed as a bit-shift operation –a 0.5 rounding precision is achieved performing the n bit-shifting operation on the value summed to $2^{(n-1)}$–. All components work in time division multiplexing over the 32 channels, storing each channel state. The HDL part of the project has been developed on the Xilinx ISE Design Suite 14.7. The pseudocode of the components can be found at the end of this section.

The pseudocode of the main algorithms used to create the spike detector design can be found below the section of each component. Note that, in the sake of simplicity, the pseudocode ignores the time division multiplexing depending on the channel. The states variables are independent from the procedure life and keep their value between multiple procedure calls. Where the initialization value of a variable is relevant, the value is specified.

43
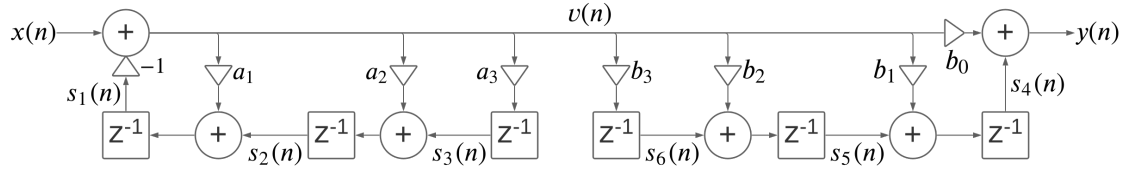
Figure 3.4: IIR filter direct-transposed form I structure.

	Coefficients				Rounding Error (%)			
	0	1	2	3	0	1	2	3
a	30.388	-91.163	91.163	-30.388	0.0021	0.0010	0.0010	0.0021
b	32.768	-93.364	88.789	-28.180	0	0.0009	0.0001	0.0008

Table 3.1: **Coefficients of the 3rd order IIR filter** scaled by the scaling factor of 2^{15} and the percentage error introduced from the integer rounding.

High pass filter

When dealing with signals such as APs and MUA characterized by high frequency features, the first step of the processing chain is to high-pass filter the signal, to exclude the LFP from the further analysis, to remove the predominant low frequency components of the signal below 300 Hz. Here, a 3rd order IIR Butterworth filter is used, to remove the low frequency changing features of the LFP, offset, and off-band noise. The filter coefficients in Table 1 are computed using MATLAB and are used to implement the IIR filter with a cutoff frequency of 300 Hz.

Direct and direct-transposed from I and II have been simulated for the FPGA integer-based implementation of the 3rd order IIR filter. Using the direct-transposed form I (Figure 3.4), the state variables of the filter did not saturate and the filter remained stable despite the rounding error on the output, avoiding using a cascade of second-order filters. Being the coefficients real numbers close to the 0 value, the error introduced by the rounding would be disastrous. To overcome this problem working in the integer domain, the coefficients are scaled by a factor big enough to reduce the rounding error to a negligible one. This scaling factor is chosen as a power of 2, to be then removed from the filter output with a bit-shift operation. The filter form fits well to the DSP48A1 multiplier/adder of the Spartan-6, that provides a signed multiplication of 18 bit per operand, followed by a 48 bit adder. Two DSPs are used to create a 35 × 18 bit fully pipelined multiplier with a 48 bit adder after the multiplication stage. The

six filter state variables of the 32 channels are stored in a 48 bit width block RAM (BRAM), where the state variables of each channel are mapped. A scaling factor of 2^{15} is chosen to scale the filter coefficients to fit the 18 bit signed input of the multiplier, knowing that it does not exceed the limit of $\pm 2^{17}$. In Table 3.1, the integer coefficients are shown with the percentage rounding error. For each new sample to filter, the sum of the 16 bit value of the new sample with the state $s_4(n)$ is tied in the input on the 35 bit multiplicand port. This value is reduced by the scaling factor and is resized to 35 bit without losing any information. The filter coefficients are given sequentially on the 18 bit multiplier port and the corresponding channel state variable is given on the 48 bit sum port to compute all the new state values. The filter output, reduced by the scaling factor, can be safely resized to 16 bit. Even if it is smaller on average compared to the input, the output bit width is kept the same since an eventual stimulation artifact can cause the signal to span the entire range even after the filtering.

In Algorithm 3.1, IIR high-pass filtering, the new acquired sample is given in the input, and a new filtered sample is returned. The a and b coefficients are scaled by the 2^{15} factor and rounded, the s variables are the filter internal states.

Algorithm 3.1 IIR high-pass filter

    state variables a_1, a_2, a_3 : integer $\leftarrow$ filter 'a' coefficients $\times$ 2^{15}

    state variables b_0, b_1, b_2, b_3 : integer $\leftarrow$ filter 'b' coefficients $\times$ 2^{15}

    state variables $s_1, s_2, s_3, s_4, s_5, s_6$: integer $\leftarrow$ 0

    procedure FILTER(*unfiltered_sample* : integer)

        variable *filtered_sample* : integer

        variable v : integer

        $v \leftarrow$ *unfiltered_sample* $- s_1/2^{15}$

        filtered_sample $\leftarrow (v \times b_0 + s_4)/2^{15}$

        $s_1 \leftarrow v \times a_1 + s_2$

        $s_2 \leftarrow v \times a_2 + s_3$

        $s_3 \leftarrow v \times a_3 + 2^{14}$

        $s_4 \leftarrow v \times b_1 + s_5$

        $s_5 \leftarrow v \times b_2 + s_6$

        $s_6 \leftarrow v \times b_3 + 2^{14}$

        return *filtered_sample*

    end procedure
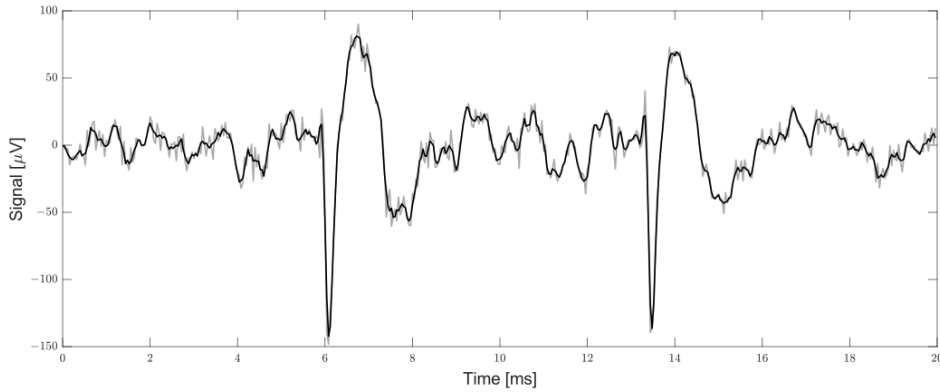
Figure 3.5: A 20 ms acquisition of extracellular signal from the rat barrel cortex. Two strong extracellular spikes are recorded at 6 and 14 ms, propagated from a neuron near the recording electrode. In gray, the high-pass filtered signal with a cutoff frequency of 300 Hz. In black, the signal fitted with the Savitzky-Golay filter.

Mask	0	1	2	3	4	5	6
a	0.9274	−2.7821	2.7821	−0.9274	n/a	n/a	n/a
b	1	−2.8492	2.7096	−0.8600	n/a	n/a	n/a
SG	−0.0952	0.1429	0.2857	0.3333	0.2857	0.1429	−0.0952

Table 3.2: Coefficients of the 3rd order IIR filter (a and b), and for the Savitzky-Golay (SG) fitting.

SAVITZKY-GOLAY FITTING

The filtering step is immediately followed by the smoothing Savitzky-Golay filter, used to fit the last seven points of the high-pass filtered signal with a second-order polynomial at each iteration. The signal is convoluted by the seven coefficients mask shown in Table 3.2, providing a cutoff frequency of −3 dB at 3 kHz. This results in less sharp high frequency changes, increasing the SNEO performances as demonstrated in [119]. A fitting example of an extracellular signal is shown in Figure 3.5.

The Savitzky-Golay implementation consists in a convolution of the seven coefficients mask with the last seven samples of every channel. Similarly to the high-pass filter, the seven coefficients of the 2nd grade polynomial fitting are multiplied by a scaling factor. The coefficients can safely be scaled by a factor of 2^{18}, without exceeding the signed range of an 18 bit word. The last seven values of each channel are stored in a 16 bit width BRAM. The last six samples are ordered in BRAM by channel (i.e., ch1-sample1, ..., ch1-sample6, ..., ch32-sample1, ch32-sample 6) to be linearly indexed. The convolu-

tion exploits DSP48A1, configured in an 18 × 18 bit multiply and accumulate mode. Each sample is extracted sequentially from the BRAM and is multiplied by its respective coefficient with the DSP multiplier, the result is then accumulated in the 48 bit register. Each sample, when read from the BRAM, is reinserted as one position delayed—except for the sixth which is discarded—and the new sample is inserted first, to achieve the behavior of a shift register. The accumulation register is reset to a value of 2^{17} before receiving any new samples, to account for the 0.5 rounding of the bit shift division used to remove the scale factor from the convolution output. The average error introduced by the rounding after the scaling is 0.0004%.

In Algorithm 3.2, Savitzky-Golay fitting, the output of the high-pass filter is given in the input and a fitted new sample is returned. The mask coefficients are hard coded scaled by the 2^{18} factor and rounded, the samples array is used to keep the last seven samples.

Algorithm 3.2 Savitzky-Golay filter

    state variables mask : integer[7] ← Savitzky-Golay coefficients × 2^{18}

    state variables samples : integer[7] ← [0]

    procedure SAVITZKY-GOLAY(filtered_sample : integer)

        variable fitted_sample : integer ← 2^{17}

        for i ← 7 **downto** 2

            samples[i] ← samples[i-1]

        end for

        samples[1] ← filtered_sample

        for i ← 1 **to** 7

            fitted_sample ← fitted_sample + samples[i] × mask[i]

        end for

        fitted_sample ← fitted_sample / 2^{18}

        return fitted_sample

    end procedure

The *kNEO*, on which the SNEO is based, gives an instantaneous estimate of the energy contained in a signal oscillation. Thanks to the energy-dependent response, SNEO became widely used for the spike detection task and is still one of the preferred methods when performing real-time processing [120, 121, 122, 123]. It fits very well in a real-time and low-latency application since it does not require any training phase and has a small footprint on resource usage, nevertheless good performance, as proved and compared in my previous work [118]. This operator strictly relies on a parameter called *k*, which depends on the sampling frequency and the average spike duration. Given the sampling frequency of 25 kHz, the average spike duration, and the experimental tuning, the parameter value *k* that achieves the best detection accuracy results has been found to be 4. After computing the nonlinear energy response of every sample *t* of the filtered signal *s* of each channel *ch*, the SNEO smooths it with a Bartlett window *BW* of size $4 \times k + 1$ (Equation 3.1).

$$kNEO(ch, t) = s(ch, t)^2 - s(ch, t + k) \times s(ch, t - k) \qquad \forall t | t \in \{k + 1, ..., |s| - k\}$$

$$SNEO = kNEO \otimes BW(4 \times k + 1)$$

(3.1)

The operations of the SNEO implementation involve two DSP48A1 configured in a 35×18 bit fully pipelined multiply and accumulate mode and a 35 bit width BRAM. The component receives three samples depending on the SNEO parameter *k*, to compute the new signal energy value of a 35 bit width as shown in the first row of Equation 3.1. Both the BRAM organization and convolution with the Bartlett window are implemented as in the Savitzky-Golay component, but with a convolution length of 17. The input of a multiplier of 35 bit is required due to the width of the energy value. The Bartlett window is scaled by a factor of 2^{16}, which introduces an average error of 0.0025%. Therefore, the accumulation register starts with a value of 2^{15} for the bit shift of 0.5 rounding.

In Algorithm 3.3, SNEO, the last value output from the Savitzky-Golay fitting is taken in input, and the signal energy is returned. The Bartlett windows are hard coded scaled by the 2^{16} factor and rounded, the samples and energies arrays are used to keep the last 17 samples and 17 kNEO output.

Algorithm 3.3 SNEO

---

    state variables bartlett_window : integer[17] ← Bartlett coefficients × 2^{16}

    state variables energies : integer[17] ← [0]

    state variables samples : integer[17] ← [0]

    procedure SNEO(fitted_samples : integer)

        variable smoothed_energy : integer ← 2^{15}

        for i ← 9 **downto** 2

            samples[i] ← samples[i-1]

        end for

        samples[1] ← fitted_samples

        for i ← 17 **downto** 2

            energies[i] ← energies[i-1]

        end for

        energies[1] ← samples[5]^2 - samples[1] × samples[9]

        for i ← 1 **to** 17

            smoothed_energy ← smoothed_energy + energies[i] × Vartlett_window[i]

        end for

        smoothed_energy ← smoothed_energy / 2^{16}

        return smoothed_energy

    end procedure

The result returned by the SNEO is now compared with a threshold, which must be set to a value accurate enough to discern the physiological events from the signal noise. A fixed value for the threshold can sensibly reduce the detection performances, since each channel has its own SNR level, which can also be subjected to changes caused by probe drifts. A threshold value based on the SNEO output distribution can adaptively adjust the detection level of each individual channel for the entire recording duration. The median is the most reliable option to find an effective threshold using a scaling value, but unfortunately it does not fit well in a real-time hardware implementation pipeline. For this reason, this work relies on the RMS of the signal, multiplied by a scaling factor C to find an accurate threshold which is constantly updated over a window of samples –here called timeframe, tf – long enough to provide a correct and stable trend. However, when using the RMS to find the threshold, it must be considered that the SNEO is a nonlinear operator and the high energy response to a spike will highly affect the RMS value. Being the firing rate intrinsically nonconstant, the RMS output can be sensibly affected with different intensities from timeframe to timeframe and therefore it cannot be simply accounted for in reducing the threshold multiplier C by a constant fraction. To mitigate this problem, this work presents a new approach for the threshold estimation. The signal in each timeframe is compared with the threshold based on the RMS of the prior timeframe. Therefore, the new RMS value can be computed for every timeframe by replacing the samples exceeding the threshold with the RMS from the previous timeframe, to exclude the contribution of the spikes energy from the estimation. Using this approach, the RMS usually converges in a maximum of five iterations to a value close to the RMS value of the noise energy only, independently from the spike amplitude and firing rate, as shown in Figure 3.6. According to this, stimulation artifacts, which could increase the threshold far over the correct level, are also rejected from the RMS estimation. The threshold multiplier C, which scales the RMS value, is chosen by experimental results as in equation 3.2: A value of approximately 5.5 is used for the MUA detection and a greater value up to 18 is used to detect a clear single AP.

$$Th(ch, tf) = C \times RMS(s(ch, t)) \qquad \forall t | t \in tf \qquad (3.2)$$

This component provides a threshold based on the RMS estimation of the SNEO output to each
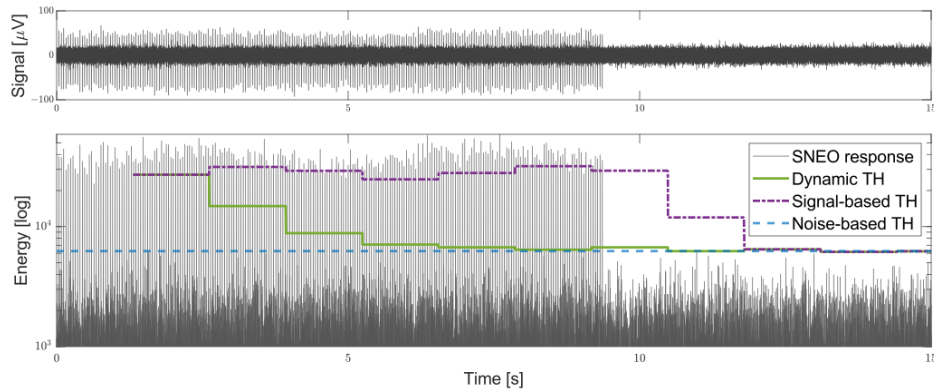
Figure 3.6: spike detection on 15 s synthetic dataset created from an ex-vivo extracellular recording. Top: The ex vivo recording is high-pass filtered at 300 Hz. It does not contain any neuronal activity, thus well representing the instrumental noise floor. A spike template with a negative amplitude of ∼80 μV is generated from the average spikes shape propagated by a neuron nearby the electrode from a filtered in vivo experiment. Twenty-five templates per second are added with a uniform distribution to the ex vivo noise, for a duration of 9.4 s. Bottom: The energy response of the Smoothed Nonlinear Energy Operator (SNEO) is shown in gray. The dashed blue line is the threshold based on the Root Mean Square (RMS) of the filtered ex-vivo energy, representing the value that a spike-independent threshold must ideally have. The solid green line represents the dynamic threshold presented in this work. In comparison, the dash-dotted purple line is the threshold computed on the same timeframes but from the RMS of the entire signal: It is evident how it is largely affected by the firing rate. After the first timeframe where the threshold is not yet computed, a first value is estimated and after four steps the threshold converges to a stable value close to the ideal given by the dash-dotted line.

channel. The RMS is computed incrementally, accumulating the square of the 32 bit energy values of a timeframe. To compute the square of the value, a 35 × 35 bit multiplier based on a single DSP48A1 slice is used. The cumulative sum of the 32 channels is stored in an 85 bit width BRAM. The last thresholds found for each channel and the last 32 RMS values from the previous timeframe are also stored in two 35 bit width BRAM. This allows comparing the energy value with the channel threshold before accumulating it and, in case it is greater, to replace its value with the last RMS value. A counter keeps the number of samples processed and after a timeframe of 2^{15} samples, the square root of the accumulated squared sum is computed with the abacus algorithm, returning an integer approximation of the solution in a variable number of iterations. The result is multiplied by the user-selected multiplier and is stored in the thresholds BRAM.

In Algorithm 3.4, threshold estimation, the SNEO output and the current threshold value are in the input, and the threshold value is returned.

Algorithm 3.4 Threshold

---

state variable counter ← 0

state variable cumulative_squared ← 2^{14}

state variable rms ← 0

state variable threshold ← ∞

procedure THRESHOLD_ESTIMATE(smoothed_energy, threshold_multiplier)

    if smoothed_energy < threshold

        cumulative_squared ← cumulative_squared + smoothed_energy^2

    else

        cumulative_squared ← cumulative_squared + rms^2

    end if

    if counter < 2^{15}

        counter ← counter + 1

    else

        rms ← squared_root(cumulative_squared / 2^{15})

        threshold ← rms × threshold_multiplier

        counter ← 0

        cumulative_squared ← 2^{14}

    end if

    return threshold

end procedure

In a follow-up work, I published another threshold estimation method in [124], which is strongly oriented towards the low-footprint requirements of a real-time implementation. In the work I proposed a noise estimation method relying on the base 2 logarithm, suitable for the automatic setting of a firing-rate independent threshold for spike detection methods. The performances were compared with other statistical variability indices such as the widely used RMS, the mean, and the median of the absolute value of the signal both qualitatively and quantitatively. My results indicate that while the RMS and the mean are heavily affected by the firing rate, this proposed method performs almost equally to the median-based estimation, but the complexity of the latter poses it as an optimal solution for applications requiring a real-time definition of the threshold.

Spike Detection and Local Minimum Finder

For each new sample, the SNEO output is computed and compared with the two previous samples searching for a local maximum and with the threshold found in the previous RMS timeframe (Equation 3.3)). It must be considered that a peak in the SNEO output can be not precisely aligned with the peak in the filtered signal. In fact, depending also on the filtering [125], the positive rebound following the negative spike peak can reach a prominent amplitude in the transition from the negative and the positive phase of the spike, developing enough energy to shift the peak of the SNEO output (Figure 3.7). Therefore, if the output is a local maximum and is also greater than the threshold, the algorithm searches for the minimum value among the previous samples of the filtered signal, within a window wide as the Bartlett window, which is used to smooth the SNEO. Once the minimum is found, the index will represent the temporal information of the spike, while the value will be the amplitude of the spike (Equation 3.4).

$$Peaks(ch, t) = True \ if \begin{cases} SNEO(ch, t-1) \geq Th(ch, tf), & where \ tf \ni t \\ SNEO(ch, t) \leq SNEO(ch, t-1) > SNEO(ch, t-2) \end{cases} \quad (3.3)$$

$$Spike(ch, t') = min(s(ch, t')) \qquad \forall t' | t - 4 \times k + 1 \leq t' \leq t \quad \& \quad Peaks(ch, t) = True \quad (3.4)$$
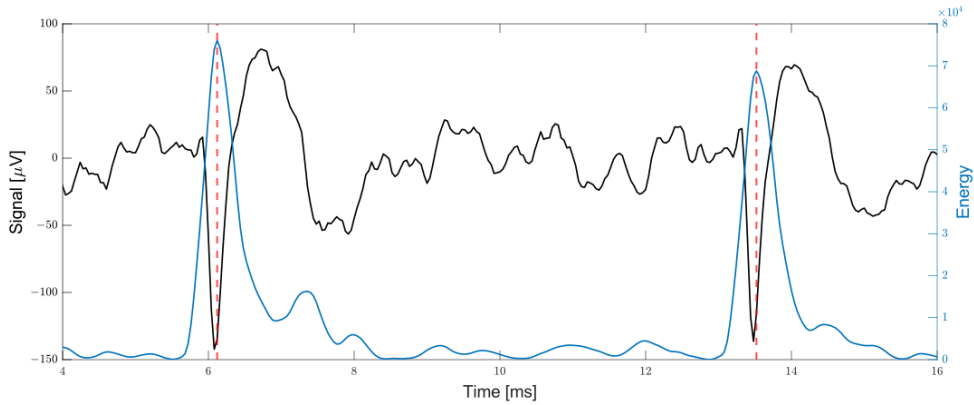
Figure 3.7: An example of two action potentials (APs) recorded from an in vivo experiment. In black, the signal is fitted by the Savitzky-Golay filter. In blue, the energy is computed by the SNEO. The two vertical red dashed lines highlight the peak shifts between the spike and the energy.

For the implementation, whenever a spike is detected, the minimum is found cycling through the last 17 samples of the filtered signal of the channel, stored in a 16 bit width BRAM, to find the maximal negative amplitude. The final timestamp is computed as the difference from the position of the minimum value and the current timestamp, while the amplitude is the minimum value. The timestamp, the amplitude, and the channel of the detected spike are inserted in two different FIFOs. The first is used to cross the clock domain to match the USB communication frequency. Amplitude (16 bit), channel number (8 bit), threshold multiplier (8 bit), and timestamp (32 bit) are written concatenated in the FIFO, which keeps the data count and, thanks to the different aspect-ratio, provides the data in a 16 bit word to the logic managing the USB data transfer. The data count helps a fast transfer of the data to the host computer, as explained in the next subsection. The second FIFO has an 8 bit width, and the timestamp (27 bit) channel number (5 bit), and amplitude (16 bit) of the spike are written in little-endian byte order. This FIFO is used to manage the data transfer via the UART protocol from the high-speed port on the back of the recording system. Data is read and transferred at 8 bit at a baud rate that can be customized in the design.

In Algorithm 3.5, thresholding, the current threshold and the new SNEO output are required in the input, and the spike detection result is returned. The last three SNEO output values are kept in the energies array, which can be merged with the SNEO energies array.

Algorithm 3.5 Thresholding

---

 state variable energies : integer[3] ← [0]

 procedure THRESHOLDING(smoothed_energy, threshold)

  spike_detection : boolean ← **false**

  for $i \leftarrow 3$ **downto** 2

   energies[i] ← energies[i-1]

  end for

  energies[1] ← smoothed_energy

  if energies[2] $\geq$ energies[1] **and** energies[2] $>$ energies[3]

   spike_detection ← **true**

  end if

  return spike_detection

 end procedure

In Algorithm 3.6, minimum finder, the last high-pass filtered sample is taken in the input, as well as the current timestamp and the thresholding output, and the index and the amplitude of the minimum in the last 17 samples are returned. The samples array can be merged with that in the Savitzky-Golay pseudocode.

Algorithm 3.6 Minimum finder

---

state variable samples[17] ← [0]

procedure LOCAL_MINIMUM_FINDER(filtered_sample, spike_detection, timestamp)

    variables amplitude, sample_index : integer ← 0

    variable position : integer ← 0

    for i ← 17 **downto** 2

        samples[i] ← samples[i-1]

    end for

    samples[1] ← filtered_sample

    if spike_detection = true

        for i ← 1 **to** 17

            if samples[i] < amplitude

                amplitude ← samples[i]

                sample_index ← i

            end if

        end for

    end if

    position ← timestamp - sample_index

    return [amplitude, position]

end procedure

The open-source software of the RhythmStim for the host computer has been modified (with Qt 5.15.1) to support the new features introduced in the acquisition system. By default, the software manages the data transfer from the acquisition system to the computer thanks to the USB communication provided by the PipeOut construct of the Opal Kelly board and manages the transfer of data via USB. On the HDL side, the PipeOut is instantiated on a specific endpoint, an address, and it is interfaced with the read-side of a 16 bit width FIFO. At this point, the data contained in the FIFO can be retrieved with an API call on the host side, specifying the endpoint and the length of the transfer in bytes. A PipeOut is instantiated in the RhythmStim design connected to the Opal Kelly RAM to manage and buffer the recording transfer. A second PipeOut has been added to bypass the RAM buffering and to provide the spikes information with a lower latency. While the first PipeOut continues to stream the buffered data in large chunks, the software runs a secondary thread polling the new PipeOut for new data every millisecond. The FIFO connected to the pipe-out provides the software the count of words that it contains. Whenever the software notices that this count is greater than 0, it reads from the PipeOut all the spikes contained in the FIFO. The words counter is given to the host by the WireOut construct of the Opal Kelly, which thanks to an endpoint exposes FPGA variables of 32 bit via USB through an API. The spikes acquired by the software can be streamed via the UDP protocol to any user-defined IP address. The packet is formed by four integers of 4 bytes in Big-Endian order, which are ordered in an array position from 0 to 3: Zero, timestamp, amplitude, and channel. If the acquisition system saves data on the disk, the detected spikes are also stored in a separate file from the main record. Thanks to the WireIn constructs, used to show variables from the software to the FPGA, the user can control the digital spike detector through the software to run or stop it, to set the threshold multiplier (in 0.5 step), the blind window length (to stop the detection for a few ms after a stimulation command) and the channels whose outputs have to be active. These parameters are exposed to the user with a dedicated application window that can be reached from the main window of the RhythmStim application, which also shows a real-time raster plot of the spiking activity (Figure 3.8).
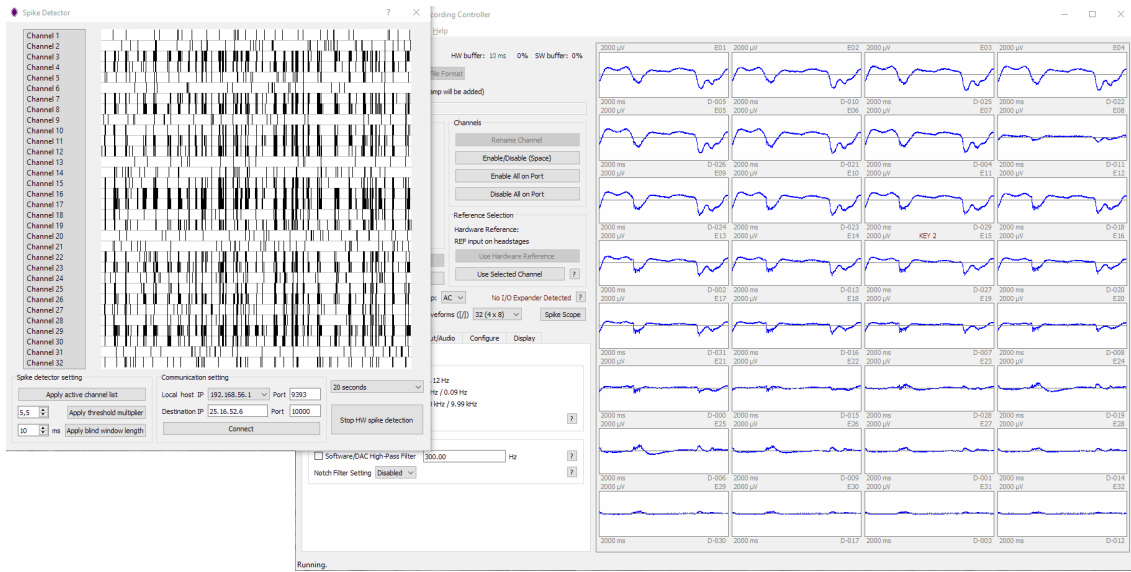
Figure 3.8: Graphical user interface. The window on the left shows the real time raster plot and allows tuning the parameter of the spike detector. The window on the right is the standard application window that shows the raw recording and manages the interface with the recording system.

3.3   SYNCH integration

An implantable array of microelectrodes records and stimulates neural signals via the Intan RHS stimulation/recording controller, developed to integrate the feature required for the purpose. The spiking activity is detected and fed to an array of memristors that process spikes and changes their weight according to synapse-inspired mechanisms such as *spike-timing-dependent plasticity*. A control unit (CU) completes the link between the network of neurons and SNN in this forward path, encoding the weight of each spike to a stimulus suitable for the stimulation of the SNN neurons and routing it to the target artificial neurons. In the backward path, from digital to biological, the AP signals of SNN output neurons are routed by the CU to the memristor array, driving plasticity weights that are then transformed into weighted pulses for ICMS. The SNN, after initialization, will perform autonomously and adaptively control of the network of neurons.

The system integration took place in two steps. A first approach was to remotely connect the components using UDP as a communication protocol to build a prototype of the overall integrated system. Remote testing was performed using both pre-recorded data and synthetic signals to include the Intan RHS controller. The major milestone was to simulate the flow of the information and to ensure that the components were able to elaborate the data in a correct regime. Local integration has been achieved with direct and fast hardware communication between devices.

Electrophysiology setup

The Intan RHS stimulation/recording controller governs a multielectrode array implant that records and stimulates activity in the barrel cortex of a urethane anesthetized rat as described in Section 2.1. It detects the spiking activity and communicates it to the CU, preserving the timing and location of the events for an accurate reconstruction and propagation of information about the neuronal activity. Also, whenever triggered by the CU, the controller applies the ICMS to the tissue, to drive the neuronal activity. The implementation of this system is part of this work and is extensively discussed in Section 3.2. This implementation is developed on the FPGA of the Intan Technologies RHS stimulation/recording controller and synthesized as a digital circuit, to deal with the spiking events in a rate compatible with the biological signalling time.

For an agile testing and debugging of the local connections, I developed a surrogate source of spike capable of replaying prerecorded data. It is developed on a board providing a System-on-Chip that includes an ARM processor and an FPGA. A Linux-based operating system was streaming the prerecorded spikes to the programmable logic of the FPGA, where they are sent from a UART module providing the same communication characteristic as the one that I implemented in the Intan RHS controller.

CONTROL UNIT

The CU acts as a router and manages the different components of the overall system. It routes the spikes and encodes to appropriate stimuli that are applied both to memristors and to SNN neurons. It also biases the SNN, allowing to program and initialize the SNN according to the desired model parameters (e.g., connectivity and synaptic weights, basal excitability of neurons) and includes a machine learning layer to classify the output of the SNN, providing feedback stimuli to the neurons. This is quite intriguing as it takes a role that resembles the one of diffuse neuromodulation systems that control global connectivity and excitation state in the real brain, thereby closing the adaptive stimulation loop. It can embed neuromorphic digital circuitry for emulation of synaptic plasticity. It is developed at the Technische Universität Dresden [126].

A Xilinx Spartan-6 FPGA was used within the CU system to increase the total lines to support the connection to the other devices, even with large parallel communication such as the Address event representation (AER) protocol to and from the SNN. This FPGA also adjusted the input/output voltage of the CU (1.8V) to interface with the Intan RHS controller (3.3 V) and the memristor setups (5 V) using UART set to run at 115200 Baud, using one stop-bit and even parity. A mapper was included in the FPGA design, which allows to conveniently switch between several routing scenarios in order to perform individual experiments either with a source streaming pre-recorded data, the Intan RHS controller and to include or exclude the memristors setup. Here, the incoming data from the other setups is entering into a buffer, whenever it is available at the interfaces. In situations where several interfaces aim to write into the buffer at the same time, a fixed prioritization is applied, and the remaining interfaces are read out as soon as the buffer is available, with an higher priority towards events from the SNN, according to the expected data rates for incoming data from the sources. All incoming data is routed to the CU, where it is processed, and corresponding messages are sent back to the FPGA. The CU is

capable of individually addressing the partner setups by means of a destination ID, which is interpreted by the CU-FPGA and then determines the routing. In this configuration, the CU forms the center of a star-shaped network topology, analogous to the setup prototyped using UDP.

Memristors

The memristors array will serve as synaptic processors for the implementation of neuromorphic synapses. In the electrical-to-biological pathway, *digital* spikes arriving from artificial neurons will be turned into analogue, weighted signals by the memristive synapse-like memory. The memristive setup is realized by ARC Instruments [127] and consists of a board conditioning an array of memristors, commended via a computer. The board provides the electronics required to apply the chosen pulses to the memristors, and to read out the resistive state over time.

Spiking neural network

The SNN is developed as an hardware circuit on chip, meaning that it is an embedded neuromorphic platform that mimics the behavior of a real neuronal network, where neurons are physical circuits and fully interconnected by real *wire* that can assume different weights. The SNN will work as reservoir, providing temporally integrated and nonlinearly expanded signals, but also as a component analyzer to enable the learning of the basic components of the input signal to represent them by independent components. Both of these features will be enabled by an on-line adaptation through synaptic and homeostatic plasticity rules, allowing to study of the co-adaptation of the biological and the artificial networks. The SNN is developed by SynSense (Neuromorphic Processor Dynap-SE2 [128]) and consists of a board that hosts the neuromorphic chips with the networks of neuron, together with asynchronous digital circuits for managing the address-event traffic.

Communication protocols

AER is used in order to ensure communication of spike events among the subsystems. AER describes a family of communication protocols that are used to exchange data with neuromorphic hardware. Due to its asynchronous nature, this protocol is well suited for the transmission spikes from and to the SNN, thus is used to connect directly the CU to the SNN. Being designed for the communication of spikes, it

relies on a four-phase Handshake, to receive and transmit firing activity that gets translated from digital pulses to postsynaptic potentials on the memristor. Whenever a valid datum is applied to the data lines, multiplexed in a bus 20 lines, the sender lowers the Request control line. The receiver correspondingly lowers the acknowledge line (both are active low). After this first phase, the receiver is required to keep the acknowledge line low until the datum is processed, and then releases the line. The transaction is closed as soon as the sender responds to this by releasing the Request as well. Likewise, artificial neurons action potentials are multiplexed and applied to the outgoing parallel data bus of 20 bit (and the two control signals additionally).

A serial transmission of the data based on the universal asynchronous receiver-transmitter (UART) protocol is used to connect the CU, the Intan RHS controller and the memristors setup. The choice of employing this protocol for connecting these devices stems from the limited number of available connections on these controllers. Using UART allowed to reduce the required lines count from 44 for bidirectional AER to only 2 for the serial interface. Data from these setups is processed and produced channel by channel, that means that no events are generated concurrently. This also enables the possibility of direct connection to a computer for logging, via off-the-shelf UART/USB adapters and thus ensures a fast debug and validation of the data transmission. Detected events are communicated in 4 Bytes, with the upper 20 Bit being composed of timestamps, and the lower 10 bit corresponding to the artificial neurons IDs. The CU utilizes this protocol as well, in order to send and receive data from/to the FPGA within the CU system.

4

Results
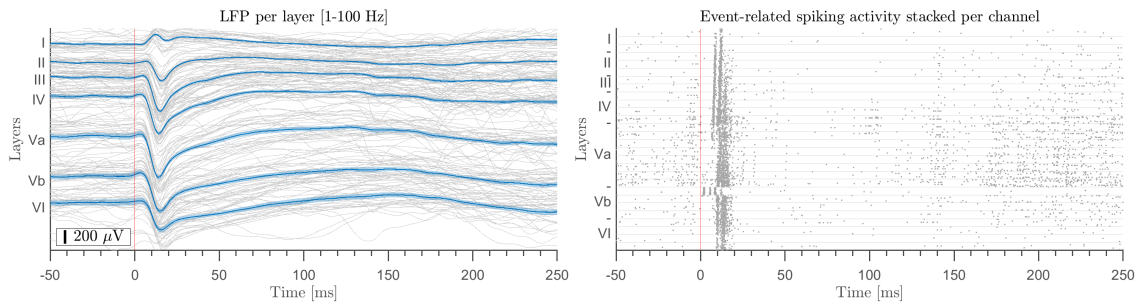
Figure 4.1: Barrel cortex response to mechanical whisker stimulation Left: LFP response to stimuli for each layer of the barrel cortex. In blue, the average LFP; in gray, the LFP of each stimulation trials aligned to the stimuli onset. Signals are the mean of channels recording in the same layers. The red vertical line indicates the time of the stimulation. Right: spikes raster of the event-related activity. In gray, the spikes of the 29 trials are aligned to the stimuli onset and stacked for each channel. The red vertical line indicates the time of the stimulation.

4.1 Mechanical stimulation of the whisker

Studies have shown that neurons within the barrel cortex respond with increased spiking activity when a whisker touches an object [129]. This type of response can be divided into two distinct components: a short-latency response that is thought to originate from direct synaptic input from thalamocortical afferents and involve excitatory postsynaptic potentials (EPSPs) as well as inhibitory postsynaptic potentials (IPSPs) at different depths of layer IV in the barrel cortex; a long-latency response that is thought to be generated by intracolumnar circuits involving both excitatory and inhibitory neurons located deep inside layer IV barrels columns. These cells not only receive input from thalamocortical afferents, but also generate their own local signals through recurrent connections between pyramidal cells and interneurons within each columnar circuit. The result is a prolonged depolarization or burst of firing due to increased EPSP activity followed by IPSP inhibition, resulting in decreased spiking activity after stimulus offset [130].

The stereotypical LFP evoked by the stimulation of the whisker comprises three main waves: response onset, with a latency of approximately 5 ms after the stimulation, the principal peak of the response, approximately after 15 ms, and a slower positive rebound after 20-40 ms [131, 132]. The course of the principal peak wave in time corresponds to the distribution of the shortest latencies of the responses of a single unit of pyramidal cells [101, 133]. This is supported by our experimental data and shown in the example of Figure 4.1; the experimental protocol and the equipment are described previously in 2.

66

4.2 Intracortical microstimulation

By applying ICMS to the barrel cortex of the anesthetized rats, a remarkably different response can be observed than that evoked by mechanical stimulation of the whisker. Two example trials showing the response are reported in Figure 4.2. The evoked response consists of a first period of inhibition of the activity, followed by a spindle-like activation that lasts up to more than a second and spreads from the IV layer to layer II and VI. Figures 4.3 and 4.4 show, respectively, the average LFP and the spiking activity during the spindle-like response to the stimuli of an experiment in which ICMS were given with an amplitude of 10 μA every 7 seconds in the upper part of the layer Va. The response starts with a spiking activity inhibition corresponding to an LFP down-states of 120 ms, followed by a spindle-like oscillatory activity at a frequency of 9.8 Hz. The density of the spikes during the spindle peaks sensibly increases and decreases up to 7 times, synchronously with peaked up-states in the LFP. Previous works [134, 13, 135] showed stimulation in the neocortex of rats and mice under different anesthetics and in awake rodents to produce the same initial inhibition of spiking activity, but did not highlight any subsequent spindle.

More generally, the experimental results from 29 rats and many sets of stimulation at different amplitudes and depth show a median inhibition of activity after the stimuli of 124 ms and a following spindle with a median frequency of 11 Hz, as shown in Figure 4.5a. Figure 4.5b shows the the median absolute deviation (MAD) distribution of the spindle frequency and the inhibition duration, between different sets on the same animal. Spindles can last up to more than a second, with a minimum of 3-4 peaks, up to a dozen. During the spindle, activity is strongly correlated across layers from VI to II/III (bottom right of Figure 4.3 and Figure4.4 for LFP and firing rate, respectively). Spindles originate from the central layers (IV and the upper end of Va) and propagate up to layers II and down to layers VI during mid-oscillations, before terminating at the same depth. Some rats show a slight shift in the depth of the spindle origin, and some have a second source in the lower part of the layer Va. In the latter case, there are two distinct depths from where the spindles originate simultaneously, before merging in the mid-oscillations and terminating again at the same depths.
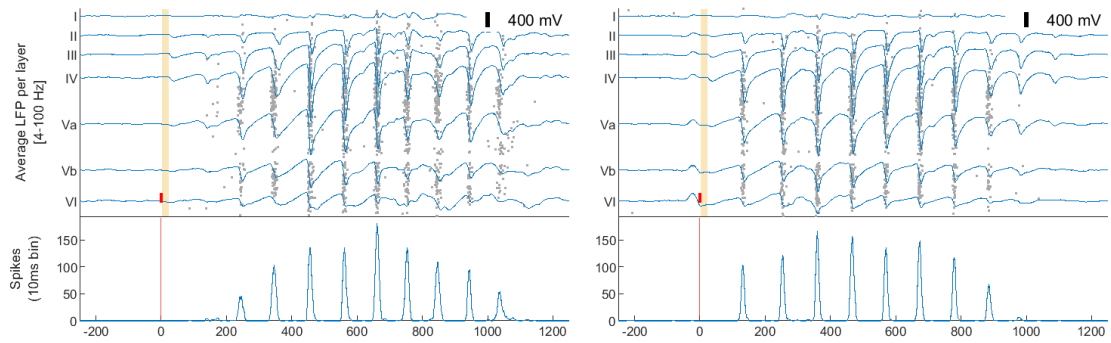
Figure 4.2: Spindle responses evoked by ICMS. Top: Combined view of event-related LFP and spiking activity of 2 ICMS example trials. In blue, the average LFP of channel in the same layer; in gray, the spikes for each channel. The red vertical bar indicates the depth and the time of the stimulation, the orange area delimits the artifact interpolation. Bottom: firing rate in spikes/s in a 10 ms moving window. The red vertical line indicates the stimulation time.

ICMS SHAPES

Changes in stimulation amplitude or depth do not show a significant variation in the average response shape ($P>0.05$, Kruskal-Wallis test, distribution of activity inhibition and spindle frequency shown in Figure 4.6a) or in response strength (spikes count and LFP amplitude). Increasing the ICMS amplitude shows a linear relation with the probability of evoking a spindle with a gain of 16.2% ($\pm$ 1.24 %) every 5 μA of ICMS amplitude (Figure 4.6b). A stimulus amplitude lower than 5 μA did not show any response in the vast majority of the anesthetized rats. The stronger the current, the more the propagation of a voltage level that leads to a depolarization of the tissue that causes the activation of farther and overall more neuron somata and fibers. This may imply a local population dynamic where a minimal level of excitation spread is required to generate a spindle. Different thresholds in different animals could be related to the types and the amount of excitable tissue nearby the stimulating electrode. Furthermore, stimulation of amplitudes greater than 15 μA shows a significant reduction in activity inhibition variability between trials in the same animal ($P<0.01$, Mann-Whitney U-test, Figure 4.6c). The stimulation indicated as *max* indicates an amplitude at the maximum stimulation limit of the system of 7 V, corresponding to about 25 μA, depending on the animal. Changes in the layer where stimulation is applied show no significant differences in the number of evoked responses with the same amplitude when stimulating between layers IV, V and VI, while stimulation in the supragranular layers, II and III, shows to be less effective (about 30% less probability). This is probably due to the stimulation being more
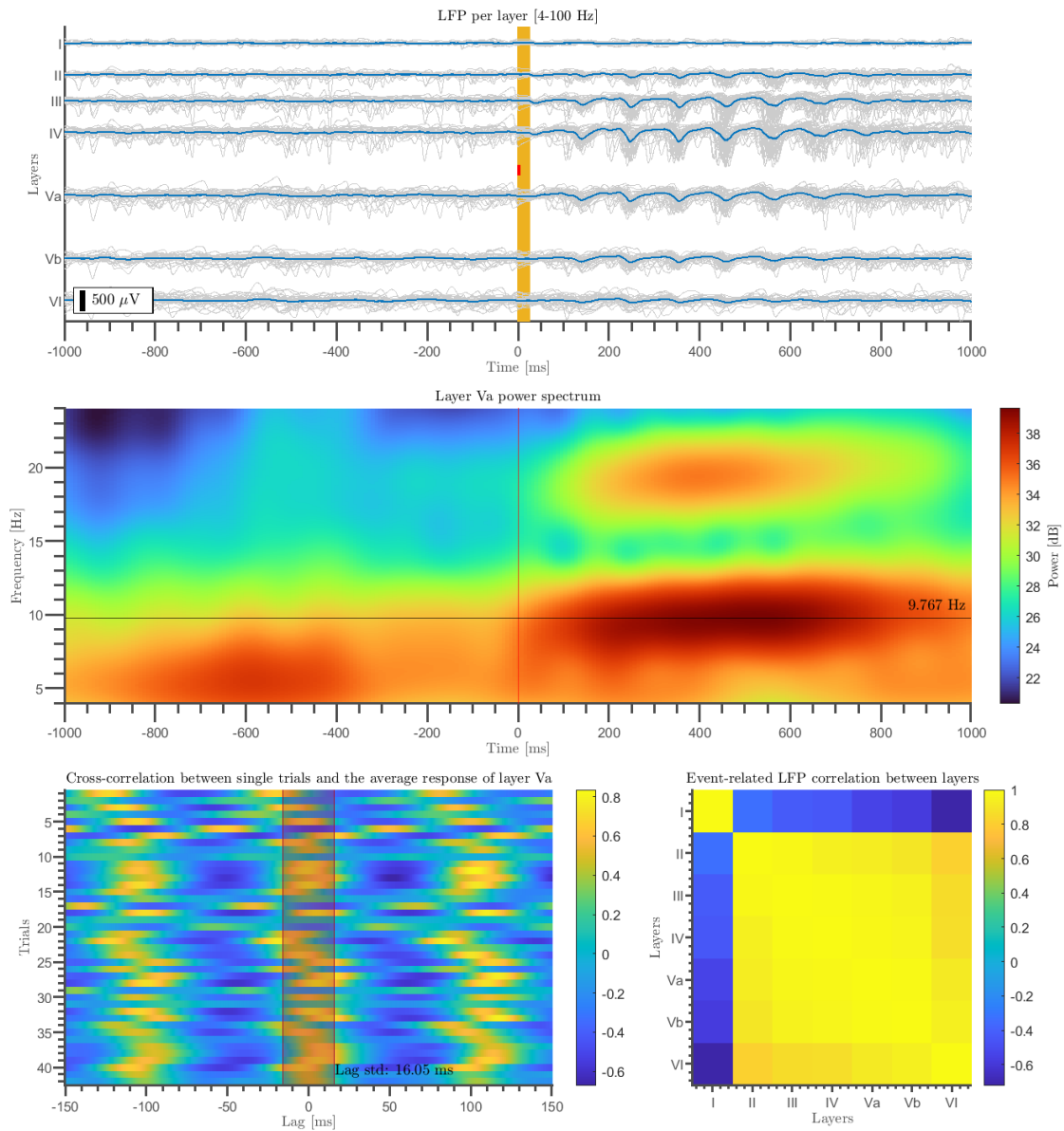
Figure 4.3: Event-related LFP activity evoked by ICMS in the barrel cortex. Top: average LFP for 42 ICMS applied to layer Va. In blue, the average LFP; in gray, the LFP of each stimulation trials. Signals are the mean of channels recording in the same layers and trials are aligned to the stimuli onset. The red vertical bar indicates the depth and the time of the stimulation, the orange area delimits the artifact interpolation. Middle: average of the power spectrums of the LFP activity in layer Va of the 42 stimulation trials. The red vertical bar indicates the stimulation onset, the horizontal black line highlights the response frequency of 9.8 Hz. Bottom left: cross-correlation between the single trials LFP responses in layer Va and their mean. The lags between trials show a standard deviation of 14.3 ms, highlighted by the overlay rectangle. Only trials showing a maximum cross-correlation higher than 0.3 are considered. Bottom right: post-stimuli correlation between LFP average responses of each layer. The oscillatory activity, despite the different amplitudes, is strongly correlated across all the layers, except for the layer I.
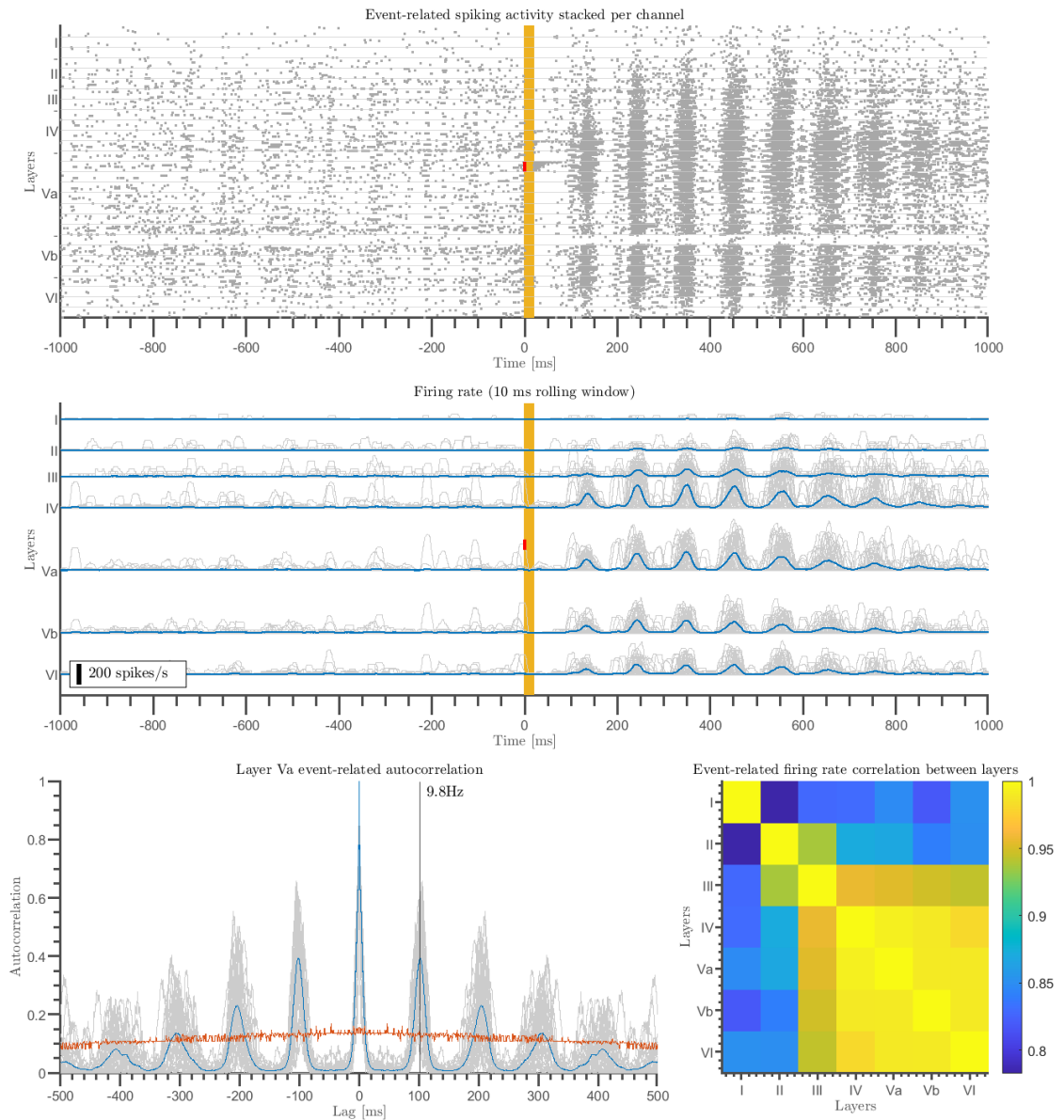
Figure 4.4: Event-related spiking activity evoked by ICMS in the barrel cortex. Top: spiking activity per channel of 42 ICMS in layer Va. In gray, the spikes of the 42 trials are aligned to the stimuli onset and stacked for each channel. The red vertical bar indicates the depth and the time of the stimulation, the orange area delimits the blanking windows where events cannot be detected due to the stimulation artifact. Middle: firing rate response to stimuli of each layer, accumulated in a 10 ms moving window. In blue, the average firing rate over trials; in gray, the firing rate of each stimulation trial. Firing rate of channels in the same layers are averaged and trials are aligned to the stimuli onset. Red vertical bar and orange area as before. Bottom left: In blue, average autocorrelation of the spiking activity of layer Va in bin of 1 ms; in gray, the autocorrelation of each stimulation trial. The red line shows the autocorrelation found by permutation test (P=0.95), while the black vertical line marks the peaks at 102 ms of lag, indicating an oscillatory frequency of 9.8 Hz. Bottom right: post-stimuli correlation between average firing rates of each layer. The oscillatory activity, despite the different amplitude, is strongly correlated across all the layers.

(a)   **(b)**
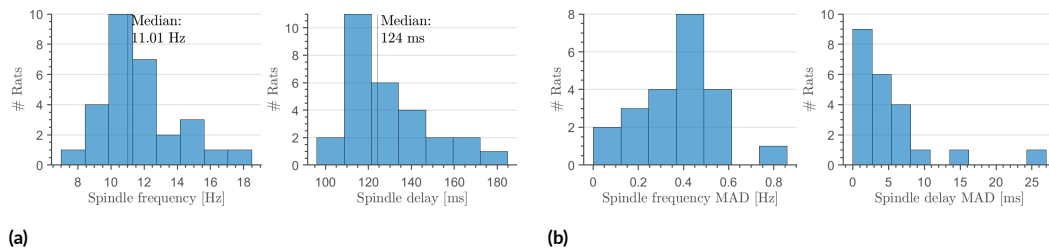
Figure 4.5: Distribution of spindles frequency and activity inhibition induced by ICMS. (a) Distributions of spindle frequency (left) and activity inhibition (right) evoked in different rats; for each rat showing a valid response in more than one stimulation set, the median value has been considered. (b) MAD of spindle frequency and activity inhibition between sets of same rats.

(a)   **(b)**   **(c)**
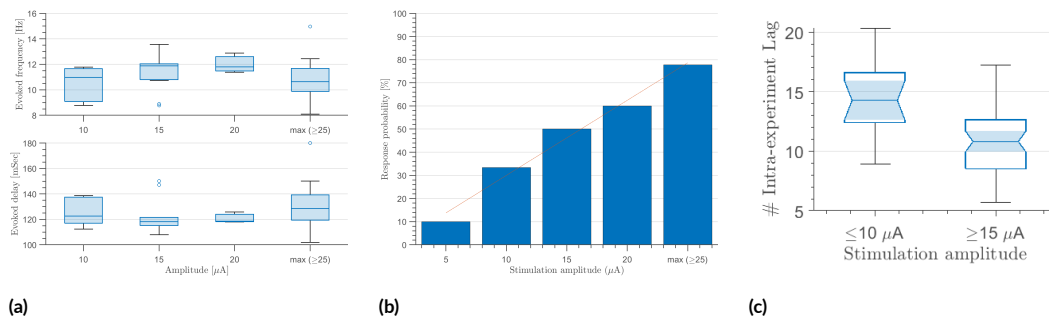
Figure 4.6: Effect of amplitude and depth on the spindles evoked by the ICMS. (a) Distribution of the spindle frequency (top) and the activity inhibition (bottom) for stimulation applied at different amplitude in layer VI. Kruskal-Wallis test results in a non-significant difference ($P>0.05$) between groups of stimulation amplitudes. Stimulation applied to layers IV and V shown similar results. (b) Percentage of rats where spindle responses has been evoked for different stimulation amplitudes. There is a significant relationship ($P<0.001$) between stimulation amplitude and the probability of a spindle to be evoked. (c) Distributions of the per-trial variability of the evoked activity inhibition for stimulation amplitude lower than 10 μA and greater than 15 μA.

effective in activating the most excitable elements in the cortex, the large fibers of pyramidal cells [104]. Stimulating fibers leads to a major spread of stimulation that targets excitatory neurons on layers IV and Vb, which receive synaptic input from the VPM. Figure 4.7 describes the spindles in terms of firing rate, with different stimulation amplitudes and depth: in the top part the firing rate sum of the stimulation trials is shown per channel, in the middle part the sum of the firing rate in the whole barrel is shown per trial, in the bottom part the autocorrelation of the overall spiking activity is averaged between trials, highlighting the average spindling frequency.

Age, weight, sex and temperature effect

Age (range P25-P35) and weight (range 80-160 g) of the animals do not seem to influence the response probability significantly (correlation t-test, $P>0.05$), as well as the body temperature recorded simulta-
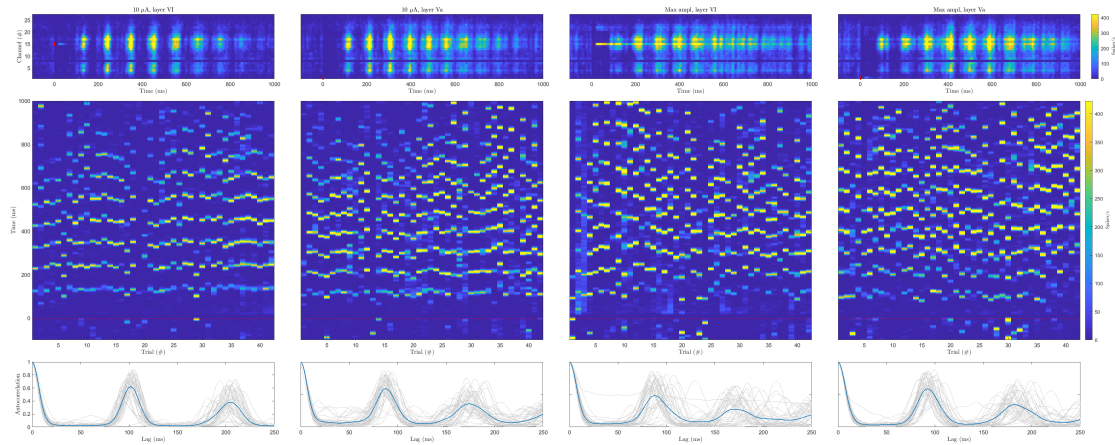
Figure 4.7: Spindle activity evoked by the ICMS per trial. Four example sets from the same subject. From left to right, stimulation of 10 μA at layer Va, 10 μA at layer VI, maximum amplitude at layer Va, and maximum amplitude at layer VI. Top: firing rate in a 10 ms moving window of the average evoked response per channel. Middle: sum of the firing rate of all the channels in a 10 ms moving window ordered per trials. The red line indicates the ICMS. Bottom: mean of the autocorrelations of the post-stimuli evoked activity of trials, in blue, and autocorrelation of the single trials, in gray. The spindle is preceded by the same average duration of activity inhibition across sets, also the average spindle frequency remain similar.

neously with the barrel cortex activity. Neither gender significantly affects the probability of evoking the response (t-test, $P > 0.05$).

4.3 Spindles in spontaneous & mechanically evoked activity

During the experiments, spindles have also been observed in response to mechanical stimulation of the rat whisker and in spontaneous activity, without perturbing the state of the anesthetized animal with any stimulation. In both cases, the spindles show frequencies and durations similar to those evoked by ICMS. Spindles in spontaneous activity can be found in about half of the rats (28/55) and are not preceded by any inhibition of activity (Figure 4.8). Spindles in response evoked by whisker stimulation occur in a fewer rats (5/20) approximately 400 ms after the onset of the stimulus. The spindle is preceded by the expected stereotyped response at the mechanical stimulation of the whisker, as in Figure 4.9. An example experiment is shown in Figure 4.10 in LFP and in Figure 4.11 in spiking activity. On the left of both figures, the activity has been averaged to the whisker stimulation onset: given the intra-trial variability, the average response is not clear, while it is clear in single trials. On the right side of both figures, trials have been aligned to the response: the average evoked spindle is highlighted, as well as the lag introduced to align the trials. The delay from the stimuli to the spindle, in addition to being longer, also has greater variability between trials in the same subject compared to ICMS, as visible in the example of Figure 4.12.
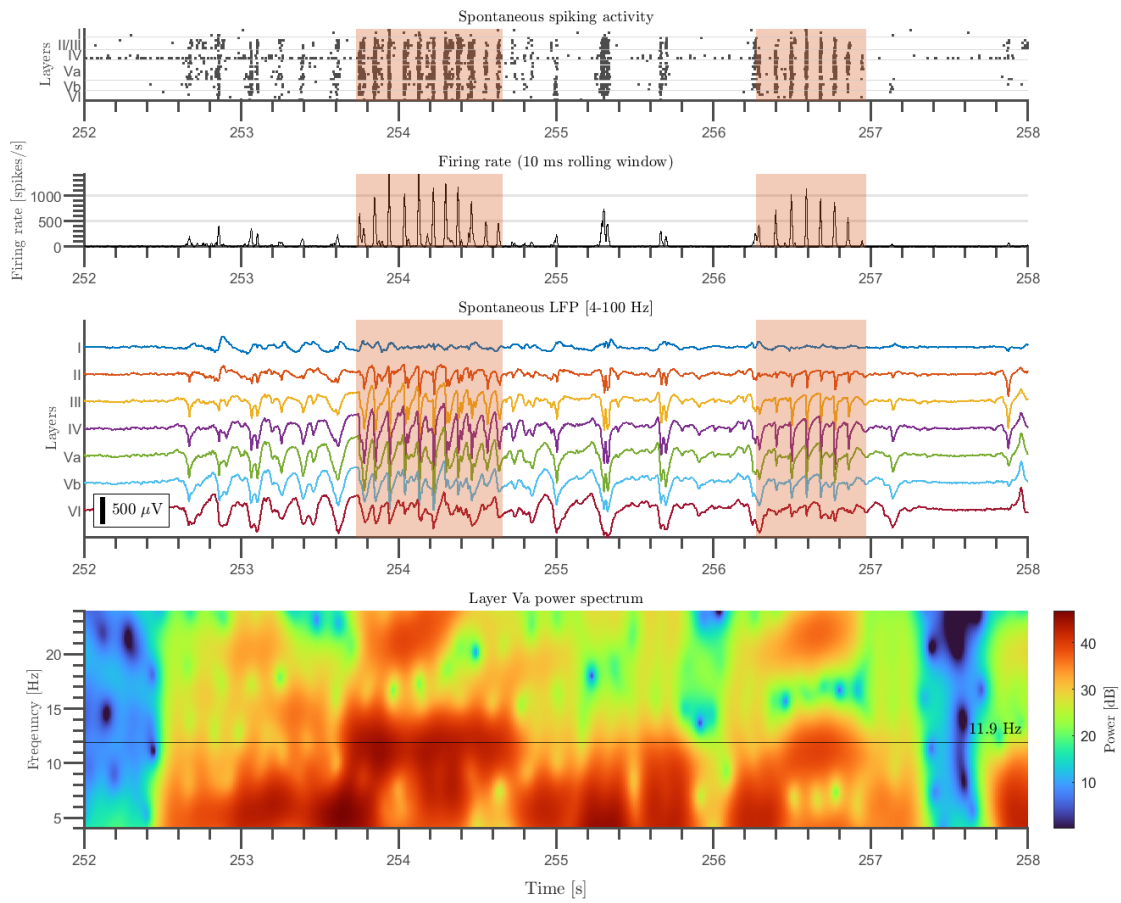
Figure 4.8: Spindles observed during spontaneous activity. Top: rasterplot of the spiking activity and global firing rate. Middle: LFP activity, channels of the same layers are averaged. Bottom: power spectrum of layer Va, average of 8 channels. Spindles of 11.9 Hz are highlighted with a red overlay from time 253.74 to 254.65 and from 256.28 to 256.96 ms in both the spiking activity and the LFP, while the rat was not undergoing any stimulation.
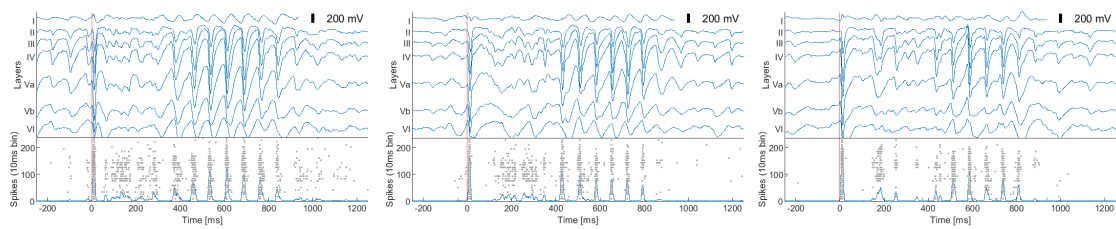
Figure 4.9: Spindles evoked by whisker mechanical stimulation. Top: event-related LFP averaged from channel in the same layers of 3 ICMS example trials. Bottom: spikes and firing rate in spikes/s in a 10 ms moving window. The red vertical line indicates the time of the stimulation. The spindles start with a notably different delay about 400 ms after the stimuli.

74
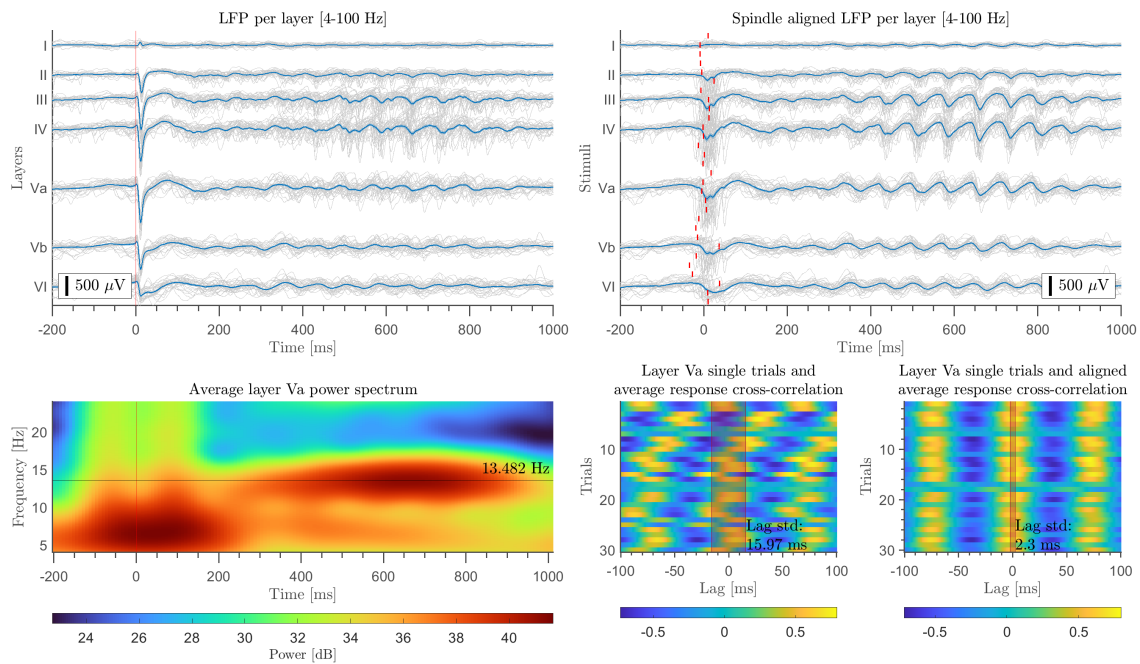
Figure 4.10: LFP response evoked by whisker mechanical stimulation. LFP of 29 mechanical stimulation of the whisker. About 15 ms from the stimulation onset, the stereotyped response. Signals are the mean of channels recording in the same layers. Top left: LFP response in each layer the barrel cortex aligned to the whisker stimulation onset. In blue, the average LFP of each layer; in gray, the LFP of each stimulation trials. The stereotyped response evoked by the mechanical whisker stimulation consisting in a strong deflection of the LFP can be observed 15 ms after the stimuli, followed by a slower positive rebound. The red vertical line indicates the stimulation time. Top right: LFP response of each layer of the barrel cortex aligned to the spindle response. In blue, the average LFP of each layer; in gray, the LFP of each stimulation trials. The red vertical line indicates the stimulation time. Bottom left: average of the power spectrums of the LFP activity in layer Va. The red vertical bar indicates the stimulation onset, the horizontal black line highlights The response frequency of 9.8 Hz. Bottom right: cross-correlations of the stimulation trials of LFPs before and after the alignment, underlying the delay variability. The second graph shows the little variability in the spindle frequency between trials after the alignment.
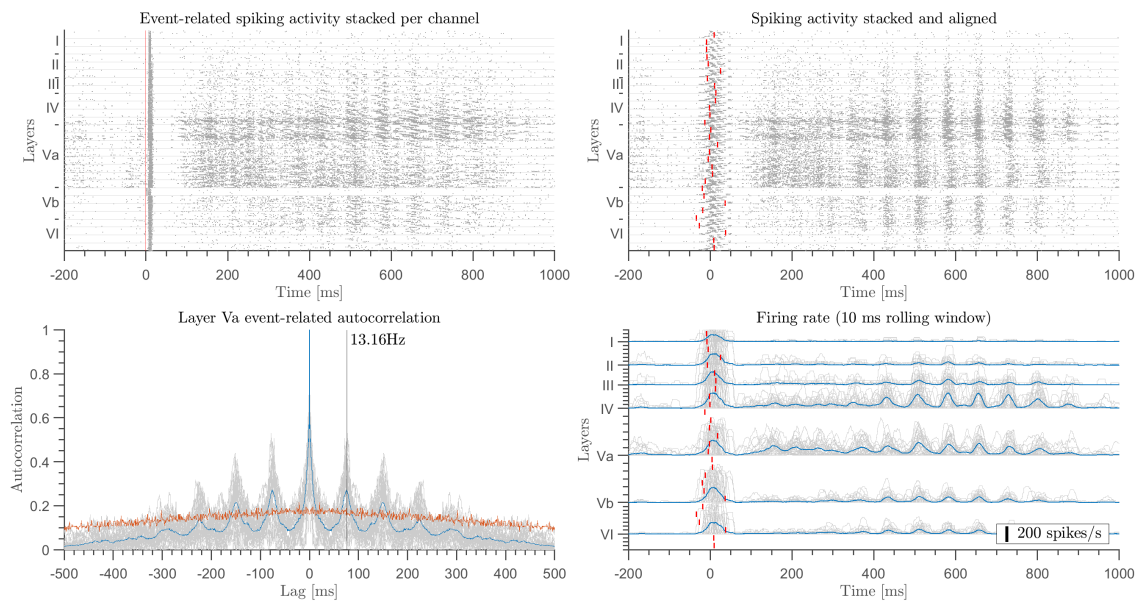
Figure 4.11: Spiking activity evoked by the whisker mechanical stimulation. Spiking activity and average firing rate of 29 mechanical stimulation of the whisker. About 15 ms from the stimulation onset, the stereotyped response. Top left: rasterplot of the spiking activity stacked by trial for each channel, aligned to the stimulus onset. The stereotyped response evoked by the mechanical whisker stimulation consisting in a peaked increase in the firing rate can be observed 15 ms after the stimuli. The red vertical line indicates the stimulation time. Top right: rasterplot of the spiking activity stacked by trial for each channel, aligned to the elicited spindle activity, to emphasize the oscillatory response. Red bars indicate the stimulation time of the trials. Bottom left: autocorrelation of the post-stimuli spiking activity of layer Va. In gray, the autocorrelation of the single trials, in blue their average. In red, the autocorrelation found by permutation test (P=0.95). Bottom right: firing rate response to the whisker stimuli of each layer, smoothed by a 10 ms moving window. In blue, the average firing rate of each layer; in gray, the firing rate of each stimulation trials. Signals are the mean of channels recording in the same layers. Red bars indicate the stimulation time of the trials.
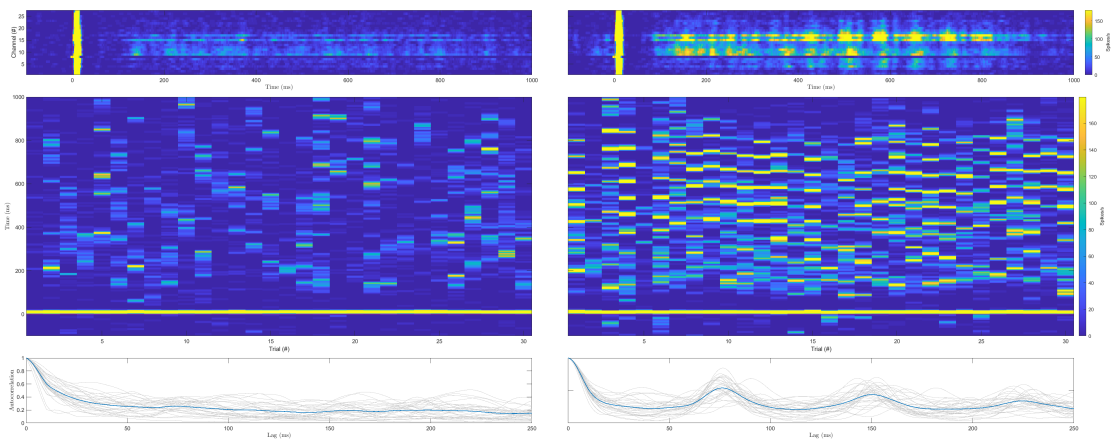
Figure 4.12: Spiking activity evoked by the whisker mechanical stimulation per trial. Two example sets from the same subject. On the left, the set does not show any spindle evoked by the whisker stimulation, on the right, many set show a spindle response. The spindle is preceded by non-coherent activity between trials and starts about 400 ms after the stimuli, with great variability between trials. The average spindle frequency remain similar. Top: firing rate in a 10 ms moving window of the average evoked response per channel. Middle: sum of the firing rate of all the channels in a 10 ms moving window ordered per trials. Bottom: mean of the autocorrelations of the post-stimuli evoked activity of trials, in blue, and autocorrelation of the single trials, in gray.
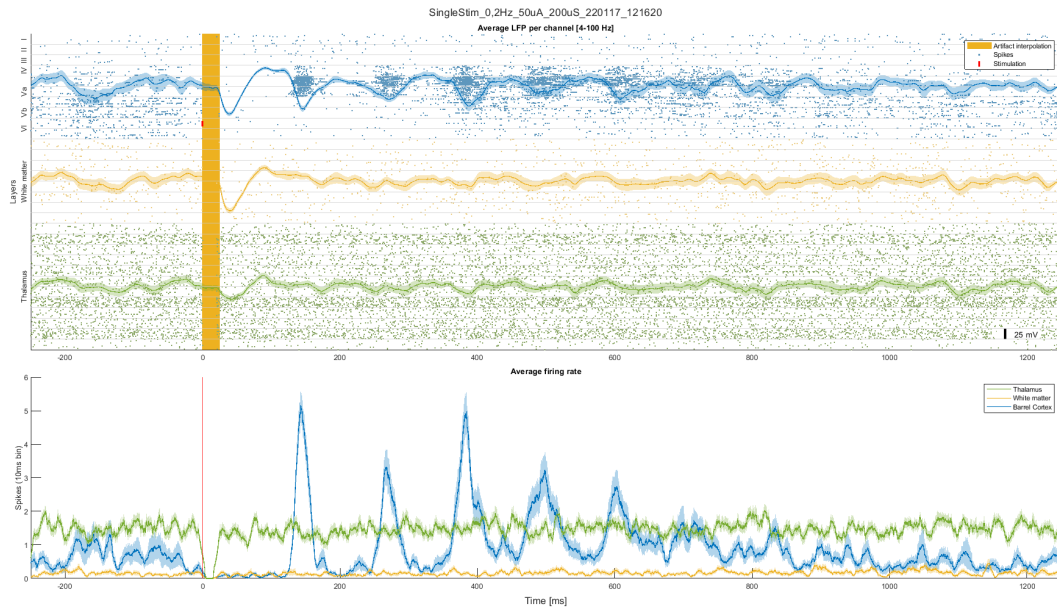
Figure 4.13: Spiking activity evoked by ICMS in the barrel cortex and VPM. Top: combined view of the event-related LFP and MUA events of 60 trials. Lines indicates LFP mean and standard error of the mean, dots indicates spikes stacked per trial for each channel. The red vertical bar indicates the depth and the time of the ICMS pulse, while the orange area delimits the artifact interpolation. Bottom: mean and standard error of the mean of the spikes sum per area smoothed by a 10 ms moving window. Red vertical line indicates the time of the ICMS pulse. Brain areas are grouped by color: barrel cortex in blue, white matter between barrel a thalamus in yellow, and VPM in green.

4.4 CORTICOTHALAMIC ACTIVITY

Spindles normally arise from interactions between neurons located within specific regions of the brain such as the thalamus and cortical layers IV-VI [63, 64]. From the experiments carried out recording from the barrel cortex and the VPM simultaneously (see 2.3) I did not find any correlation between the ongoing activity of the VPM during the spindle in the barrel cortex, neither at the spiking nor at the LFP level; an example is shown in Figure 4.13. Mechanical stimulation of the whisker, however, showed a correlation at the level of LFP activity of the classical response as in Figure 4.14, suggesting correct placement of the probe at the recording site, a conclusion further enforced by histological examination of the probe stain. Furthermore, also spontaneous spindles and spindles eventually after a whisker stimulation do not show any correlated oscillations in the VPM recorded area in LFP or spiking activity.
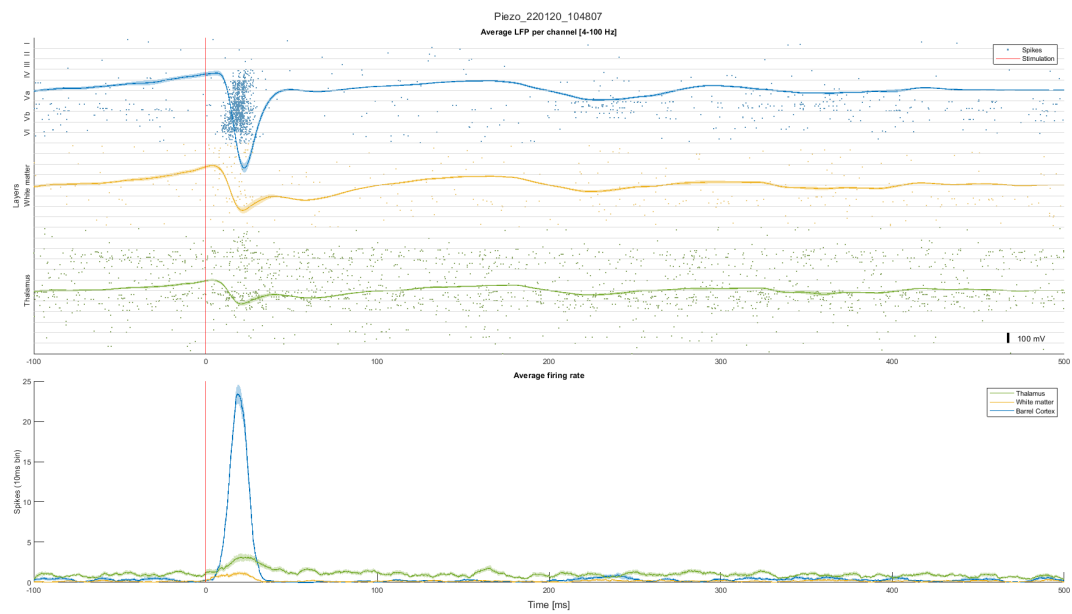
Figure 4.14: Spiking activity evoked by the whisker mechanical stimulation in barrel cortex and VPM. Top: combined view of the event-related LFP and MUA events of 30 trials. Lines indicates LFP mean and standard error of the mean, dots indicates spikes stacked per trial for each channel. Bottom: mean and standard error of the mean of the spikes sum per area smoothed by a 10 ms moving window. Brain areas are grouped by color: barrel cortex in blue, white matter between barrel a thalamus in yellow, and VPM in green. The red vertical lines indicates and the time of the whisker stimulation.

4.5 SPINDLES MODULATION

After the spindles characterization, I tried to modify the activity to *write* in the barrel cortex different information via a set of stimuli. By applying ICMS trains in a range of frequencies close to the spindles one, the activity can be phase locked to the stimulation frequency. Spindles can be modulated in a range between 5 and 20 Hz, phase locking them to the stimulation frequency. A single spindle modulation example is shown in Figure 4.15, while the average results of example experiments phase locked to all the frequencies can be observed in Figure 4.16. A *critical* frequency can be recognized, corresponding to the natural spindle frequency of each rat. With a stimulation frequency lower than the critical frequency, the oscillation is strong in amplitude and the activations occur in the second half of the stimulation period (Figure 4.16a to d), far from each stimulation onset of the train; with a stimulation frequency greater than the critical frequency, the oscillation is weaker in amplitude and the activation occurs in the first half of the stimulation period, close to each onset of the train (Figure 4.16e to g). In other words, the spindle changes gradually the phase respect to the ICMS from being greater than π to smaller than π while increasing the ICMS frequency. Unfortunately, because of the stimulation artifact, the LFP signal is corrupted for the greater part of each stimulation period of the trains. This prevents the use of LFP to draw conclusions about the behavior of neural activity during trains. The spiking activity signal, instead, returns to the normal regime after 10 to 15 ms, resulting in a clean signal without distortion immediately after the blanking window, leaving enough valid time between stimulations to investigate the activity.

4.5.1 ARNOLD'S TONGUES

Periodic pulse stimulations of the barrel leads to a frequency locking of the spindles: this can be seen as a hint that the neuronal population –during a spindle– can be considered as a macroscopic self-sustained oscillation. To investigate this theory, I evaluated the strength of the frequency locking between the spindle and the ICMS train, quantified as the small difference being created. This highlighted a zone where independently of the stimulation amplitude, this difference was around the 0 Hz. But, of greater significance, this highlighted also that when the ICMS frequency was pushed farther than the natural spindle frequency, this difference became greater. Also, when varying the stimulation amplitude, this difference
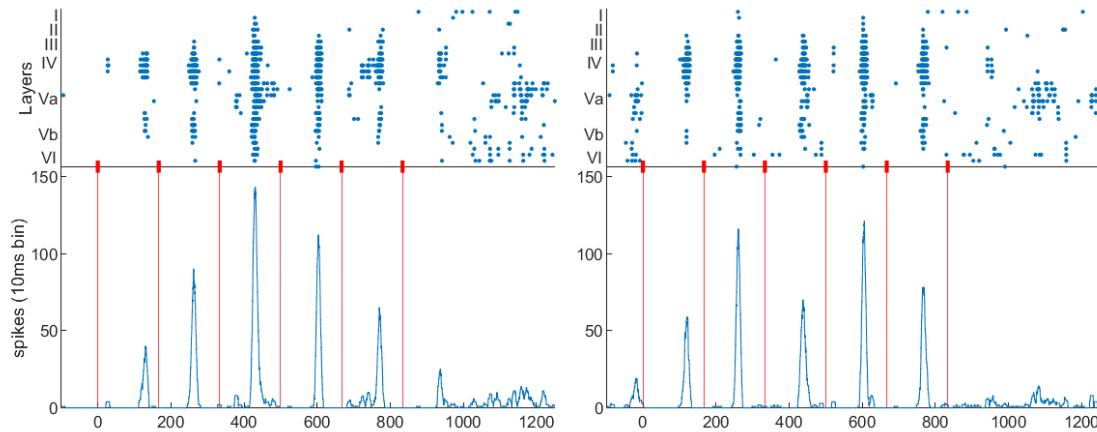
Figure 4.15: Spiking activity evoked by ICMS train at 6 Hz. Top: event-related spiking activity of 2 ICMS example trials. Dots mark the spikes of each channel. The red vertical bar indicates the depth and the time of the stimulations. Bottom: firing rate in spikes/s in a 10 ms moving window. The red vertical line indicates the stimulation time.

was greater when a small ICMS amplitude was applied and smaller when an higher amplitude was applied. The quantification of this spindle frequency trend while varying the superimposed stimulations frequency and amplitude clearly shown a plateau in the surroundings of the spindle natural frequency that was wider with the higher stimulation amplitude. The frequency locking condition, where external stimulation ω is equal to the frequency of the oscillator Ω, is important and applies over a range of amplitudes (I) and frequencies (ω) of the forcing. This domain, where the frequencies are locked, is known as the Arnold's tongue. The overall frequency difference found while varying frequency and amplitude of ICMS is shown in Figures 4.17 and 4.18. The *wider, flat triangle* enclosed by the plateau that are generated when the stimulation amplitude is increased, draw indeed an Arnold's tongue.

Generally, frequency locking implies a rational relationship between the two frequencies, such as $\Omega : \omega = n : m$, where n and m are integers. For noisy oscillators, the locking condition is not always exactly fulfilled, but the locking domains can still be observed in real-world oscillators, at least for the main locking region $n = 1$, $m = 1$. The ability to synchronize or entrain with an external drive is a general property of endogenous oscillators and applies to macroscopic oscillations of ensembles, such as groups of interacting neurons [136, 137]. Therefore, if the reductionist approach outlined earlier is valid, brain rhythms should exhibit frequency locking to external forces. This is what is here observed for the sustained rhythmic activity of spindles in the barrel cortex and these measurements provide evidence of an Arnold's tongue. This result is important, e.g., for understanding mechanisms of possible control

Event-related spiking activity stacked per channel — Layer Va event-related autocorrelation

(a)

(b)

(c)

(d)

(e)

(f)

(g)
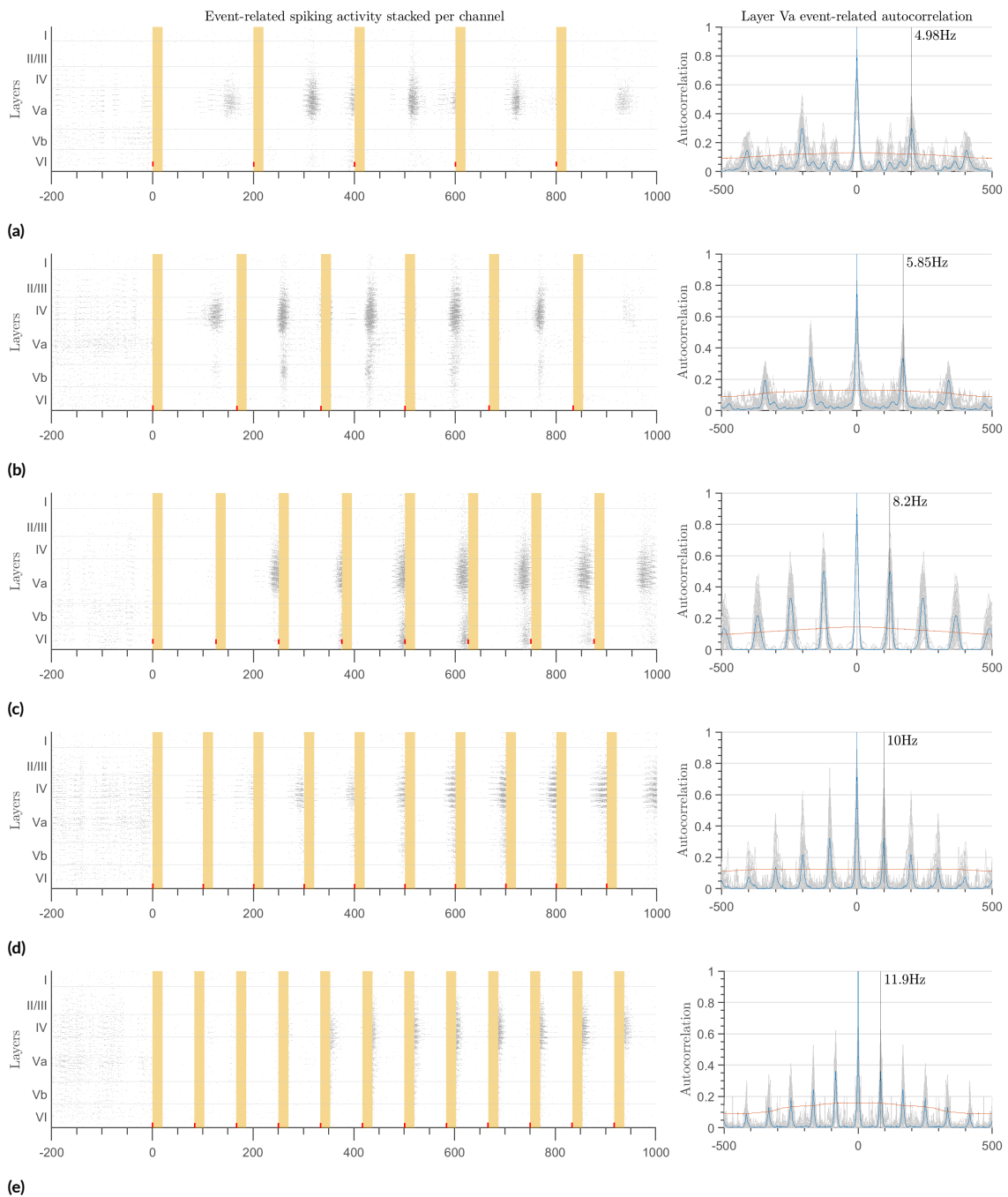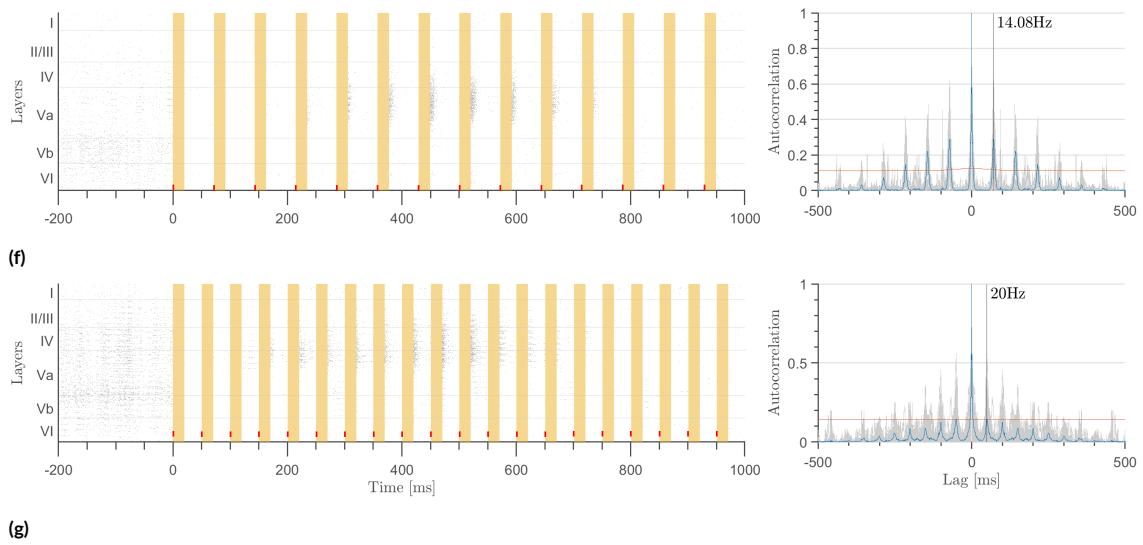
Figure 4.16: Spiking activity evoked by 30 trains of stimuli of frequency from 5 to 20 Hz. On the left, the spikes raster of the event-related activity. In gray, the spikes of the 30 trials are aligned to the stimuli onset and stacked for each channel. The red vertical bar indicates the depth and the time of the stimulation, the orange area delimits the blanking windows where events cannot be detected due to the stimulation artifact. On the right, the autocorrelation of the post-stimuli spiking activity of layer Va. In gray, the autocorrelation of the single trials, in blue their average. In red, the autocorrelation found by permutation test (P=0.95). The black vertical line indicates the peak of the autocorrelation lag, that indicates the oscillation frequency. From top to bottom: 5, 6, 8, 10, 12, 14, and 20 Hz. Spindles are phase-locked to the stimulation frequency.

of pathological brain activity [138, 139].
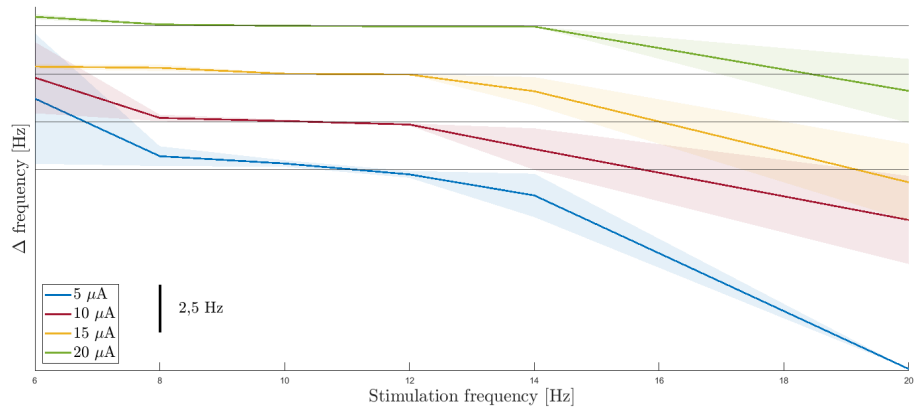
Figure 4.17: Frequency locking of the spindle evoked activity with increasing stimulation amplitude.
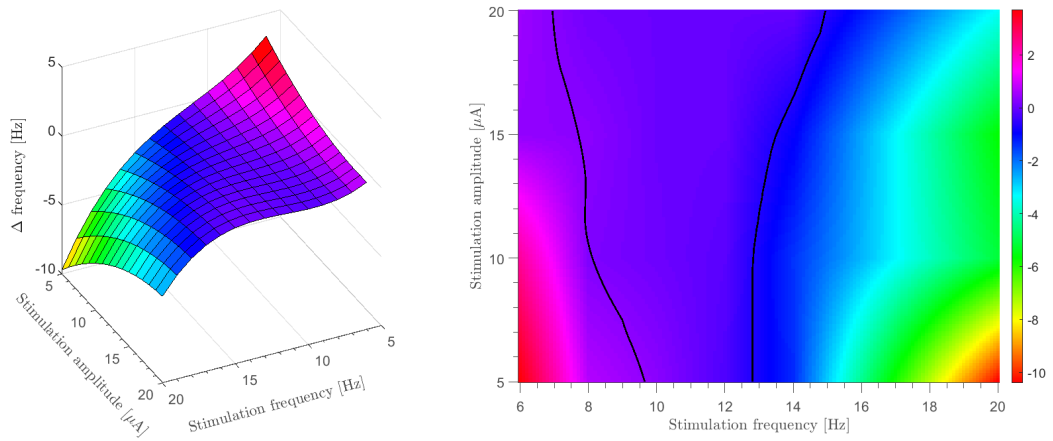
Figure 4.18: Pictorial illustration of Arnold's tongue. Left: 3D representation, with surface interpolation and color-coded by the difference between the frequency of the evoked spindle and the stimulation frequency. Right: color gradient representation of the Arnold tongue, with interpolation. The phase locking area is delimited by the black lines (stimulation frequency - 0.3 to stimulation frequency + 0.7 Hz)
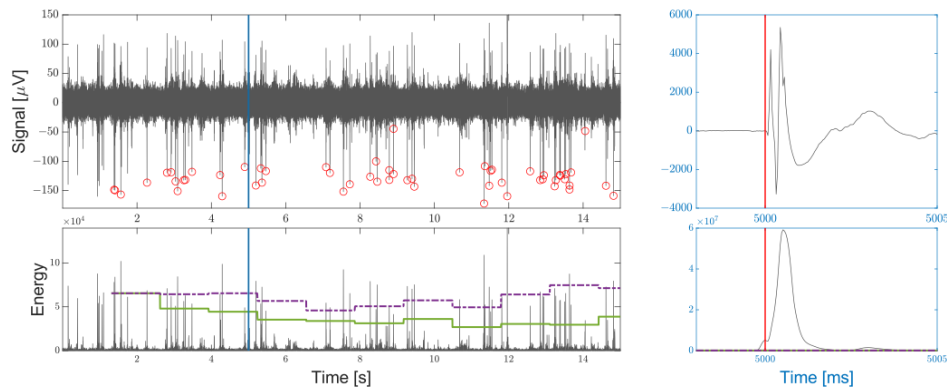
Figure 4.19: Spike detection of a single unit Action Potential (AP) activity on 15 s of acquisition. The vertical blue line corresponds to a cathodic to anodic ICMS of maximum amplitude of 200 μs per phase injected by a channel 520 μm distant. Top: Spikes generated by a neuron nearby the recording electrode surface are clearly visible. Positions and amplitudes corresponding to events detected are circled in orange. The ICMS artifact, recorded as a fast oscillation ranging from −3.5 to 5.5 mV, is magnified in the blue box on the right, where the vertical red bar indicates the stimulation instant. Bottom: The energy output from the SNEO (in gray), is compared with the dynamic threshold in solid green to detect the spikes. In comparison, the threshold altered by the firing-rate based on the whole signal RMS computed in the same timeframes is shown as the dashed purple line. The ICMS energy answer is magnified in the blue box on the right and is several orders of magnitude bigger than the values observed in the graph ($\sim 10^7$). Despite this, the threshold estimation is not altered, and the stimulation artifact does not cause false events detection.

4.6 ELECTROPHYSIOLOGY EXTENDED SETUP TESTING & RESULTS

The spike detector has been tested in simulations and in experiments conducted in the barrel cortex of anesthetized rats as described in the 2 Section. The experimental protocol ICMSs at the meximal μA amplitude. Figure 4.19 shows the detection performance on 15 s around one of the given ICMS of a channel recording a strong spiking signal. The threshold multiplier is set to a value of 18 to focus on the detection of the single unit AP. Note that the first spikes are lost due to the threshold initialization. The threshold fluctuation depends on the MUAs energy around the APs, which being undetected (as expected), influences the RMS level. Anyway, the fluctuation is small compared to the energy developed by the spikes and the threshold remains closer to what would be the noise-based value, allowing for higher accuracy than can be achieved with the classic RMS-based threshold. The accuracy achieved on the entire acquisition of 5 minutes is 92%, with 1369 spikes detected out of 1429 and 58 false negatives. The accuracy, once again, has been defined as the relationship between the correct detection and the sum of the total spikes and the false positives.

The offline analysis performed on our experiments showed that clear APs were found in a reduced

85
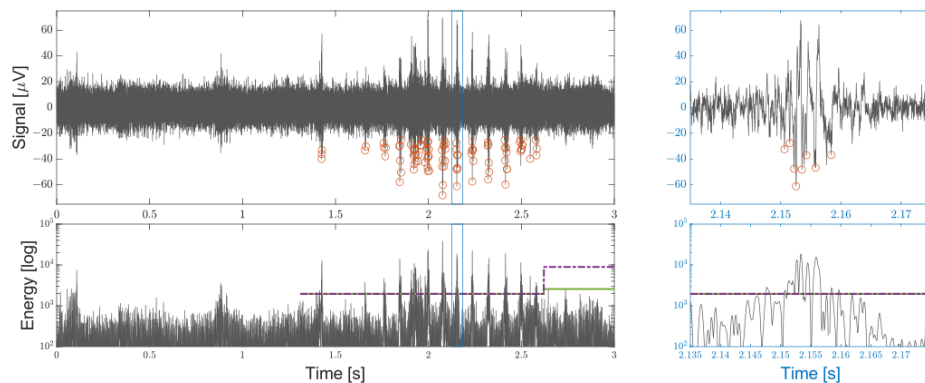
Figure 4.20: Multi Unit Activities (MUAs) on 3 s of acquisition. Top: Activity recorded by an electrode without any clear source of APs near the surface. The MUAs oscillations detected are circled in red and provide a firing profile of the neuronal population. On the right, the detection of the highlighted single MUA is magnified. Bottom: The energy output from the SNEO operator (in gray, reported in a logarithmic scale), is compared with the dynamic threshold in solid black to detect the oscillations. The threshold based on the RMS of the entire signal is reported with the dashed line for comparison. On the right, the energy response of the highlighted MUA is shown.

subset of channels. Given the low number of channels and the different morphology of the covered layers of the barrel cortex, the probability of having multiple neurons close to the electrode surface is low, resulting in only one or two channels acquiring strong APs. In the six experiments, spikes with a strong negative peak below 70μV were not present in any channel in two experiments, in two channels in three experiments, and only on a single channel in one experiment. This is the reason behind the need for an accurate MUA detection. Unfortunately, spike detection performances for MUA detection are difficult to properly evaluate in simulation. MUAs are generated by the simultaneous activity of large populations of spatially distributed and interconnected neurons, a behavior that is difficult to emulate and explore on a synthetic dataset. Therefore, MUAs are quantified here on the basis of the information provided by the in vivo experiments. An example of MUA detection from a channel without neurons close enough to the electrode to allow identifying single-unit APs can be seen in Figure 4.20. The RMS multiplier used to find the threshold must be set to a value significantly lower than that used for the single AP detection, and here is set to 5.5. A more stable threshold compared to that of single AP detection can be observed, which is due to the exclusion of the MUA contribution from the RMS estimation, while MUA fluctuations during AP detection were treated as noise. The results are a smoother threshold change between the different timeframes and the ability to also accurately detect smaller fluctuations at the beginning and at the end of MUAs.

The ICMS experiments evoked a response visible in both the LFP and the high frequency domain, that allow to perform a comparison with the MUA detection. A stereotyped response, as shown in Figure 12, has been evoked and, therefore, reliably detected in the six experiments for 12, 20, 26, 27, 27, and 28 trials out of the 28 given stimuli. On all the trials where a response was visible in the LFP domain, the spike detector highlighted MUAs correspond to the LFP negative peaks. Figure 12 shows an example of a stereotyped evoked response where MUAs are detected in channels near the stimulation site after a silent period of 170 ms from the ICMS and further expands rhythmically in repetitions spreading across multiple channels of the linear probe. In comparison, the activity detected before stimulation shows some spurious desynchronized spiking activity.

The clock cycles required for each component of the design to produce the result are reported in Table 4.1, where the latency of each pipeline component is evaluated, from the acquisition of samples from the main RhythmStim loop to the writing of the results in the output FIFOs. The cycles required are intrinsically dependent on the SNEO parameters k, which in this design is assumed to be 4. Table 4.2 compares the FPGA logic consumed by the Intan RhythmStim design by default without any addition and the logic used after the modified implementation, highlighting the amount of space left available on the FPGA for the eventual further development of other functionalities. This led to a power consumption reported by the Xilinx XPower Analyzer of the modified design with spike detector of 1.002 W, with an increase of 0.096 W over the default design consumption of 0.906 W.

The first design constraint of the system is the sub-millisecond latency between a neuronal spike peak in the biological domain and its detection and digital communication. The latency of the system can be calculated from Table 3. Each of the 16 pairs of samples is acquired at 25 kHz, thus the total system sampling rate is 400 kHz. Considering the spike detector working frequency of 100 MHz, each pair disposes of 250 clock cycles to be elaborated, hence 125 cycles for each sample. The design requires 96 clock cycles to process a single sample, resulting in about 1 μs of processing time. The detection can be algorithmically found after only 14 samples from a spike peak, since the k NEO output evaluates the energy of the central sample in the $2k+1$ window and, in turn, the smoothing refers to the central energy value of the Bartlett window of $4k + 1$, where $k = 4$. Taking into account the processing time and the channel sampling period of 40 μs, the time required to detect a spike is approximately half a millisecond. The communication latency depends on the UART baud rate: Assuming a rate of 115'200, 4 bytes can
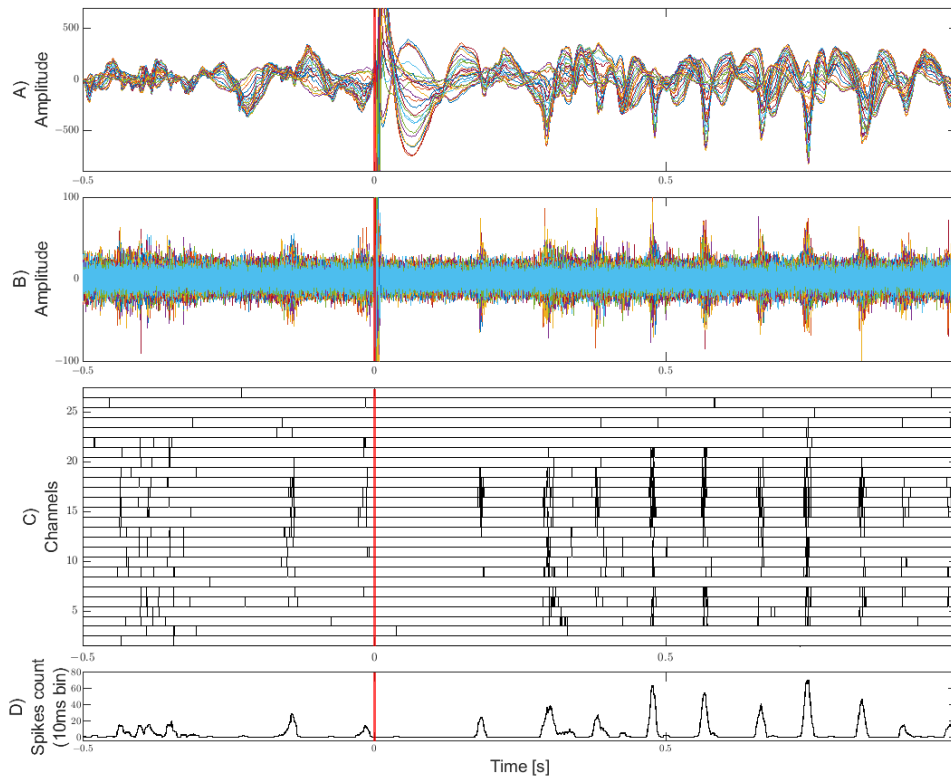
Figure 4.21: ICMS evoked response in a 1.5 s window. The red bar at time 0 corresponds to a cathodic to anodic ICMS of maximum amplitude of 200 μs per phase injected by the fifteenth channel every 10 s. A: LFP evoked response enhanced by band-pass filtering the signal between 5 and 200 Hz. B: Spiking activity enhanced by high-pass filtering the signal with a cutoff frequency of 300 Hz. C: Raster plot of MUA detection on data recorded by the linear probe. Channel 1 is the deepest in the barrel cortex, channels 28 to 32 are excluded being outside the cortex. The electrode of channel 8 has a higher impedance and is not recording properly. Before the stimulation, a random firing pattern can be observed from −400 to −300 ms and a spontaneous synchronous activation at −140 ms. After the stimulation, a synchronous activation of a neuronal population is observed spreading across the different channels. D: Cumulative spiking activity (instantaneous firing rate) of the channels in a moving sum window of 10 ms.

Component	Clock Cycles to Output	Notes
Samples preprocessing	7	cross-clock and samples format
High-pass filter	11	complete the filter state after 17
Savitzky-Golay fitting	15	8 + mask length
SNEO	34	$18 + 4 \times k\,(k = 4)$
Thresholding	5	
Local minimum	20	$4 \times k + 4\,(k = 4)$
Samples post-processing	4	writing to output FIFOs
Threshold estimation[1]	11	the square root and 8 more cycles are required every 2^{15} samples
Total	96	125 cycles are available between the two samples

Table 4.1: **Clock cycles required by the design components** to provide the output. [1] Threshold estimation does not influence the total cycles count since no other components wait for its output.

Logic	Default	Custom	Increment	Available
Slice register	8883	13.770	4887	54.576
Slice LUT	17.775	23.065	5290	27.288
BRAM16	69	76	7	116
BRAM8	0	15	15	232
DSP48A1	8	19	11	58

Table 4.2: **Logic utilization** of designs.

be transferred in less than 350 μs. This satisfies the initial constraint of the sub-millisecond processing time required from a spike peak to its detection and propagation, for a fast and reliable closed-loop system design. Obviously, the time required to transfer the spikes information via the USB to the host computer is affected by different factors, but considering the privileged USB communication and the 1 ms polling by the host application, the spike receiving latency will be of a few milliseconds at most. The second constraint was to have a higher system accuracy compared to the spike detection included in the default RhythmStim design. The detection accuracy of this work allows for the detection of single-unit APs with a great precision of up to 92%, with a reduced number of false positives and without false detections during the post-ICMS artifact. Furthermore, the spike detector can be used to provide a precise firing profile of MUAs that, due to the low SNR, are difficult to correctly recognize with a standard threshold crossing approach. The firing-independent threshold helps in this by providing a stable threshold value, especially when detecting MUAs, and it has the valuable advantage of avoiding hand-tuning the threshold for each channel, an important limitation of the default spike detection. As already mentioned, our recording from the rat barrel cortex showed strong APs –with a similar shape– only on few channels per record, while MUAs were recorded by most of the channels. For this reason, a spike sorter has not been included in the design. Table 4.3 shows a comparison with other similar recent works. Work from Murphy, M. at al. [140] is the most similar, being developed on the same recording system, while works from Wang, P.K. et al. [122] and Luan, S. et al. [141] use only the same headstage. Particularly, the latter is a battery-powered standalone platform that logs data on a SD card and therefore, could be considered to belong to another category of devices.

	This Work	Default	[140]	[122]	[141]
AP detection accuracy (%)	92	N/A	90.7	80–96[1]	N/A
Latency (ms)	~ 0.5	0.2	0.3–0.8	1.96	0.1
Supported channels	32	8	8	1	32
Automatic threshold	✓	✗	✗	✓	✓
Stimulation artifact dealing	✓	✗	✓	✗	✗
MUA detection	✓	$\sim$	✓	✗	✗
Sorting	✗	✗	✗	✓[2]	✓[2]
UDP spike communication	✓	✗	✗	✗	✗
Use Intan RHS	✓	✓	✓	✓[3]	✓[3]
Code availability	✓	✓	✓	✗	✓

Table 4.3: Comparison of this work with other works including the default spike detection of the Intan RHS stimulation/recording system. [1] On spike sorting; [2] off-line clustering with template matching; [3] headstage only.

4.7 SYNCH proof of concept experiments

The memristors platform currently require the communication to pass from a computer to be applied, causing this link of the communication to introduce a non-deterministic latency. Thus, to validate the local integration, experiments were performed both with and without the memristors setup, allowing to test both the overall latency of the system with direct hardware connection –without memristors– and overall information processing of the entire system chain –with memristors– For the configuration without memristors, the spiking events detected by the Intan RHS controller were streamed to the CU, which forwarded the activity to the SNN. Within the SNN, a recurrently connected network of artificial neurons was stimulated with received events, and the activity of the silicon neurons was again fed back to the CU. Here, the CU performed a simple rate estimation by counting incoming events and binning them in a 10 ms window. If the event count within this time-window exceeded a threshold, a stimulation event was issued and routed to the Intan RHS controller. The delays imposed by the path from source to destination via the CU is deterministic and was measured at the interfaces of the corresponding Setups. It has been measured in 816 μs from SNN to RHS and 1.2 ms from the Intan RHS controller to the SNN. This, summed with the small time required by the Intan RHS controller to stream an event from a spike onset and the time to trigger a neuron in the SNN, keeps the timing very close to those of a biological processing of the information. The memristors setup, when included, was receiving events forwarded from the CU prior to be sent to the SNN. The activity was applied to a memristor with a pulse of an amplitude proportional to the number of spikes in a batch of 10 ms received from a chosen channel. This caused a decay in the memristor resistance, which is dependent on the frequency and the amplitude of the applied pulses. Only for the time the memristor resistance was still lower than a threshold, the setup propagated the spiking activity retained by the system in the 10 ms batch to the SNN through the CU, mimicking the role of a synapse in a high excitability state. The 10 ms batch approach was included to allow for the computer governing the memristors to deal with the high number of events received in a way less influenced by the non deterministic managing of the timing in the loop. The overall setup is shown in Figure 4.22, together with the conceptual scheme 4.23.

This experiment was important to test the deployed systems in a real-time processing of information and data exchange, to verify that the components behave as expected, even if the resulting spiking activity
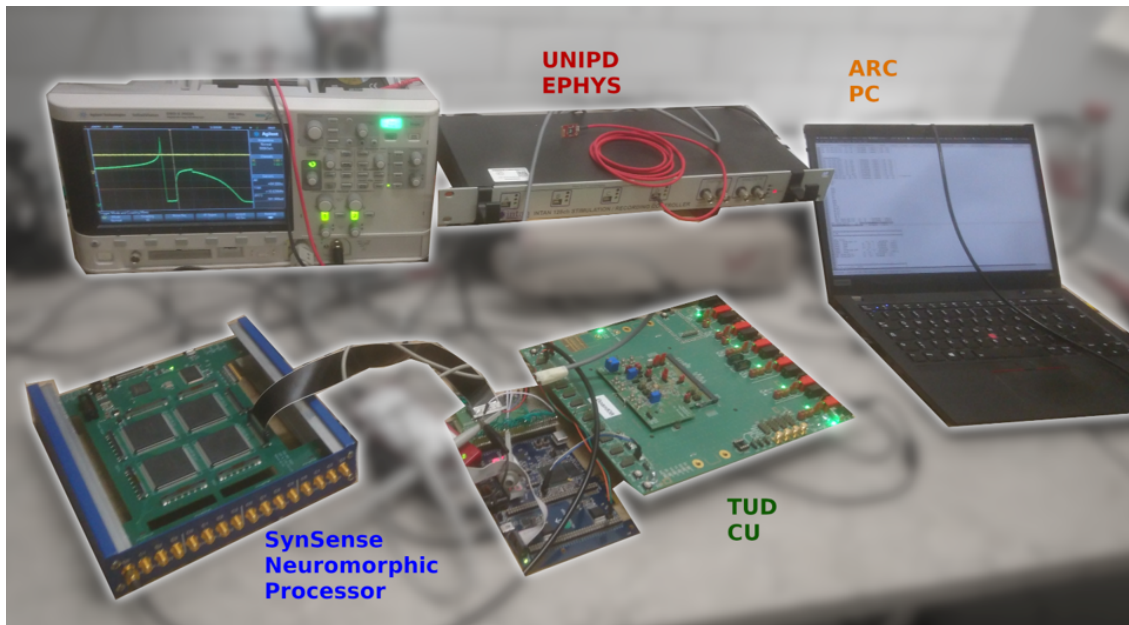
Figure 4.22: Locally integrated setups. The Neuromorphic Processor (Bottom Left) is interfaced with the CU via the FPGA and a 50-pin ribbon cable. The Intan RHS controller and the memristors computer (Top Center and Right) are interfaced via UART. The Oscilloscope on the top left allows observing the artificial membrane potential of a neuron (Green Trace), as a response to individual Intan RHS controller channel activity (Yellow Trace)

of the barrel cortex was not brought into a significant regime. The next integration phases will include the direct communication also with the memristors controller together with the implementation of the homeostasis rules, to avoid the binning of the activity and to open a full real-time processing of the data in the the closed-loop. Also, to complete the proof of concept and to move into a meaningful conditioning of neuronal activity, online recognition of the SNN activity in the CU by a linear classifier will be included. The classification has been already tested off-line on prerecorded data fed to the SNN, and demonstrated great performance in the detection of both the whisker stimulation and ICMS, after some tens of trials of training only.
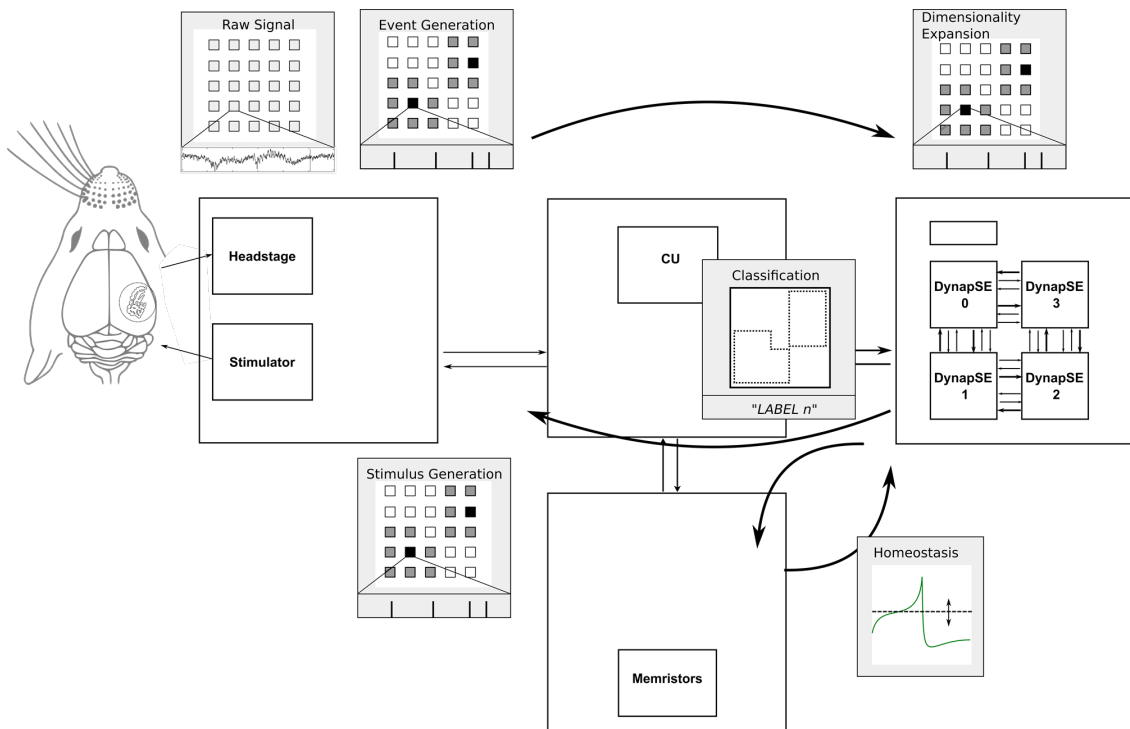
Figure 4.23: Full closed-loop setup. Acquired raw data acts are processed to extract spiking data from the Intan RHS controller. The CU forwards this data, stimulating the Neuromorphic Processor which acts as a reservoir and expands the dimensionality of the incoming data. Outgoing events from the Neuromorphic Processor are linearly classified by the CU and a stimulus message is sent to the Intan RHS controller, triggering Stimulus generation. Simultaneously, the CU computes firing rates of artificial neuron populations, and forwards them to the memristors setup. Here a homeostasis-rule formulates adjustments in the artificial neuron models parameters, keeping the population in a stable operating regime

5

Conclusion

In this thesis, I investigated the recording and stimulation of the neuronal activity of the barrel cortex in urethane anesthetized rats. I presented the development of an entire system that allows the precise and fast, at sub- millisecond, detection of the spiking activity during an in-vivo experiment. The system is developed on the RHS stimulation/recording controller from Intan technologies, and it is deployed alongside the original software and FPGA implementation of the device. It consists of an hardware spikes detector based on the SNEO and an accurate estimation of a SNEO threshold based on the noise baseline of the recordings of each channel. It also include a software extension of the original GUI of the controller, that allow to control the detection parameters and to visualize the detection results. This implementation supports an headstage of 32 channels recording the activity from 32 microelectrodes.

I then presented an electrophysiological characterization of the neural activity evoked by applying ICMS to the somatosensory barrel cortex of rats in a deep anesthesia state induced by urethane. The ICMS can evoke spindles of 11 Hz frequency synchronizing the activity across the entire barrel cortex after an initial inhibition of the activity of about 120-130 ms. These spindles have a wide range of duration, up to seconds, and present many oscillations, up to a dozen. They originate from the central layers (upper end of Va and IV) and span normally to layers III and Vb, especially during the stronger middle oscillations. I presented a characterization of the conditioning of these spindles, by modulating the oscillation frequency using a train of electrical stimulations. I found that the spindle frequency is phase-locked to the stimulation frequency in a range from 5 to 20 Hz. Using then a combination of stimuli at different amplitude (5 to 20 μA) and frequency (6 to 20 Hz), I described the overall activity undergoing the post-ICMS in the barrel cortex as a nonlinear dynamical system, following the phenomenon of a macroscopic, self-sustained oscillator, described by the Arnold's tongues.

I also found that the spindles evoked by ICMS seem to not involve the thalamocortical loops, suggesting a strictly local population processing. This is contrary to what is commonly described in the literature relative on sleep spindles during SWS [142], suggesting that it could be a different phenomenon. These spindles may also involve adjacent barrels near the ICMS site, and for this reason it would be interesting to monitor the adjacent areas using a probe with multiple shanks.

Simulations conducted in partnership with the Graz University of Technology have shown that this spindling phenomenon is reproducible by simulating the experiment on a networks of 500 point current-based generalized integrate-and-fire neurons (100 inhibitory and 400 excitatory randomly connected).

I estimated the number of neurons that are stimulated in the half-radius surrounding the stimulating electrode, given the current injected, the barrel neuronal density and the tissue conductance. We found that a current injection to a population corresponding to that reached by an ICMS of 10 to 20 μA amplitude caused the simulated neuronal population to behave similarly as MUA during spindles shown in this work. Neurons activity was oscillating between a high firing rate phase and a silent period, to then return in a *normal regime* after some hundreds of ms. This would suggest a resonance phenomenon between the activity of inhibitory and excitatory neurons during the evoked spindles, but it currently does not provide enough insights to exclude the involvement of other brain areas.

To my knowledge, this is the first work that uses ICMS to evoke and modulate spindles in the barrel cortex of rats. My findings support previous research suggesting that stimulation can modulate brain activity, but my study is unique because I characterized this phenomenon modulating the spindle frequency. This adds to the existing body of research on brain activity and stimulation in rodents new insights into their dynamics, and contributes to the field of neuroscience by providing a new experimental model and a potential avenue for further investigation. The significance of my findings lies in their potential implications for understanding brain function and dysfunction. Unfortunately, the use of a urethane anesthetized model only and a yet lack of a general and precise understanding of the role of these spindles in the literature, poses some limitations on how to exploit this phenomenon. For example, further investigations in awake animal, or under a different anesthesia could provide a better disclosure of this spindles origination: if strictly tied to the slow wave sleep, similar to the state caused by the deep anesthesia state induced by the urethane, the spindles should disappear or transform.

The barrel cortex is a somatosensory area and integrates information from the whiskers, tactile organs used for navigation. Would it be possible to change the perception of a rat by changing the spindling activity? Spindles have been strongly related to learning and synaptic development processes [143, 144]. By modulating the frequency of this activity, so changing the timing, could maybe lead to a different perception of space or to store information about objects and environment on a different scale size. Also, by imposing spindles by ICMS during the sleep may be possible that the memorization of a newly explored environment could be enhanced. Spindles, then, are a phenomenon diffuse throughout the cortex. A characterization similar to what as been done here could be performed for other cortical areas, as in the sensory or in the motor cortex, potentially leading to similar results. Once how the spindles precisely re-

late to the learning and memory process will be unveiled, the modulation of this activity during the SWS can become a precious tool for both the treatment and the training in neurological disorders, specially in diseases causing memory impairments as Alzheimer and Dementia.

Currently, the capability of modulating the spindles in a predictable way only provides a great test-bench for the closed-loop paradigm of the SYNCH objective, even if still lack of a practical purpose. This work reinforced the feasibility of the project of creating a hybrid system connecting a BNN in the brain of a living animal and a SNN on a chip. The development of the real-time bidirectional interface and its characterization demonstrate the viability of this approach and provide important insights into the modulation of neural activity in living organisms.

Future perspective

The mesolimbic pathway is a collection of dopamine-releasing neurons that project from the ventral tegmental area (VTA) to the ventral striatum (VS) in mammals, including humans. It is a component of the medial forebrain bundle (MFB), which is a set of neural pathways that mediate brain stimulation reward. This pathway regulates various cognitive processes such as incentive salience, motivation, reinforcement learning, and fear. The depletion of dopamine in this pathway or damage to its origin site can decrease the willingness of an animal to obtain a reward. Additionally, the firing rate of neurons in the mesolimbic pathway increases during the anticipation of reward, which may contribute to cravings.

To demonstrate the goodness of the SYNCH system, its first application will consists in treating neurological disorders by rescuing motivation in a rat model of dopaminergic deficiency, which is related to conditions such as depression, schizophrenia, and Parkinson's disease. In the first place, electrophysiological activity will be investigated in the VS during the formation of an association between auditory cues and MFB stimulation in both the anesthetized and the freely moving animals. Then a multivariate reinforcement learning task (MRLT) will be designed, that included classical and operant conditioning trials that were rewarded either by natural (water) or artificial (MFB stimulation) reinforcers. Neuronal activity is recorded while rats perform a task, and analyzed the activity of tonically active neurons during different events of the task, and characterized the responses during the formation of an association with learning. In general, tonically active neurons activity patterns consist of a fast excitatory response followed by a prolonged suppression. The information is conveyed by the duration and amplitude of

the excitatory and inhibitory components, and will be used to train the SNN in accomplishing the task. The study found that in behaving animals, operant conditioning trials rewarded by natural and artificial reinforcers (MFB stimulation) had similar acquisition rates and performance levels. Additionally, by considering the activity of groups of neurons, or neuronal ensembles, the information content is enhanced.

The work done so far in the barrel cortex of urethane anesthetized rats shown to be a promising technique to test the capability of the system and tune it towards this scope. It is crucial in gain new insights on computational properties of SNN and the ways to control the dynamics of the interconnected brain networks. Furthermore, it will represent a tool to investigate emerging properties and to better understand the computational properties of both the brain and artificial neural networks.

References

[1] A. L. Hodgkin and A. F. Huxley, "A quantitative description of membrane current and its application to conduction and excitation in nerve," *The Journal of Physiology*, vol. 117, no. 4, pp. 500–544, 1952. [Online]. Available: https://physoc.onlinelibrary.wiley.com/doi/abs/10.1113/jphysiol.1952.sp004764

[2] D. R. Humphrey and E. M. Schmidt, *Extracellular Single-Unit Recording Methods*. Totowa, NJ: Humana Press, 1990, pp. 1–64. [Online]. Available: https://doi.org/10.1385/0-89603-185-3:1

[3] G. H. Kim, K. Kim, E. Lee, T. An, W. Choi, G. Lim, and J. H. Shin, "Recent progress on microelectrodes in neural interfaces," *Materials*, vol. 11, no. 10, 2018. [Online]. Available: https://www.mdpi.com/1996-1944/11/10/1995

[4] M. E. J. Obien and U. Frey, *Large-Scale, High-Resolution Microelectrode Arrays for Interrogation of Neurons and Networks*. Cham: Springer International Publishing, 2019, pp. 83–123. [Online]. Available: https://doi.org/10.1007/978-3-030-11135-9_4

[5] M. E. Spira and A. Hai, "Multi-electrode array technologies for neuroscience and cardiology," *Nature Nanotechnology*, vol. 8, no. 2, pp. 83–94, Feb 2013. [Online]. Available: https://doi.org/10.1038/nnano.2012.265

[6] Y. Nam and B. C. Wheeler, "In vitro microelectrode array technology and neural recordings," *Critical Reviews™ in Biomedical Engineering*, vol. 39, no. 1, pp. 45–61, 2011.

[7] A. Destexhe and C. Bédard, *Local Field Potentials: LFP*. New York, NY: Springer New York, 2020, pp. 1–12. [Online]. Available: https://doi.org/10.1007/978-1-4614-7320-6_548-2

[8] A. L. Hodgkin and A. F. Huxley, "A quantitative description of membrane current and its application to conduction and excitation in nerve," *J Physiol*, vol. 117, no. 4, pp. 500–544, Aug. 1952.

[9] M. Morgan, M. Christie, J. Macdonald, and et Al., "Multiunit activity," in *Encyclopedia of Psychopharmacology*.   Berlin, Heidelberg: Springer Berlin Heidelberg, 2010, pp. 809–809.

[10] J. J. Jun, N. A. Steinmetz, J. H. Siegle, D. J. Denman, M. Bauza, B. Barbarits, A. K. Lee, C. A. Anastassiou, A. Andrei, Ç. Aydın, M. Barbic, T. J. Blanche, V. Bonin, J. Couto, B. Dutta, S. L. Gratiy, D. A. Gutnisky, M. Häusser, B. Karsh, P. Ledochowitsch, C. M. Lopez, C. Mitelut, S. Musa, M. Okun, M. Pachitariu, J. Putzeys, P. D. Rich, C. Rossant, W.-l. Sun, K. Svoboda, M. Carandini, K. D. Harris, C. Koch, J. O'Keefe, and T. D. Harris, "Fully integrated silicon probes for high-density recording of neural activity," *Nature*, vol. 551, no. 7679, pp. 232–236, Nov 2017. [Online]. Available: https://doi.org/10.1038/nature24636

[11] J. Scholvin, J. P. Kinney, J. G. Bernstein, C. Moore-Kochlacs, N. Kopell, C. G. Fonstad, and E. S. Boyden, "Close-packed silicon microelectrodes for scalable spatially oversampled neural recording," *IEEE Transactions on Biomedical Engineering*, vol. 63, no. 1, pp. 120–130, Jan 2016.

[12] A. Berényi, Z. Somogyvári, A. J. Nagy, L. Roux, J. D. Long, S. Fujisawa, E. Stark, A. Leonardo, T. D. Harris, and G. Buzsáki, "Large-scale, high-density (up to 512 channels) recording of local circuits in behaving animals," *Journal of Neurophysiology*, vol. 111, no. 5, pp. 1132–1149, 2014, pMID: 24353300. [Online]. Available: https://doi.org/10.1152/jn.00785.2013

[13] S. Butovas and C. Schwarz, "Spatiotemporal effects of microstimulation in rat neocortex: A parametric study using multielectrode recordings," *Journal of Neurophysiology*, vol. 90, no. 5, pp. 3024–3039, 2003, pMID: 12878710. [Online]. Available: https://doi.org/10.1152/jn.00245. 2003

[14] E. J. Tehovnik, "Electrical stimulation of neural tissue to evoke behavioral responses," *Journal of Neuroscience Methods*, vol. 65, no. 1, pp. 1–17, 1996. [Online]. Available: https://www.sciencedirect.com/science/article/pii/016502709500131X

[15] S. N. Flesher, J. L. Collinger, S. T. Foldes, J. M. Weiss, J. E. Downey, E. C. Tyler-Kabara, S. J. Bensmaia, A. B. Schwartz, M. L. Boninger, and R. A. Gaunt, "Intracortical microstimulation of human somatosensory cortex," *Science translational medicine*, vol. 8, no. 361, pp. 361ra141–361ra141, 2016.

[16] A. Pascual-Leone, V. Walsh, and J. Rothwell, "Transcranial magnetic stimulation in cognitive neuroscience–virtual lesion, chronometry, and functional connectivity," *Current opinion in neurobiology*, vol. 10, no. 2, pp. 232–237, 2000.

[17] M. Meinzer, D. Antonenko, R. Lindenberg, S. Hetzer, L. Ulm, K. Avirame, T. Flaisch, and A. Flöel, "Electrical brain stimulation improves cognitive performance by modulating functional connectivity and task-specific activation," *Journal of Neuroscience*, vol. 32, no. 5, pp. 1859–1866, 2012.

[18] T. A. Woolsey and H. Van der Loos, "The structural organization of layer iv in the somatosensory region (si) of mouse cerebral cortex: the description of a cortical field composed of discrete cytoarchitectonic units," *Brain research*, vol. 17, no. 2, pp. 205–242, 1970.

[19] M. F. Jacquin and R. W. Rhoades, "Central projections of the normal and 'regenerate' infraorbital nerve in adult rats subjected to neonatal unilateral infraorbital lesions: a transganglionic horseradish peroxidase study," *Brain Research*, vol. 269, no. 1, pp. 137–144, 1983. [Online]. Available: https://www.sciencedirect.com/science/article/pii/0006899383909708

[20] H. P. Killackey and K. Fleming, "The role of the principal sensory nucleus in central trigeminal pattern formation," *Developmental Brain Research*, vol. 22, no. 1, pp. 141–145, 1985. [Online]. Available: https://www.sciencedirect.com/science/article/pii/016538068590077X

[21] P. M. Ma, "Barrelettes—architectonic vibrissal representations in the brainstem trigeminal complex of the mouse. ii. normal post-natal development," *Journal of Comparative Neurology*, vol. 327, no. 3, pp. 376–397, 1993. [Online]. Available: https://onlinelibrary.wiley.com/doi/abs/10.1002/cne.903270306

[22] P. M. Ma and T. A. Woolsey, "Cytoarchitectonic correlates of the vibrissae in the medullary trigeminal complex of the mouse," *Brain Research*, vol. 306, no. 1, pp. 374–379, 1984. [Online]. Available: https://www.sciencedirect.com/science/article/pii/0006899384903901

[23] J. Chmielowska, G. E. Carvell, and D. J. Simons, "Spatial organization of thalamocortical and corticothalamic projection systems in the rat smi barrel cortex," *Journal of Comparative Neurology*, vol. 285, no. 3, pp. 325–338, 1989. [Online]. Available: https://onlinelibrary.wiley.com/doi/abs/10.1002/cne.902850304

[24] A. Peters, E. G. Jones, and I. T. Diamond, *The Barrel Cortex of Rodents: Volume 11: The Barrel Cortex of Rodents*.   Springer Science & Business Media, 1995, vol. 11.

[25] P. W. Land, S. A. Buffer Jr, and J. D. Yaskosky, "Barreloids in adult rat thalamus: Three-dimensional architecture and relationship to somatosensory cortical barrels," *Journal of Comparative Neurology*, vol. 355, no. 4, pp. 573–588, 1995. [Online]. Available: https://onlinelibrary.wiley.com/doi/abs/10.1002/cne.903550407

[26] D. J. Simons, "Response properties of vibrissa units in rat si somatosensory neocortex," *Journal of Neurophysiology*, vol. 41, no. 3, pp. 798–820, 1978, pMID: 660231. [Online]. Available: https://doi.org/10.1152/jn.1978.41.3.798

[27] C. Welker, "Microelectrode delineation of fine grain somatotopic organization of smi cerebral neocortex in albino rat," *Brain Research*, vol. 26, no. 2, pp. 259–275, 1971. [Online]. Available: https://www.sciencedirect.com/science/article/pii/S0006899371800045

[28] ——, "Receptive fields of barrels in the somatosensory neocortex of the rat," *Journal of Comparative Neurology*, vol. 166, no. 2, pp. 173–189, 1976. [Online]. Available: https://onlinelibrary.wiley.com/doi/abs/10.1002/cne.901660205

[29] P. W. Land and D. J. Simons, "Cytochrome oxidase staining in the rat smi barrel cortex," *Journal of Comparative Neurology*, vol. 238, no. 2, pp. 225–235, 1985. [Online]. Available: https://onlinelibrary.wiley.com/doi/abs/10.1002/cne.902380209

[30] K. D. Alloway, "Information Processing Streams in Rodent Barrel Cortex: The Differential Functions of Barrel and Septal Circuits," *Cerebral Cortex*, vol. 18, no. 5, pp. 979–989, 08 2007. [Online]. Available: https://doi.org/10.1093/cercor/bhm138

[31] C. Welker and T. A. Woolsey, "Structure of layer iv in the somatosensory neocortex of the rat: Description and comparison with the mouse," *Journal of Comparative Neurology*, vol. 158, no. 4, pp. 437–453, 1974. [Online]. Available: https://onlinelibrary.wiley.com/doi/abs/10.1002/cne.901580405

[32] J. F. Pasternak and T. A. Woolsey, "The number, size and spatial distribution of neurons in lamina iv of the mouse smi neocortex," *Journal of Comparative Neurology*, vol. 160, no. 3, pp. 291–306, 1975. [Online]. Available: https://onlinelibrary.wiley.com/doi/abs/10.1002/cne.901600303

[33] J. F. Staiger, R. Kötter, K. Zilles, and H. J. Luhmann, "Laminar characteristics of functional connectivity in rat barrel cortex revealed by stimulation with caged-glutamate," *Neuroscience Research*, vol. 37, no. 1, pp. 49–58, 2000. [Online]. Available: https://www.sciencedirect.com/science/article/pii/S0168010200000948

[34] A. Ayaz, A. Stäuble, M. Hamada, M.-A. Wulf, A. B. Saleem, and F. Helmchen, "Layer-specific integration of locomotion and sensory information in mouse barrel cortex," *Nature Communications*, vol. 10, no. 1, p. 2585, Jun 2019. [Online]. Available: https://doi.org/10.1038/s41467-019-10564-8

[35] B. Kolb, "Functions of the frontal cortex of the rat: a comparative review," *Brain research reviews*, vol. 8, no. 1, pp. 65–98, 1984.

[36] V. Reyes-Puerta, S. Kim, J.-J. Sun, B. Imbrosci, W. Kilb, and H. J. Luhmann, "High stimulus-related information in barrel cortex inhibitory interneurons," *PLOS Computational Biology*, vol. 11, no. 6, pp. 1–32, 06 2015. [Online]. Available: https://doi.org/10.1371/journal.pcbi.1004121

[37] Y. Shu, A. Hasenstaub, M. Badoual, T. Bal, and D. A. McCormick, "Barrages of synaptic activity control the gain and sensitivity of cortical neurons," *Journal of Neuroscience*, vol. 23, no. 32, pp. 10388–10401, 2003.

[38] C. C. Petersen and B. Sakmann, "Functionally independent columns of rat somatosensory barrel cortex revealed with voltage-sensitive dye imaging," *Journal of Neuroscience*, vol. 21, no. 21, pp. 8435–8446, 2001.

[39] M. Brecht, "Barrel cortex and whisker-mediated behaviors," *Current opinion in neurobiology*, vol. 17, no. 4, pp. 408–416, 2007.

[40] E. Ahissar, R. Sosnik, K. Bagdasarian, and S. Haidarliu, "Temporal frequency of whisker movement. ii. laminar organization of cortical representations," *Journal of Neurophysiology*, vol. 86, no. 1, pp. 354–367, 2001, pMID: 11431516. [Online]. Available: https://doi.org/10.1152/jn.2001.86.1.354

[41] J. M. Gibson and W. I. Welker, "Quantitative studies of stimulus coding in first-order vibrissa afferents of rats. 2. adaptation and coding of stimulus parameters," *Somatosensory Research*, vol. 1, no. 2, pp. 95–117, 1983. [Online]. Available: https://doi.org/10.3109/07367228309144543

[42] M. F. Jacquin and R. W. Rhoadesi, "Cell structure and response properties in the trigeminal subnucleus oralis," *Somatosensory & Motor Research*, vol. 7, no. 3, pp. 265–288, 1990, pMID: 2174199. [Online]. Available: https://doi.org/10.3109/08990229009144709

[43] M. E. Diamond, M. von Heimendahl, P. M. Knutsen, D. Kleinfeld, and E. Ahissar, "'where' and 'what' in the whisker sensorimotor system," *Nature Reviews Neuroscience*, vol. 9, no. 8, pp. 601–612, Aug 2008. [Online]. Available: https://doi.org/10.1038/nrn2411

[44] E. Ahissar and T. Oram, "Thalamic Relay or Cortico-Thalamic Processing? Old Question, New Answers," *Cerebral Cortex*, vol. 25, no. 4, pp. 845–848, 11 2013. [Online]. Available: https://doi.org/10.1093/cercor/bht296

[45] K. Reinhold, A. D. Lien, and M. Scanziani, "Distinct recurrent versus afferent dynamics in cortical visual processing," *Nature Neuroscience*, vol. 18, no. 12, pp. 1789–1797, Dec 2015. [Online]. Available: https://doi.org/10.1038/nn.4153

[46] L. I. Schmitt, R. D. Wimmer, M. Nakajima, M. Happ, S. Mofakham, and M. M. Halassa, "Thalamic amplification of cortical connectivity sustains attentional control," *Nature*, vol. 545, no. 7653, pp. 219–223, May 2017. [Online]. Available: https://doi.org/10.1038/nature22073

[47] M. Deschênes, P. Veinante, and Z.-W. Zhang, "The organization of corticothalamic projections: reciprocity versus parity," *Brain Research Reviews*, vol. 28, no. 3, pp. 286–308, 1998. [Online]. Available: https://www.sciencedirect.com/science/article/pii/S0165017398000174

[48] S. M. Sherman and C. Koch, "The control of retinogeniculate transmission in the mammalian lateral geniculate nucleus," *Experimental Brain Research*, vol. 63, no. 1, pp. 1–20, Jun 1986. [Online]. Available: https://doi.org/10.1007/BF00235642

[49] L. Puelles, M. M. de-la Torre, S. Bardet, and J. Rubenstein, "Chapter 8 - hypothalamus," in *The Mouse Nervous System*, C. Watson, G. Paxinos, and L. Puelles, Eds.   San Diego: Academic Press, 2012, pp. 221–312. [Online]. Available: https://www.sciencedirect.com/science/article/pii/B9780123694973100081

[50] F. Clascá, P. Rubio-Garrido, and D. Jabaudon, "Unveiling the diversity of thalamocortical neuron subtypes," *European Journal of Neuroscience*, vol. 35, no. 10, pp. 1524–1532, 2012. [Online]. Available: https://onlinelibrary.wiley.com/doi/abs/10.1111/j.1460-9568.2012.08033.x

[51] H. S. Meyer, V. C. Wimmer, M. Hemberger, R. M. Bruno, C. P. de Kock, A. Frick, B. Sakmann, and M. Helmstaedter, "Cell Type–Specific Thalamic Innervation in a Column of Rat Vibrissal Cortex," *Cerebral Cortex*, vol. 20, no. 10, pp. 2287–2303, 06 2010. [Online]. Available: https://doi.org/10.1093/cercor/bhq069

[52] H. Markram, E. Muller, S. Ramaswamy, M. Reimann, M. Abdellah, C. Sanchez, A. Ailamaki, L. Alonso-Nanclares, N. Antille, S. Arsever, G. Kahou, T. Berger, A. Bilgili, N. Buncic, A. Chalimourda, G. Chindemi, J.-D. Courcol, F. Delalondre, V. Delattre, S. Druckmann, R. Dumusc, J. Dynes, S. Eilemann, E. Gal, M. Gevaert, J.-P. Ghobril, A. Gidon, J. Graham, A. Gupta, V. Haenel, E. Hay, T. Heinis, J. Hernando, M. Hines, L. Kanari, D. Keller, J. Kenyon, G. Khazen, Y. Kim, J. King, Z. Kisvarday, P. Kumbhar, S. Lasserre, J.-V. Le Bé, B. Magalhães,

A. Merchán-Pérez, J. Meystre, B. Morrice, J. Muller, A. Muñoz-Céspedes, S. Muralidhar, K. Muthurasa, D. Nachbaur, T. Newton, M. Nolte, A. Ovcharenko, J. Palacios, L. Pastor, R. Perin, R. Ranjan, I. Riachi, J.-R. Rodríguez, J. Riquelme, C. Rössert, K. Sfyrakis, Y. Shi, J. Shillcock, G. Silberberg, R. Silva, F. Tauheed, M. Telefont, M. Toledo-Rodriguez, T. Tränkler, W. Van Geit, J. Díaz, R. Walker, Y. Wang, S. Zaninetta, J. DeFelipe, S. Hill, I. Segev, and F. Schürmann, "Reconstruction and simulation of neocortical microcircuitry," *Cell*, vol. 163, no. 2, pp. 456–492, Oct 2015. [Online]. Available: https://doi.org/10.1016/j.cell.2015.09.029

[53] F. Briggs and W. M. Usrey, "A fast, reciprocal pathway between the lateral geniculate nucleus and visual cortex in the macaque monkey," *Journal of Neuroscience*, vol. 27, no. 20, pp. 5431–5436, 2007. [Online]. Available: https://www.jneurosci.org/content/27/20/5431

[54] S. Ohno, E. Kuramoto, T. Furuta, H. Hioki, Y. R. Tanaka, F. Fujiyama, T. Sonomura, M. Uemura, K. Sugiyama, and T. Kaneko, "A Morphological Analysis of Thalamocortical Axon Fibers of Rat Posterior Thalamic Nuclei: A Single Neuron Tracing Study with Viral Vectors," *Cerebral Cortex*, vol. 22, no. 12, pp. 2840–2857, 12 2011. [Online]. Available: https://doi.org/10.1093/cercor/bhr356

[55] M. Brecht, "Barrel cortex and whisker-mediated behaviors," *Current Opinion in Neurobiology*, vol. 17, no. 4, pp. 408–416, 2007, sensory systems. [Online]. Available: https://www.sciencedirect.com/science/article/pii/S0959438807000918

[56] C. O'Reilly, E. Iavarone, J. Yi, and S. L. Hill, "Rodent somatosensory thalamocortical circuitry: Neurons, synapses, and connectivity," *Neuroscience & Biobehavioral Reviews*, vol. 126, pp. 213–235, 2021. [Online]. Available: https://www.sciencedirect.com/science/article/pii/S0149763421001305

[57] D. J. Simons, "Multi-whisker stimulation and its effects on vibrissa units in rat sml barrel cortex," *Brain research*, vol. 276, no. 1, pp. 178–182, 1983.

[58] A. Scaglione, K. A. Moxon, J. Aguilar, and G. Foffani, "Trial-to-trial variability in the responses of neurons carries information about stimulus location in the rat whisker thalamus," *Proceedings of the National Academy of Sciences*, vol. 108, no. 36, pp. 14956–14961, 2011.

[59] D. J. Krupa, M. C. Wiest, M. G. Shuler, M. Laubach, and M. A. L. Nicolelis, "Layer-specific somatosensory cortical activation during active tactile discrimination," *Science*, vol. 304, no. 5679, pp. 1989–1992, 2004. [Online]. Available: https://www.science.org/doi/abs/10.1126/science.1093318

[60] D. J. Simons and G. E. Carvell, "Thalamocortical response transformation in the rat vibrissa/barrel system," *Journal of Neurophysiology*, vol. 61, no. 2, pp. 311–330, 1989, pMID: 2918357. [Online]. Available: https://doi.org/10.1152/jn.1989.61.2.311

[61] D. E. Feldman, "Timing-based ltp and ltd at vertical inputs to layer ii/iii pyramidal cells in rat barrel cortex," *Neuron*, vol. 27, no. 1, pp. 45–56, 2000. [Online]. Available: https://www.sciencedirect.com/science/article/pii/S0896627300000088

[62] V. Jacob, D. J. Brasier, I. Erchova, D. Feldman, and D. E. Shulz, "Spike timing-dependent synaptic depression in the in vivo barrel cortex of the rat," *Journal of Neuroscience*, vol. 27, no. 6, pp. 1271–1284, 2007. [Online]. Available: https://www.jneurosci.org/content/27/6/1271

[63] M. Steriade, I. Timofeev, and F. Grenier, "Natural waking and sleep states: a view from inside neocortical neurons," *Journal of neurophysiology*, vol. 85, no. 5, pp. 1969–1985, 2001.

[64] L. M. Fernandez and A. Lüthi, "Sleep spindles: mechanisms and functions," *Physiological reviews*, vol. 100, no. 2, pp. 805–868, 2020.

[65] S. An, W. Kilb, and H. J. Luhmann, "Sensory-evoked and spontaneous gamma and spindle bursts in neonatal rat motor cortex," *Journal of Neuroscience*, vol. 34, no. 33, pp. 10 870–10 883, 2014. [Online]. Available: https://www.jneurosci.org/content/34/33/10870

[66] T. O. Bergmann and J. Born, "Phase-amplitude coupling: a general mechanism for memory processing and synaptic plasticity?" *Neuron*, vol. 97, no. 1, pp. 10–13, 2018.

[67] J.-W. Yang, V. Reyes-Puerta, W. Kilb, and H. J. Luhmann, "Spindle bursts in neonatal rat cerebral cortex," *Neural Plasticity*, vol. 2016, p. 3467832, Jan 2016. [Online]. Available: https://doi.org/10.1155/2016/3467832

[68] T. Hashiguchi, H. Kobayashi, T. Tosaka, and B. Libet, "Two muscarinic depolarizing mechanisms in mammalian sympathetic neurons," *Brain research*, vol. 242, no. 2, pp. 378–382, 1982.

[69] G. Kleiner-Fisman, D. N. Fisman, E. Sime, J. A. Saint-Cyr, A. M. Lozano, and A. E. Lang, "Long-term follow up of bilateral deep brain stimulation of the subthalamic nucleus in patients with advanced parkinson disease," *Journal of neurosurgery*, vol. 99, no. 3, pp. 489–495, 2003.

[70] M. Hallett, "Transcranial magnetic stimulation: a primer," *Neuron*, vol. 55, no. 2, pp. 187–199, 2007.

[71] A. L. Benabid, "Deep brain stimulation for parkinson's disease," *Current opinion in neurobiology*, vol. 13, no. 6, pp. 696–706, 2003.

[72] Y.-C. Lai and T. Tél, *Transient chaos: complex dynamics on finite time scales*. Springer Science & Business Media, 2011, vol. 173.

[73] D. Goldobin, M. Rosenblum, and A. Pikovsky, "Controlling oscillator coherence by delayed feedback," *Physical Review E*, vol. 67, no. 6, p. 061119, 2003.

[74] N. Kopell *et al.*, "We got rhythm: Dynamical systems of the nervous system," *Notices of the AMS*, vol. 47, no. 1, pp. 6–16, 2000.

[75] P. A. Tass, "A model of desynchronizing deep brain stimulation with a demand-controlled coordinated reset of neural subpopulations," *Biological cybernetics*, vol. 89, no. 2, pp. 81–88, 2003.

[76] P. Suffczynski, S. Kalitzin, and F. L. Da Silva, "Dynamics of non-convulsive epileptic phenomena modeled by a bistable neuronal network," *Neuroscience*, vol. 126, no. 2, pp. 467–484, 2004.

[77] M. Rosenblum and A. Pikovsky, "Delayed feedback control of collective synchrony: An approach to suppression of pathological brain rhythms," *Physical review E*, vol. 70, no. 4, p. 041904, 2004.

[78] P. A. Tass, C. Hauptmann, and O. V. Popovych, "Development of therapeutic brain stimulation techniques with methods from nonlinear dynamics and statistical physics," *International Journal of Bifurcation and Chaos*, vol. 16, no. 07, pp. 1889–1911, 2006.

[79] O. V. Popovych, C. Hauptmann, and P. A. Tass, "Effective desynchronization by nonlinear delayed feedback," *Physical review letters*, vol. 94, no. 16, p. 164102, 2005.

[80] S. H. Strogatz, "From kuramoto to crawford: exploring the onset of synchronization in populations of coupled oscillators," *Physica D: Nonlinear Phenomena*, vol. 143, no. 1-4, pp. 1–20, 2000.

[81] J. A. Acebrón, L. L. Bonilla, C. J. P. Vicente, F. Ritort, and R. Spigler, "The kuramoto model: A simple paradigm for synchronization phenomena," *Reviews of modern physics*, vol. 77, no. 1, p. 137, 2005.

[82] L. Glass, "Synchronization and rhythmic processes in physiology," *Nature*, vol. 410, no. 6825, pp. 277–284, 2001.

[83] M. L. Homer, A. V. Nurmikko, J. P. Donoghue, and L. R. Hochberg, "Sensors and decoding for intracortical brain computer interfaces," *Annual Review of Biomedical Engineering*, vol. 15, no. 1, pp. 383–405, 2013, pMID: 23862678. [Online]. Available: https://doi.org/10.1146/annurev-bioeng-071910-124640

[84] D. B. Strukov, G. S. Snider, D. R. Stewart, and R. S. Williams, "The missing memristor found," *nature*, vol. 453, no. 7191, pp. 80–83, 2008.

[85] S. H. Jo, T. Chang, I. Ebong, B. B. Bhadviya, P. Mazumder, and W. Lu, "Nanoscale memristor device as synapse in neuromorphic systems," *Nano letters*, vol. 10, no. 4, pp. 1297–1301, 2010.

[86] S. Kvatinsky, D. Belousov, S. Liman, G. Satat, N. Wald, E. G. Friedman, A. Kolodny, and U. C. Weiser, "Magic—memristor-aided logic," *IEEE Transactions on Circuits and Systems II: Express Briefs*, vol. 61, no. 11, pp. 895–899, 2014.

[87] R. Waser, "Resistive non-volatile memory devices," *Microelectronic Engineering*, vol. 86, no. 7-9, pp. 1925–1928, 2009.

[88] B. Liu, H. Li, Y. Chen, X. Li, Q. Wu, and T. Huang, "Vortex: Variation-aware training for memristor x-bar," in *Proceedings of the 52nd Annual Design Automation Conference*, 2015, pp. 1–6.

[89] S. Zhou, X. Li, Y. Chen, S. T. Chandrasekaran, and A. Sanyal, "Temporal-coded deep spiking neural network with easy training and robust performance," in *Proceedings of the AAAI Conference on Artificial Intelligence*, vol. 35, no. 12, 2021, pp. 11 143–11 151.

[90] W. Maass and V. C. Storey, "Pairing conceptual modeling with machine learning," *Data & Knowledge Engineering*, vol. 134, p. 101909, 2021.

[91] H. Fang, Y. Zeng, and F. Zhao, "Brain inspired sequences production by spiking neural networks with reward-modulated stdp," *Frontiers in Computational Neuroscience*, vol. 15, p. 612041, 2021.

[92] Z. Bing, C. Meschede, F. Röhrbein, K. Huang, and A. C. Knoll, "A survey of robotics control based on learning-inspired spiking neural networks," *Frontiers in neurorobotics*, vol. 12, p. 35, 2018.

[93] M. Hopkins, G. Pineda-Garcia, P. A. Bogdan, and S. B. Furber, "Spiking neural networks for computer vision," *Interface Focus*, vol. 8, no. 4, p. 20180007, 2018.

[94] N. Kasabov and E. Capecci, "Spiking neural network methodology for modelling, classification and understanding of eeg spatio-temporal data measuring cognitive processes," *Information Sciences*, vol. 294, pp. 565–575, 2015.

[95] G. J. Benson, J. C. Thurmon, and W. J. Tranquilli, *Lumb & Jones' Veterinary Anesthesia*. Lippincott Williams & Wilkins, 1996.

[96] R. Fiáth, B. P. Kerekes, L. Wittner, K. Tóth, P. Beregszászi, D. Horváth, and I. Ulbert, "Laminar analysis of the slow wave activity in the somatosensory cortex of anesthetized rats," *European Journal of Neuroscience*, vol. 44, no. 3, pp. 1935–1951, 2016. [Online]. Available: https://onlinelibrary.wiley.com/doi/abs/10.1111/ejn.13274

[97] I. M. Devonshire, T. H. Grandy, E. J. Dommett, and S. A. Greenfield, "Effects of urethane anaesthesia on sensory processing in the rat barrel cortex revealed by combined optical imaging and electrophysiology," *European Journal of Neuroscience*, vol. 32, no. 5, pp. 786–797, 2010. [Online]. Available: https://onlinelibrary.wiley.com/doi/abs/10.1111/j.1460-9568.2010.07322.x

[98] M. Torao-Angosto, A. Manasanch, M. Mattia, and M. V. Sanchez-Vives, "Up and down states during slow oscillations in slow-wave sleep and different levels of anesthesia," *Frontiers in Systems Neuroscience*, vol. 15, 2021. [Online]. Available: https://www.frontiersin.org/articles/10.3389/fnsys.2021.609645

[99] S. Shimegi, T. Akasaki, T. Ichikawa, and H. Sato, "Physiological and anatomical organization of multiwhisker response interactions in the barrel cortex of rats," *J. Neurosci.*, vol. 20, no. 16, pp. 6241–6248, Aug. 2000.

[100] L. W. Swanson, "Brain maps 4.0-structure of the rat brain: An open access atlas with global nervous system nomenclature ontology and flatmaps," *J. Comp. Neurol.*, vol. 526, no. 6, pp. 935–943, Apr. 2018.

[101] M. Armstrong-James, K. Fox, and A. Das-Gupta, "Flow of excitation within rat barrel cortex on striking a single vibrissa," *Journal of Neurophysiology*, vol. 68, no. 4, pp. 1345–1358, 1992, pMID: 1432088. [Online]. Available: https://doi.org/10.1152/jn.1992.68.4.1345

[102] S. Pagliardini, S. Gosgnach, and C. T. Dickson, "Spontaneous sleep-like brain state alternations and breathing characteristics in urethane anesthetized mice," *PLOS ONE*, vol. 8, no. 7, p. null, 07 2013. [Online]. Available: https://doi.org/10.1371/journal.pone.0070411

[103] D. Derdikman, C. Yu, S. Haidarliu, K. Bagdasarian, A. Arieli, and E. Ahissar, "Layer-specific touch-dependent facilitation and depression in the somatosensory cortex during active whisking," *Journal of Neuroscience*, vol. 26, no. 37, pp. 9538–9547, 2006. [Online]. Available: https://www.jneurosci.org/content/26/37/9538

[104] E. J. Tehovnik, A. S. Tolias, F. Sultan, W. M. Slocum, and N. K. Logothetis, "Direct and indirect activation of cortical neurons by electrical microstimulation," *Journal of Neurophysiology*, vol. 96, no. 2, pp. 512–521, 2006, pMID: 16835359. [Online]. Available: https://doi.org/10.1152/jn.00126.2006

[105] S. Kim, T. Callier, G. A. Tabot, R. A. Gaunt, F. V. Tenore, and S. J. Bensmaia, "Behavioral assessment of sensitivity to intracortical microstimulation of primate somatosensory cortex,"

Proceedings of the National Academy of Sciences, vol. 112, no. 49, pp. 15 202–15 207, 2015. [Online]. Available: https://www.pnas.org/doi/abs/10.1073/pnas.1509265112

[106] S. Kim, T. Callier, G. A. Tabot, F. V. Tenore, and S. J. Bensmaia, "Sensitivity to microstimulation of somatosensory cortex distributed over multiple electrodes," *Frontiers in Systems Neuroscience*, vol. 9, 2015. [Online]. Available: https://www.frontiersin.org/articles/10.3389/fnsys.2015.00047

[107] R. Q. Quiroga, Z. Nadasdy, and Y. Ben-Shaul, "Unsupervised spike detection and sorting with wavelets and superparamagnetic clustering," *Neural Comput.*, vol. 16, no. 8, p. 1661–1687, aug 2004. [Online]. Available: https://doi.org/10.1162/089976604774201631

[108] M. Tambaro, M. Bisio, M. Maschietto, A. Leparulo, and S. Vassanelli, "Fpga design integration of a 32-microelectrodes low-latency spike detector in a commercial system for intracortical recordings," *Digital*, vol. 1, no. 1, pp. 34–53, 2021. [Online]. Available: https://www.mdpi.com/2673-6470/1/1/3

[109] G. N. Angotzi, F. Boi, A. Lecomte, E. Miele, M. Malerba, S. Zucca, A. Casile, and L. Berdondini, "SiNAPS: An implantable active pixel sensor CMOS-probe for simultaneous large-scale neural recordings," *Biosens. Bioelectron.*, vol. 126, pp. 355–364, Feb. 2019.

[110] B. C. Raducanu, R. F. Yazicioglu, C. M. Lopez, M. Ballini, J. Putzeys, S. Wang, A. Andrei, V. Rochus, M. Welkenhuysen, N. van Helleputte, S. Musa, R. Puers, F. Kloosterman, C. van Hoof, R. Fiáth, I. Ulbert, and S. Mitra, "Time multiplexed active neural probe with 1356 parallel recording sites," *Sensors (Basel)*, vol. 17, no. 10, Oct. 2017.

[111] J. D. Rolston, R. E. Gross, and S. M. Potter, "A low-cost multielectrode system for data acquisition enabling real-time closed-loop processing with rapid recovery from stimulation artifacts," *Front. Neuroeng.*, vol. 2, p. 12, Jul. 2009.

[112] S. Venkatraman, K. Elkabany, J. D. Long, Y. Yao, and J. M. Carmena, "A system for neural recording and closed-loop intracortical microstimulation in awake rodents," *IEEE Trans. Biomed. Eng.*, vol. 56, no. 1, pp. 15–22, Jan. 2009.

[113] G. Q. Bi and M. M. Poo, "Synaptic modifications in cultured hippocampal neurons: dependence on spike timing, synaptic strength, and postsynaptic cell type," *J. Neurosci.*, vol. 18, no. 24, pp. 10464–10472, Dec. 1998.

[114] L. Grosenick, J. H. Marshel, and K. Deisseroth, "Closed-loop and activity-guided optogenetic control," *Neuron*, vol. 86, no. 1, pp. 106–139, Apr. 2015.

[115] J. P. Newman, M.-F. Fong, D. C. Millard, C. J. Whitmire, G. B. Stanley, and S. M. Potter, "Optogenetic feedback control of neural activity," *Elife*, vol. 4, p. e07192, Jul. 2015.

[116] A. Savitzky and M. J. E. Golay, "Smoothing and differentiation of data by simplified least squares procedures," *Anal. Chem.*, vol. 36, no. 8, pp. 1627–1639, Jul. 1964.

[117] S. Mukhopadhyay and G. C. Ray, "A new interpretation of nonlinear energy operator and its efficacy in spike detection," *IEEE Trans. Biomed. Eng.*, vol. 45, no. 2, pp. 180–187, Feb. 1998.

[118] M. Tambaro, E. A. Vallicelli, G. Saggese, A. Strollo, A. Baschirotto, and S. Vassanelli, "Evaluation of in vivo spike detection algorithms for implantable MTA brain—silicon interfaces," *J. Low Power Electron. Appl.*, vol. 10, no. 3, p. 26, Sep. 2020.

[119] H. Azami and S. Sanei, "Spike detection approaches for noisy neuronal data: Assessment and comparison," *Neurocomputing*, vol. 133, pp. 491–506, Jun. 2014.

[120] B. Yu, T. Mak, X. Li, F. Xia, A. Yakovlev, Y. Sun, and C.-S. Poon, "Real-Time FPGA-Based multichannel spike sorting using hebbian eigenfilters," *IEEE J. Emerg. Sel. Top. Circuits Syst.*, vol. 1, no. 4, pp. 502–515, Dec. 2011.

[121] T. Tariq, M. H. Satti, M. Saeed, and A. M. Kamboh, "Low SNR neural spike detection using scaled energy operators for implantable brain circuits," *Annu. Int. Conf. IEEE Eng. Med. Biol. Soc.*, vol. 2017, pp. 1074–1077, Jul. 2017.

[122] P. K. Wang, S. H. Pun, C. H. Chen, E. A. McCullagh, A. Klug, A. Li, M. I. Vai, P. U. Mak, and T. C. Lei, "Low-latency single channel real-time neural spike sorting system based on template matching," *PLoS One*, vol. 14, no. 11, p. e0225138, Nov. 2019.

[123] D. Valencia and A. Alimohammad, "A real-time spike sorting system using parallel OSort clustering," *IEEE Trans. Biomed. Circuits Syst.*, vol. 13, no. 6, pp. 1700–1713, Dec. 2019.

[124] M. Tambaro and S. Vassanelli, "A firing rate independent threshold estimation for neuronal spike detection methods," in *2022 IEEE Biomedical Circuits and Systems Conference (BioCAS)*, 2022, pp. 583–586.

[125] D. Yael and I. Bar-Gad, "Filter based phase distortions in extracellular spikes," *PLoS One*, vol. 12, no. 3, p. e0174790, Mar. 2017.

[126] S. M. A. Zeinolabedin, F. M. Schuffny, R. George, F. Kelber, H. Bauer, S. Scholze, S. Hanzsche, M. Stolba, A. Dixius, G. Ellguth, D. Walter, S. Hoppner, and C. Mayr, "A 16-channel fully configurable neural SoC with 1.52 μW/Ch signal acquisition, 2.79 μW/Ch real-time spike classifier, and 1.79 TOPS/W deep neural network accelerator in 22 nm FDSOI," *IEEE Trans. Biomed. Circuits Syst.*, vol. 16, no. 1, pp. 94–107, Feb. 2022.

[127] A. Serb, J. Bill, A. Khiat, R. Berdan, R. Legenstein, and T. Prodromakis, "Unsupervised learning in probabilistic neural networks with multi-state metal-oxide memristive synapses," *Nature Communications*, vol. 7, no. 1, p. 12611, Sep 2016. [Online]. Available: https://doi.org/10.1038/ncomms12611

[128] S. Moradi, N. Qiao, F. Stefanini, and G. Indiveri, "A scalable multicore architecture with heterogeneous memory structures for dynamic neuromorphic asynchronous processors (dynaps)," *IEEE Transactions on Biomedical Circuits and Systems*, vol. PP, 08 2017.

[129] M. Szwed, K. Bagdasarian, and E. Ahissar, "Encoding of vibrissal active touch," *Neuron*, vol. 40, no. 3, pp. 621–630, 2003. [Online]. Available: https://www.sciencedirect.com/science/article/pii/S0896627303006718

[130] M. J. Higley and D. Contreras, "Nonlinear integration of sensory responses in the rat barrel cortex: an intracellular study in vivo," *J Neurosci*, vol. 23, no. 32, pp. 10190–10200, Nov. 2003.

[131] K. F. Ahrens and D. Kleinfeld, "Current flow in vibrissa motor cortex can phase-lock with exploratory rhythmic whisking in rat," *Journal of Neurophysiology*, vol. 92, no. 3, pp. 1700–1707, 2004, pMID: 15331651. [Online]. Available: https://doi.org/10.1152/jn.00020.2004

[132] E. Kublik, "Contextual impact on sensory processing at the barrel cortex of awake rat," *Acta Neurobiol Exp (Wars)*, vol. 64, no. 2, pp. 229–238, 2004.

[133] S. Shimegi, T. Ichikawa, T. Akasaki, and H. Sato, "Temporal characteristics of response integration evoked by multiple whisker stimulations in the barrel cortex of rats," *Journal of Neuroscience*, vol. 19, no. 22, pp. 10164–10175, 1999. [Online]. Available: https://www.jneurosci.org/content/19/22/10164

[134] S. Butovas, S. G. Hormuzdi, H. Monyer, and C. Schwarz, "Effects of electrically coupled inhibitory networks on local neuronal responses to intracortical microstimulation," *Journal of Neurophysiology*, vol. 96, no. 3, pp. 1227–1236, 2006, pMID: 16837655. [Online]. Available: https://doi.org/10.1152/jn.01170.2005

[135] S. Venkatraman, K. Elkabany, J. D. Long, Y. Yao, and J. M. Carmena *, "A system for neural recording and closed-loop intracortical microstimulation in awake rodents," *IEEE Transactions on Biomedical Engineering*, vol. 56, no. 1, pp. 15–22, 2009.

[136] H. Sakaguchi, "Cooperative phenomena in coupled oscillator systems under external fields," *Progress of theoretical physics*, vol. 79, no. 1, pp. 39–46, 1988.

[137] E. Ott and T. M. Antonsen, "Long time evolution of phase oscillator systems," *Chaos: An interdisciplinary journal of nonlinear science*, vol. 19, no. 2, p. 023117, 2009.

[138] L. D. Iasemidis, "Epileptic seizure prediction and control," *IEEE Transactions on Biomedical Engineering*, vol. 50, no. 5, pp. 549–558, 2003.

[139] L. B. Good, S. Sabesan, S. T. Marsh, K. Tsakalis, D. Treiman, and L. Iasemidis, "Control of synchronization of brain dynamics leads to control of epileptic seizures in rodents," *International journal of neural systems*, vol. 19, no. 03, pp. 173–196, 2009.

[140] M. Murphy, S. Buccelli, Y. Bornat, D. Bundy, R. Nudo, D. Guggenmos, and M. Chiappalone, "Improving an open-source commercial system to reliably perform activity-dependent stimulation," *J. Neural Eng.*, vol. 16, no. 6, p. 066022, Oct. 2019.

[141] S. Luan, I. Williams, M. Maslik, Y. Liu, F. De Carvalho, A. Jackson, R. Q. Quiroga, and T. G. Constandinou, "Compact standalone platform for neural recording with real-time spike sorting and data logging," *J. Neural Eng.*, vol. 15, no. 4, p. 046014, Aug. 2018.

[142] I. Timofeev and S. Chauvette, "The spindles: are they still thalamic?" *Sleep*, vol. 36, no. 6, pp. 825–826, Jun. 2013.

[143] A. Peyrache and J. Seibt, "A mechanism for learning with sleep spindles," *Philos Trans R Soc Lond B Biol Sci*, vol. 375, no. 1799, p. 20190230, Apr. 2020.

[144] R. Cox, W. F. Hofman, M. de Boer, and L. M. Talamini, "Local sleep spindle modulations in relation to specific memory cues," *NeuroImage*, vol. 99, pp. 103–110, 2014. [Online]. Available: https://www.sciencedirect.com/science/article/pii/S1053811914003930

Ringraziamenti

Non sono una persona che ama dilungarsi troppo nei ringraziamenti o nei commenti in generale, ma ci tengo a ringraziare le persone che ho incontrato fino ad ora lungo questo mio percorso qui a Padova, sia in accademia, sia fuori, sia a cavallo dei due ambienti.

Ringrazio i miei colleghi, ma sopratutto amici, Nicolò, Matteo e Manuel. Senza di voi questo viaggio non sarebbe stato lo stesso. Grazie a voi è stata una continua grande avventura.

Ringrazio tutti i miei coinquilini presenti e passati, di cui non farò tutti i nomi perché troppi. Tengo nel cuore un posto speciale per i primi incontrati, per aver reso il mio cambio di città una passeggiata.

Ringrazio Claudia, per avermi sempre dato supporto e amicizia (e per la correzione di questo lavoro). Ringrazio Amanda, per le uscite spensierate e la compagnia sincera.

Ringrazio Stefano per l'opportunità datami e la fiducia dimostratami ogni giorno.
Ringrazio Marta M. per aver condiviso la sua conoscenza e Alessandro per essere sempre stato disponibile a scambiare un opinine.
Ringrazio Marta B. per avermi instradato ed Enzo per le chiaccherate costruttive.

Ringrazio il PNC, per avermi dato un'occasione nonostante arrivassi da un percorso distante. Ringrazio tutti i miei colleghi del corso, è un onore far parte di questo gruppo.
Ringrazio il gruppo di Bicocca, che mi ha permesso di avvicinarmi a questo mondo.

Un grazie sincero va poi a chi c'è sempre stato.

Grazie ai miei amici di una vita, per essere una certezza e un punto fermo.

Grazie Mamma, se sono quello che sono lo devo a te.

Grazie Papà, grazie Riky e grazie Bea, per l'affetto con cui aspettate sempre che ritorni.

Grazie Nonna, per essere sempre stata al mio fianco.

Grazie Benedetta, che anche quando lontana mi sei vicina, che hai sempre una buona parola e mi ricordi quanto valgo.

E grazie a me, dato che alla fine il lavoro sporco l'ho fatto io.